Dynamic Evolution of Explosive Events on the Sun:
Diagnostics Using Hα Observations

Denis Pavel Cabezas Huamán
Department of Astronomy
Kyoto University

A thesis submitted for the degree of
Doctor of Philosophy

Supervised by
Prof. Ayumi Asai, and Prof. Kiyoshi Ichimoto

February 2020

Dynamic Evolution of Explosive Events on the Sun: Diagnostics Using Hα Observations

by Denis Pavel Cabezas Huamán

February 3, 2020

Acknowledgement

First of all, I would like to express my sincere gratitude to my supervisors Prof. Kiyoshi Ichimoto and Prof. Ayumi Asai. Thanks to their guidances, encouragements and discussions the results presented in this thesis could be accomplished. It would have been really difficult to complete this work without their support. I would also like to acknowledge Prof. Kazunari Shibata for many advices, the lectures and discussions in an informal setting during the MHD seminar. Particularly, my background on shock waves has broaden thanks to the seminars.

I am deeply indebted to many people who supported me to come to Japan for pursuing the doctoral course in Kyoto University. Special mention goes to José K. Ishitsuka, Kazunari Shibata, Kiyoshi Ichimoto, Ayumi Asai, Satoru UeNo, Satoshi Morita, Reizaburo Kitai, and also to my family for supporting me during these years and understanding my life abroad.

I wish to thank the staff of the Astronomical Observatory office Ms. Mami Obase, Mrs. Ayako Okamura, and all the members of Hida Observatory, for their kind support and the hospitality during my visit to the observatory.

Finally, I would like to thank my friends and colleagues in the Department of Astronomy, it was a great pleasure to share and spend all these years along with you not only the academic life in Kyoto University.

Abstract

Any explosive event occurring in the solar atmosphere is related to the process of magnetic reconnection and the energy release mechanism. In the last decades, these aspects have extensively been discussed on the basis of numerical investigations and confirmed observationally. Recently, unprecedented high-resolution observations have revealed much more about the role of magnetic reconnection as the principal initiation mechanism of solar eruptions. However, despite important progresses, from theoretical and observational points of view still it is necessary further comprehension of solar eruptions, especially the large-scale events: flares, filament and prominence eruptions, and coronal mass ejections (CME); the later being the major contributor to the space weather. Here it is worth to mention that there is no a definitive consensus about the triggering mechanism of filament eruptions, and the means by which they are connected to CMEs. Another important issue related to filament eruptions is that in most of the studies the line-of-sight component of high-speed events are scarcely investigated due to the limited dynamic range of Doppler measurements. On the other hand, it is not clear how large-scale disturbances in the solar atmosphere can be initiated by solar eruptions.

With the aim of answering some questions stated above, this thesis contains an observational study of the dynamic evolution of explosive events on the Sun, with special emphasis on events observed in the chromosphere. This includes investigations of two filament eruptions, and a large-scale disturbance in the chromosphere and its associated coronal counterpart. In order to estimate the influence of the eruptions on the Earth, it is necessary to correctly derive the velocity both in the line-of-sight direction and in a plane perpendicular to the line-of-sight, i.e., a three-dimensional velocity field. In this thesis we tried to derive physical quantities, such as velocity field, by observing at multiple wavelength points of the Hα line. In this way, we quantitatively investigated the solar eruptive phenomenon.

On 2011 February 16, a filament eruption was recorded in multiple wavelengths around

the Hα line by the Flare Monitoring Telescope (FMT). This data set allowed us to investigate the three-dimensional velocity field of the filament eruption by applying a modified "cloud model". Based on this result and also using the side-view observations of *STEREO_A* satellite, we also investigate the inclination of the filament eruption. Because this event was associated with a coronal wave, the inclination and the eruption time of the filament suggests that the propagation direction of the observed coronal wave could have been driven by the filament eruption. We also found a clear evidence of the interaction between the coronal wave fronts and Hα quiescent filaments located at far distances from the flare site. Details of the analysis and results are presented in Chapter 2.

Solar flares can also generate transient solar phenomena, such as large-scale propagating disturbances in the chromosphere commonly known as Moreton waves. It is currently accepted that Moreton waves result because of the plasma compression in the chromosphere by the globally propagating shock wave in the corona, which emanates from the flare site. However, Moreton waves are not always present even during large or very energetic flares. So, the open question is what the is difference between flares with and without Moreton waves? In Chapter 3 we address this question by analyzing the Moreton wave on 2014 March 29 detected by the FMT. Thanks to the observations in the wing of the Hα line performed by the FMT, we were able to quantify the amplitude of the disturbance in the chromosphere caused by the passage of the Moreton wave. In other words, we estimated the Doppler velocity of the Moreton wave, which means the velocity of the plasma moving at the front of the Moreton wave. Furthermore, based on our Hα results we attempted to infer the velocity amplitude of the incident wave from the corona, and also to derive the Mach number of the incident shock. Based on the extreme-ultraviolet (EUV) data, we also characterized the coronal wave on 2014 March 29 by calculating the compression ratio and the Alfvén and fast-mode Mach numbers of the coronal wave. The combination of the results from Hα and EUV observations, permitted us to discuss the interaction corona-chromosphere during the passage of a large disturbance in the corona and the role of it in the generation process of the Moreton wave.

In Chapter 4 the analysis of a fast-filament eruption occurred on 2017 April 23 is presented. This event was captured by the Solar Dynamics Doppler Imager (SDDI) instrument incorporated on the SMART telescope, which provides high-resolution filtergrams in a wide spectral window around the Hα line center. As in the event presented in Chapter 2, we applied the "cloud model" for deriving the line-of-sight velocity of filament eruption, although, this time our calculation is better constrained because of the sufficient spectral information provided by the SDDI. In addition to the line-of-sight component of the filament eruption, the apparent motion of the erupting material is also calculated, as well as the acceleration and the total velocity of the leading edge of the eruption. Furthermore, the results of the "cloud model" fitting, that is, the optical depth and the Doppler width, are used to estimate the density of the filament, allowing us to discuss the mechanical energy of the filament eruption.

Contents

List of figures

Chapter 1

General Introduction

1.1 Global Properties of the Solar Atmosphere

The solar atmosphere is generally characterized by the increase of the temperature as a function of height, and by the decrease of the density as a function of the radial distance from the surface. The temperature in the photosphere falls from 6000 K to about 4300 K at the top of the photosphere, a place named as temperature minimum region, then it gradually increases through the chromosphere and abruptly through the transition region to a temperature of $1-2$ MK in the corona. This is a temperature of about three orders of magnitude higher than the temperature of the visible surface. In contrast, the density decreases rapidly with height, in which the number density varies from $\approx 10^{17}$ cm^{-3} in the photosphere to $\approx 10^{11}$ cm^{-3} in the chromosphere, and further to $\approx 10^{9}$ cm^{-3} in the corona. Similarly, there is a considerable variation of the magnetic field in the vertical direction, although it starts to drop more gently in the photosphere the faster reduction takes place the outer corona. The characteristics mentioned above do determine the stratified and dynamics solar atmosphere, wherein each region is governed by different physical processes. Figure 1.1 presents a schematic picture of the variation of the temperature and density as a function of height based on the standard VAL (Vernazza-Avrett-Loeset) model, in which the main three layers of the solar atmosphere, i.e., the photosphere, chromosphere, and corona are characterized by particular changes in the temperature and density. It is believed that at chromospheric temperature the plasma is only partially ionized, while from transition region to coronal temperatures the plasma becomes fully ionized.

An important parameter that characterizes the plasma dynamics in the solar atmosphere is the plasma β. This parameter which is defined as the ratio of the plasma to the magnetic

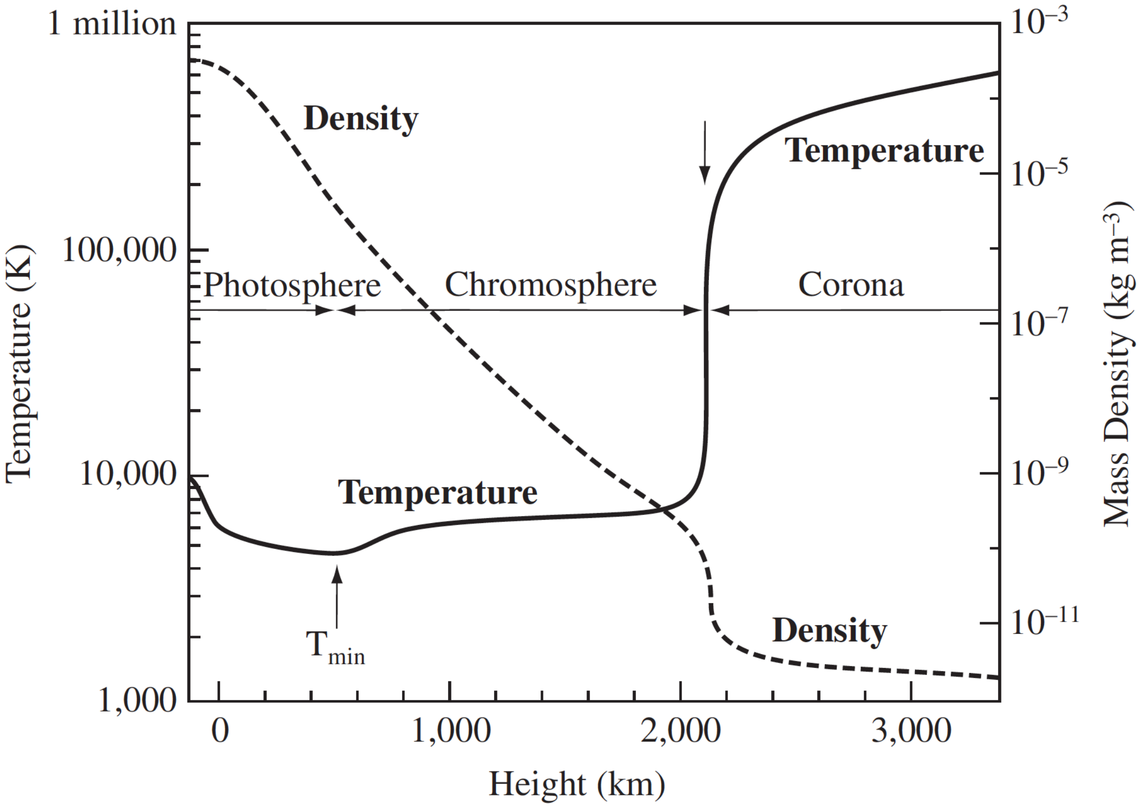

Figure 1.1: An illustration of the mean variation of the temperature and density with height in the solar atmosphere based on the VAL (Vernazza-Avrett-Loeset) model (Adapted from Priest, 2014).

field pressure, indicates whether or not the magnetic field is dominant rather that the gas pressure in a specific region. For example the plasma-β in the solar corona is less than unity, meaning that the magnetic force and magnetic energy govern this layer. Below the chromosphere it is expected $\beta > 1$, we enter into the regime where the gas pressure controls the topology and dynamics of all phenomena occurring in deeper layers of the solar atmosphere.

In describing the solar atmosphere, it is also useful to define the scale height. The scale height is the measure of how the density and the pressure decreases as a function of the vertical distance, which has also a strong dependence on the variation of the temperature. For this, it is assumed an atmosphere in hydrostatic equilibrium over which the pressure and the density falls by a factor of e. For example, the larger scale height in the corona is a consequence of much larger coronal temperature and lighter hydrogen gas (Aschwanden, 2004).

To conclude, any phenomenon happening in the solar atmosphere is dependent on the temperature, density, and the magnetic field. Therefore, it is required further understanding of the basic quantities described above if we want to do a diagnostic of any solar phenomenon.

1.2 Solar Flares

Solar flares are explosive phenomena observed in the solar atmosphere, in which the accumulated magnetic energy is abruptly released in a very short period. The amount of the released energy during a solar flare is about $10^{28} - 10^{32}$ erg, and the typical duration is $10^3 - 10^4$ s which depends on the spatial size of the flare (Shibata & Magara, 2011). The released magnetic energy is then converted into radiative energy, kinetic bulk energy, and thermal and nonthermal energies. The flare is a complex and short-term phenomenon which occurs in active regions where the magnetic topology is rapidly changing due to the sunspots evolution, new flux emergence or some instability. The manifestation of a solar flare can be seen simultaneously in almost all regions of the electromagnetic spectrum, extending from radio, optical, UV spectral lines, soft/hard X-rays, and sometimes even up to gamma rays.

The source of the flare energy is generally believed to be the magnetic field, and the main way of accomplishing its release is by magnetic reconnection (Priest, 2000). However, the build up process of the magnetic energy for the occurrence of flares still remains as an open question. It is thought that the process of the energy accumulation starts slowly over time intervals of hours and days in active regions where the field lines are deep-rooted in the photosphere. The complex motions of sunspots and sub-photospheric structures cause stresses in the field lines, these latter serve as reservoirs of magnetic energy. Here it is instructive to include some details on the magnetic energy accumulated in a sunspot and the amount needed the produce a solar flare. Considering a typical sunspot with size L and the averaged magnetic field B, the total magnetic energy stored in such a sunspot is

$$E_{mag} \simeq (B^2/8\pi)L^3 \simeq 10^{33} \left(\frac{B}{10^3\mathrm{G}}\right)^2 \left(\frac{L}{3 \times 10^9\mathrm{cm}}\right)^3 \mathrm{erg}, \quad (1.1)$$

which is sufficient to produce even the largest flare (Shibata & Magara, 2011). Only a small fraction of this total energy is used for a flare, and the large remaining part is distributed in form of potential field energy.

Most of the flares are visible by their line emission, such as in chromospheric lines (e.g., Hα, CaII, MgII). For example, in Hα filtergrams typically the flare appears as compact bright structures, but during large flares two-ribbons of Hα emission usually form. The sudden enhancement of the Hα emission is interpreted as the chromospheric response to the conversion of the magnetic energy released during a flare into heat and particle acceleration.

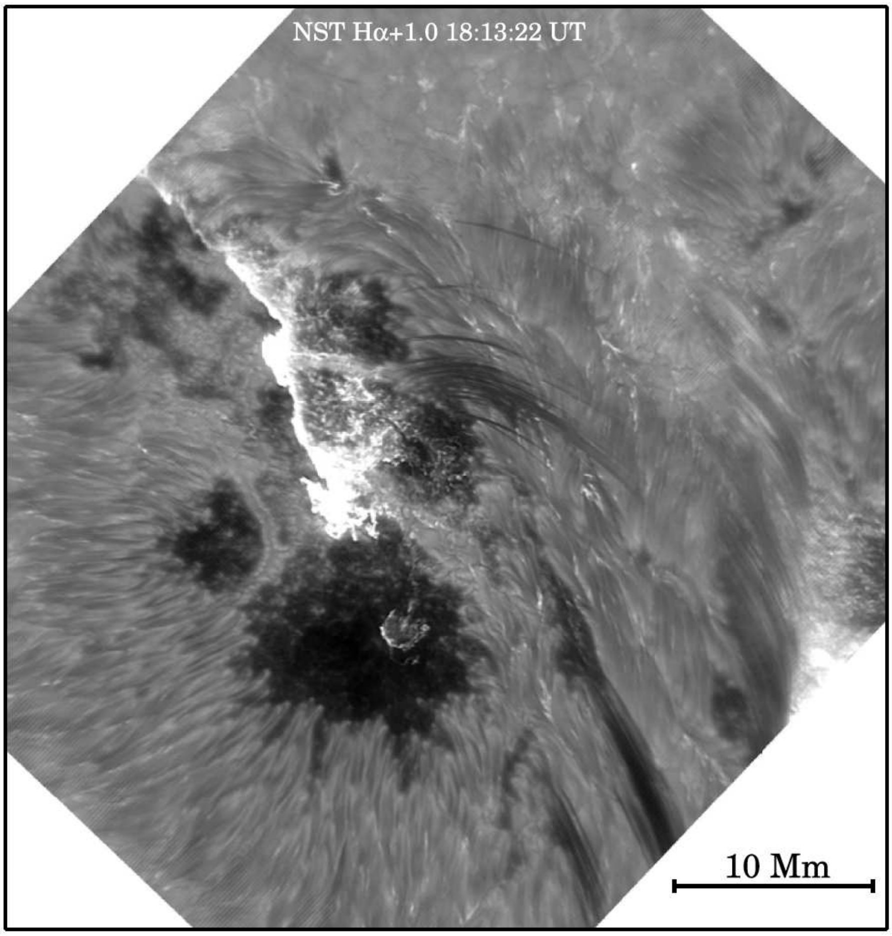

Figure 1.2: A solar flare observed at Hα + 1.0 Å on 2015 June 22 by the 1.6m New Solar Telescope (NST) at Big Bear Solar Observatory. In addition to the flare (brightening), cool falling material are also seen streaming down on the flaring region. It is more likely that the falling plasma is related to the chromospheric condensation (Adapted from Jing et al., 2016).

In Figure 1.2 an example of a solar flare observed in the wing of the Hα line is presented. The figure shows unprecedented details of the flare including a flare ribbon propagating across the sunspots, as well as flows of cool plasma.

Solar flares are often accompanied with other dynamic phenomena, for example, filament and prominence eruptions, and a large-scale eruption known as coronal mass ejection (CME). Large flares can produce disturbances in the solar atmosphere and the response of it may be manifested in different manners. For example, coronal waves that are frequently observed associated with flares and CMEs, suggests that global magnetohydrodynamics shock waves emanate from the flare site. In occasions when the disturbance reaches the chromosphere, it can also lead to the appearance of outwards propagation wave fronts from the flaring region. The latter phenomenon known as Moreton wave is of particular interest in our study and will be addressed in Section 1.3, and the results of a studied event are presented in Chapter 3.

1.3 Shock Waves and Large-Scale Propagating Disturbances in the Solar Atmosphere

As mentioned in the previous section large-scale propagating disturbances in the solar atmosphere or global waves have a close connection with flares and coronal mass ejections. For example, the eruption of a filament or a quiescent prominence may generate a wave that propagates ahead of the eruption, whereas a solar flare is more likely to produce a large-scale shock wave and its passage through the corona is revealed by type II radio burst emission. Because the complex topology of the solar atmosphere, in particular the corona, the physical understanding of global waves and shocks are not straightforward.

Shock waves associated with explosive events are fundamental physical processes in the solar atmosphere, whose properties and effects have widely been discussed in the framework of magnetohydrodynamics (MHD) theory. Basic concepts and description of shock waves and large-scale propagating disturbances including some shock-related phenomena will be given in the following sections.

1.3.1 Moreton Waves

In the Sun's chromosphere a large-scale wavelike propagating disturbance, that was discovered by Moreton (1960) and Moreton & Ramsey (1960) during the observation of a solar flare in the wing of the Hα line, occasionally happens in association with strong flares. This wave phenomenon known as "Moreton wave" usually propagates as semicircular fronts through the chromosphere over a distance of about 5×10^5 km from the flaring region, at the speed of the order of $500 - 1500$ km s^{-1}. Associated with Moreton waves, filaments and prominences standing in the way of propagation direction can abruptly be induced to oscillate, and in some situations to a disruption. Observations in the Hα spectral line reveal that the leading front of the Moreton wave is observed as enhanced absorption in the red-wing and as reduced absorption (brightening) in the blue-wing, followed by a fainter reversed front that is perceived as enhanced absorption in the blue-wing and as reduced absorption in the red-wing (Dodson & Hedeman, 1968). In the core of the Hα line the wave fronts usually appear as brightening. These observational characteristics were interpreted as depression and a subsequent relaxation process of the chromospheric material, as a consequence of the plasma that is forced to move downward with a velocity of $6 - 10$ km s^{-1} (Švestka, 1976). This was inferred from the motions of spicules and fibrils caused by the wave front passage.

The kinematical properties of the Moreton wave, such as the high speed, the great traveling distances, and the low wave amplitude, led to the question whether this phenomenon is of chromospheric origin because the mentioned physical parameters are incompatible with the framework of wave propagation in the chromosphere. For example, for a typical value of the temperature in the chromosphere of 10^4 K, the sound speed results in $\sim$10 km s^{-1}, and assuming a density 10^{11} cm^{-3} and 15 G of the magnetic field, the Alfvén speed in the chromosphere is about 100 km s^{-1}. A wave traveling in the chromosphere with a speed of 1000 km s^{-1}, as determined from observations, would imply that this wave moves with a Mach number of about 10. A shock wave of such strength should exhibit a strong amplitude and would fully be dissipated before traveling long distances, but these effects are not observed. A comprehensive interpretation of the generation and propagation aspects of the Moreton wave is conducted if wave propagation in the corona is considered, where the sound and Alfvén speeds are about one order of magnitude larger than in the chromosphere. This idea was initially postulated by Anderson (1966) and Meyer (1968), and was further modeled by Uchida (1968). According to Uchida's model, the pressure pulse during the explosive phase of a solar flare generates an MHD fast-mode wave in the corona, which compresses and pushes the chromospheric plasma downward, and as a result, the Moreton wave is created. A good correlation between type II radio burst and Moreton waves does exit (Kai, 1970). The former traces the upward-propagating fast-mode shock in the corona, therefore this supports the scenario described by Uchida.

In an effort to better understand the nature of the Moreton waves, a few studies have been conducted using Hα wing observations (e.g., Warmuth et al., 2004; Veronig et al., 2006; Balasubramaniam et al., 2007; Narukage et al., 2008; Muhr et al., 2010; Balasubramaniam et al., 2010), also in Hβ (Zhang, 2001), and in the Helium I line at 10830 Å (Vršnak et al., 2002b; Gilbert & Thomas, 2004). Most of the studies have focused on the kinematics of the horizontal and lateral propagation speed, and some of them on the morphology and Doppler velocity of the wave fronts, although no firm conclusions were drawn about the latter. For example, Balasubramaniam et al. (2007) reported a Doppler velocity of about 2.6 km s^{-1} in the chromosphere based on Dopplergrams of a Moreton wave. Certainly, the signature of Moreton waves is very faint, and in general the perturbation or the associated line-shift of the Hα spectral profile cannot easily be distinguished. Figure 1.3 shows an example of a

Moreton wave observed in the Hα line on 2006 December 6.

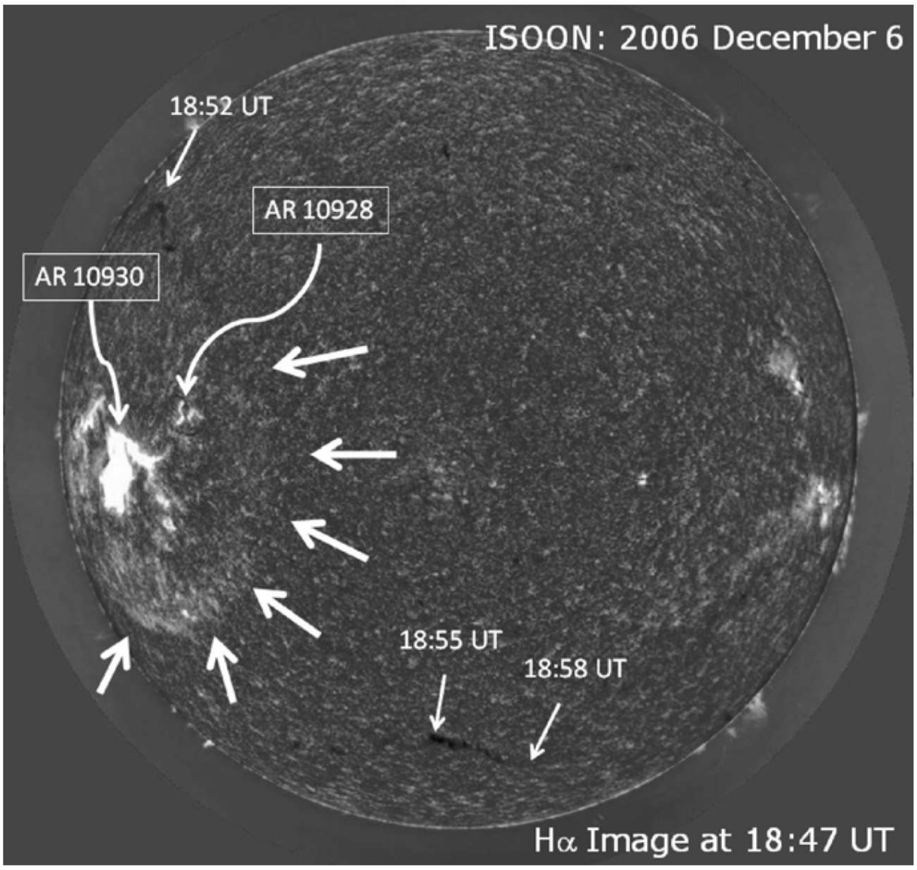

Figure 1.3: Moreton wave on 2006 detected by the ISOON telescope in the Hα line center. The brightest region is the associated X6.5 flare, and the wave front is indicated by the large arrows. (Adapted from Balasubramaniam et al., 2010).

1.3.2 Coronal Waves

In 1997, a large-scale wave propagating disturbance was discovered in the coronal emission line Fe XII (195 Å) in association with a C-class flare (Thompson et al., 1999). This coronal wave, called "Extreme-ultraviolet Imaging Telescope (EIT) wave" after the EIT (Delaboudinière et al., 1995) on board the *Solar and Heliospheric Observatory* (*SOHO*; Domingo et al., 1995), was expected to be the fast-mode MHD counterpart of the Moreton wave, as predicted by Uchida (1968). However, over the past 20 yr the debate for interpreting this phenomenon as an MHD fast-mode wave was intense (see reviews by Chen, 2016; Long et al., 2017). The controversy resides in its physical nature, such as the long-lasting coronal dimming, stationary brightening, and particularly its traveling speed because it ranges between 170 − 350 km s^{-1} (Klassen et al., 2000; Thompson & Myers, 2009), which is slower than the expected fast-mode speed, and is sometimes slower than the sound speed in the corona (Thompson &

Myers, 2009). In addition, the EIT waves lack a correlation with type II radio bursts, whose speed is in the range of $300 - 1200$ km s^{-1} (Klassen et al., 2000). In order to overcome the discrepancies on the nature of the EIT and Moreton waves, several models and possibilities were put forward. For example, based on MHD simulations by Chen et al. (2002) and extending them, Chen, Fang, & Shibata (2005) found that an upward-expanding flux-rope is capable of triggering a coronal mass ejection (CME) by which two wavelike propagating disturbances are produced: a fast-mode shock wave, and a slower component related to the density perturbation resulting from successive stretching field lines that overlies the erupting flux-rope. Here it is worth noticing that Delannée & Aulanier (1999) identified a bright front in EIT images associated with a flare and CME, and they proposed a scenario of magnetic field reconfiguration as a model of EIT waves. Alternative interpretations have also been suggested in order to clarify the inconsistency of the velocity between the EIT and Moreton waves, such as a subsequent deceleration (Warmuth et al., 2001), which was explained in terms of fast-mode shock produced by a "blast wave" rather than a flux-rope expansion. Note that in the meantime, large-scale disturbances associated with flares traveling through the corona were also detected in soft X-ray emission (e.g., Khan & Aurass, 2002; Narukage et al., 2002; Hudson et al., 2003; Warmuth et al., 2005; Asai et al., 2008), and reported in radio wavelengths as type II burst (e.g., Khan & Aurass, 2002; Eto et al., 2002; Vršnak et al., 2005). They were interpreted as the coronal counterpart of Moreton waves.

For nearly a decade, the Atmospheric Imaging Assembly (AIA; Lemen et al., 2012) on board the *Solar Dynamics Observatory* (*SDO*; Pesnell et al., 2012) has been constraining our understanding of coronal waves. From now on, we will use the term "extreme-ultraviolet (EUV) waves" to refer to large-scale coronal disturbances that are observed in the EUV passbands. Thanks to the unprecedented capability of AIA, significant discoveries were possible, including intrinsic characteristics that have never seen before of the coronal EUV waves. So, it is more likely that the controversy on the EIT waves is coming to an end. It is currently more accepted that two types of large-scale wavelike phenomena appear in the corona in association with flares and CMEs. The first is the MHD fast-mode or shock traveling ahead, and the other is the second or slow component straddling behind. This picture was initially reported by Harra & Sterling (2003) based on observations obtained with the *Transition Region and Coronal Explorer* (*TRACE*; Handy et al., 1999), suggested by analytical and numerical approaches (e.g., Chen et al., 2002), and has been confirmed by numerous recent studies (see

Liu & Ofman, 2014; Warmuth, 2015). Clear evidence of co-spatiality between the fast-mode EUV wave and the Moreton wave was also found (Asai et al., 2012), and the association with type II radio burst displays a high tendency (Nitta et al., 2013). It should be mentioned that statistical investigations have shown that EUV waves are more linked to CMEs rather than solar flares (Biesecker et al., 2002; Nitta et al., 2013, 2014; Muhr et al., 2014), although the mechanism by which they are related still remains puzzling.

In Figure 1.4 an example of a coronal wave recorded by AIA in the EUV band is displayed. The propagation of a dome-like structure similar to a shock is observed, also large-scale disturbances on the solar surface related to the wave passage. This event was analyzed in detail and the results are presented in Chapter 3.

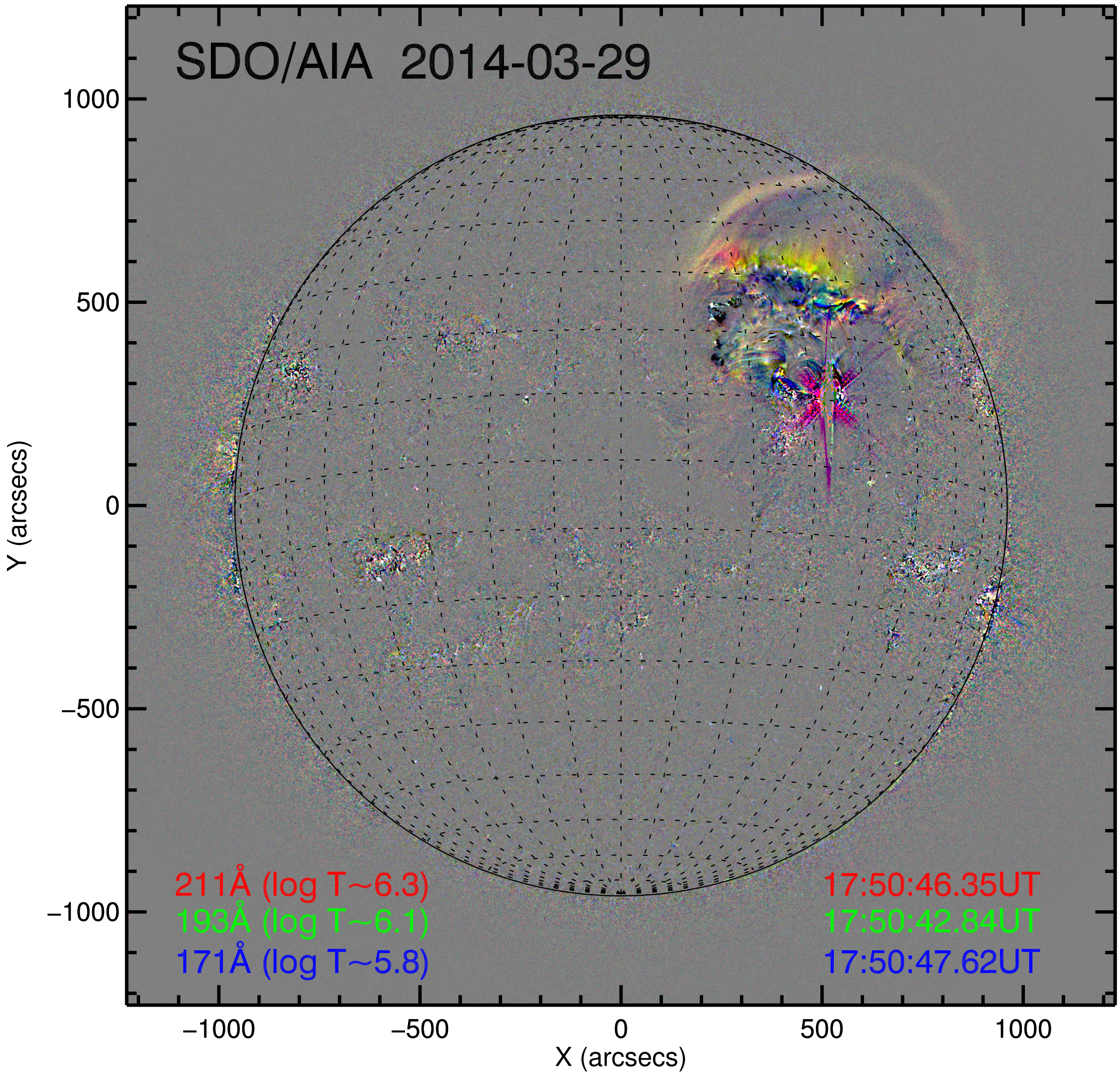

Figure 1.4: Coronal wave on 2014 March 29 captured by SDO/AIA in the EUV passbands. The map shows a combination of cool (171 Å), warm (193 Å), and hot (211 Å) temperature channels of AIA, at which the different components of the coronal wave are highlighted in blue, green, and red colors.

1.4 Hydrodynamic Shocks

Any disturbance or motion on the solar surface and above can lead to the formation of shocks. Shocks occur at discontinuous boundaries, a place where the wave steepens and attains a finite amplitude, so the nonlinear terms in the wave equation become important since they make the crest of the wave to move faster than its leading or trailing edge. If the shock speed far exceeds the sound speed we will expect a strong shock, but when the shock speed is slightly larger than or comparable to the sound speed it is called weak shock (Landau & Lifshitz, 1987; Priest, 2000). When the shock hits, there is a sudden jump in the velocity v, density ρ, pressure p, and in the temperature of the gas, that is to say, the quantities concerned change discontinuously across the so called surface of discontinuity. Moreover, the dissipation inside the shock front leads to the gradual conversion of the excess of the wave energy into heat. The conditions behind the shock front (denoted by the subscript 2) are related to those ahead (denote by the subscript 1) by the equations of conservation of mass, momentum and energy, respectively as:

$$\rho_2 v_2 = \rho_1 v_1, \tag{1.2}$$

$$p_2 + \rho_2 v_2^2 = p_1 + \rho_1 v_1^2, \tag{1.3}$$

$$p_2 v_2 + (\rho_2 e_2 + \frac{1}{2}\rho_2 v_2^2) v_2 = p_1 v_1 + (\rho_1 e_1 + \frac{1}{2}\rho_1 v_1^2) v_1, \tag{1.4}$$

where for a perfect gas the internal energy per unit mass is $e = p/[(\gamma - 1)\rho]$. These set of equations are referred as to the Rankine-Hugoniot relations or jump conditions.

Equation (1.2) tells us that the mass flux ρv crosses a unit area in unit time. The term $(\rho v)v$ in Equation (1.3) gives the rate at which the momentum is transported across a unit area, and the work done by the pressure force on the same unit area is p. In Equation (1.4) $(\rho e + \frac{1}{2}\rho v)$ represents the rate of transport of internal and kinetic energy, while pv is the rate at which the gas pressure does work (Priest, 2000). Equations (1.2)–(1.4) can be expressed as jumps of various shock parameters, such as

$$\frac{\rho_2}{\rho_1} = \frac{(\gamma+1)M_1^2}{2+(\gamma-1)M_1^2}, \tag{1.5}$$

$$\frac{v_2}{v_1} = \frac{2+(\gamma-1)M_1^2}{(\gamma+1)M_1^2}, \tag{1.6}$$

$$\frac{p_2}{p_1} = \frac{2\gamma M_1^2-(\gamma-1)}{\gamma+1}. \tag{1.7}$$

Here $M_1 = v_1/c_{s1}$ is the shock Mach number defined as the ratio of the velocity of the shock to the sound speed c_s, and γ is the adiabatic index of the gas.

In the MHD regime, the magnetic field influences considerably the shock structure. The simplest type of magnetic shock is the perpendicular case, wherein the velocity of the shock and plasma are perpendicular to the magnetic field. On the other hand, there is a particular case of shock propagation, which is called oblique shock. Unlike the perpendicular situation, in the oblique case the parallel and normal components of the magnetic field acting on the shock front must be taken into account. In similar manner as before, the properties of these two special cases can be derived from the equations of conservation of mass, momentum, energy, and magnetic flux, namely, the shocked plasma (v_2, ρ_2, p_2, B_2) are related to the unshocked plasma (v_1, ρ_1, p_1, B_1). In Section 3.5 of Chapter 3, we applied the theory of the oblique shock to analyze the properties of the coronal wave on 2014 March 29.

1.5 The Riemann Problem: Application to a Shock Tube

The state of a moving gas whose thermodynamics properties are known can be described in terms of its velocity, density, and pressure as a function of position and time. Such properties are well defined by the Euler equations, in which the conservation laws of conservation of mass, momentum and energy are taken into consideration to investigate the physical characteristics of propagating flows. In 1860, Riemann first analyzed the problem of how flows develop when two adjacent slabs of fluid with different physical properties interact violently each other, as a result Riemann observed discontinuities. This problem commonly referred to as the "Riemann problem", is widely used as a standard numerical scheme for studying the gas dynamics and shocks. A special case of the Riemann problem is the "shock tube" problem, because its solution is characterized by the appearance of shocks, reflected, and rarefaction waves, therefore, it can be used as a test for numerical methods when dealing with discontinuous problems. The intention in giving a brief description of the Riemann problem is to make easier the understanding of our results presented in Chapter 3 (Section 3.5) about a coronal shock wave and its interaction with the chromosphere.

1.5.1 Physical Description of the Shock Tube Problem

The fundamental idea of the shock tube is the following. Consider a long tube (1D), closed at its ends and separated into two regions by a very thin layer or a diaphragm. Each region of the tube is filled with the same gas but with different thermodynamics parameters (e.g., pressure p, density ρ, and temperature T). In the scheme, the region of the tube with highest pressure contains the *driver gas*, while the low pressure part consists of the *test gas*. Usually the low pressure part of the tube is several times longer that the highest pressure region. Initially the gas is at rest, and at a given time the breakdown of the diaphragm causes that the highly compressed gas flows into the low pressure gas. As a results, a shock wave is generated compressing the gas and propagating through the *test gas*, while a rarefaction wave expands through the *driver gas*. The expanded gas is separated from the compressed gas by the contact discontinuity, which travels at constant speed behind the shock wave.

The process described above is better illustrated by means of an x–t diagram (Figure 1.5), where it is identified the shock wave, contact discontinuity, and the region where the rarefaction wave propagates. We note that in the diagram the shock and the contact discontinuity propagates to the right (R), having a constant velocity because they move in uniform regions. The expansion of the rarefaction wave is in left direction (L) through a new region (E) limited by OC and OD lines in our diagram.

The solution of the shock tube problem is obtained by considering the physical variables behind the shock wave and applying the jump relations across the discontinuities (see Section 1.4). It is also important to remember the following characteristics of wave propagation: the shock wave implies the discontinuity of all the parameters of the flow which are described by the Rankine-Hugoniot relations (see Equations 1.5–1.7 in Section 1.4), and the contact discontinuity is in fact a discontinuity of the density function, the pressure and the velocity being continuous. Under this consideration it is found the exact solution to the shock tube problem (e.g., Landau & Lifshitz, 1987; Zel'dovich & Raizer, 2002; Danaila et. al, 2007). We show an illustration of the solution of the Sod shock tube problem[1] in Figure 1.6.

[1]The Sod solver is a module built to calculate analytics solution for a shock tube problem. In our illustration we used the repository implemented by J. Škifić under the MIT license 2015.

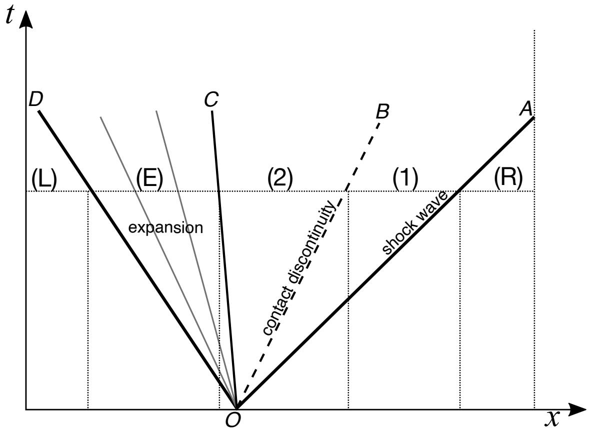

Figure 1.5: x–t diagram of the shock tube problem. The solution is presented in Figure 1.6.

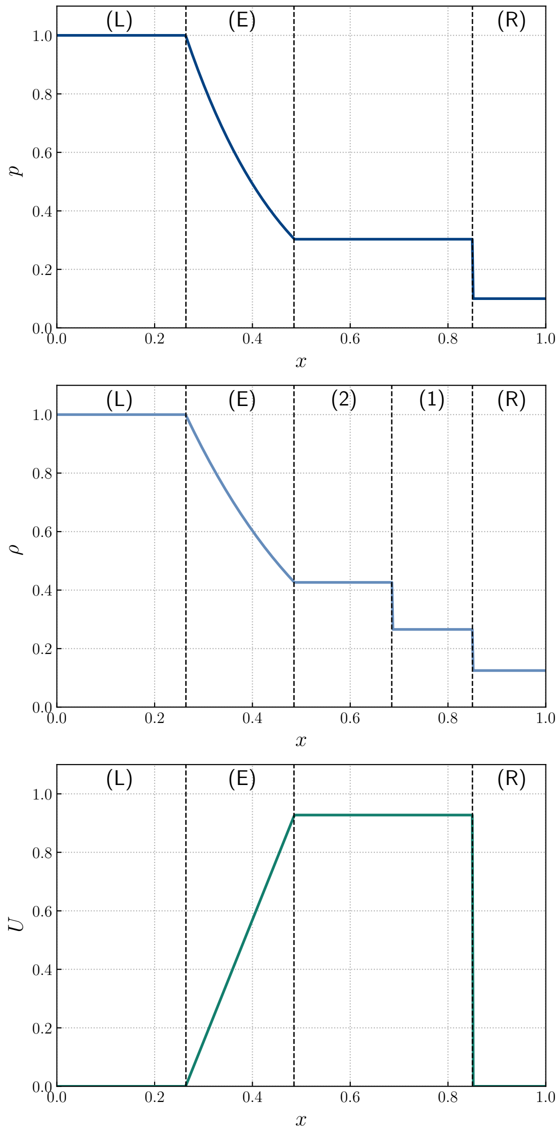

Figure 1.6: Analytical solution of the shock tube problem based on the Sod shock tube calculator. The plots show the pressure p, density ρ, and velocity U distributions, respectively. In the scheme the shock is located at $x = 0.85$ which is visible in the origin of region (R), while the contact discontinuity appears at $x = 0.68$ in the density profile in the limit of regions (2) and (1). On the other hand, the rarefaction is manifested in the region (E), expanding from $x = 0.48$ to $x = 0.26$.

1.6 Filament Eruptions and their Relation with Coronal Mass Ejections

Solar filaments which are seen as dark elongated structures against the bright solar disk, or prominences when are projected above the solar limb as brighten features, are dense and cool "clouds" immersed in the hot corona. They are best observed in the hydrogen and helium spectral lines that originate at chromospheric temperatures, thus confirming that the filaments are made up of low temperature plasma ($T \lesssim 10^4$ K). This is a temperature of about two orders of magnitude lower than the surrounding corona, a region where the magnetic field is dominant than the gas pressure ($\beta < 1$). Because the filaments are confined only in some specific regions of the solar corona and located over and along the polarity inversion lines of the photosphere, it is believed that they are sustained in equilibrium mainly by the horizontal component of the ambient magnetic field where the field lines have dipped shapes. In the last decades important progresses and investigations have been made about the filaments or prominences (for recent reviews see Vial & Engvold, 2015), however, some aspects requires further comprehensions. For example, the origin and formation of filaments, the energy and the force that prevents the material from collapsing, and the mechanism of their sudden eruptions.

As observations have revealed, various forms of eruptive phenomena occur in the solar atmosphere which develop at different time and spatial scales. Despite their differences in appearance, it is quite well established that these phenomena are manifestations of the same physical processes involving magnetic reconnection and plasma ejection (Priest & Forbes, 2002; Shibata & Magara, 2011). For example, there are certain events that can be described in terms of disruption of unstable magnetic structures, such as flare-sprays, eruptive filaments/prominences, coronal mass ejections (e.g., Kurokawa et al., 1987; Vršnak, et al., 1991; Antiochos et al., 1999; Forbes, 2000). On the other hand, in events such as surges, spicules, X-ray and chromospheric jets, the ejection is controlled more or less by the field lines, that is, the plasma is expelled along the magnetic field lines (Shibata , 1999; Shibata et al., 2007).

The question on how a filament in quasi-equilibrium becomes unstable and, what is the driving mechanism responsible for its eruption and acceleration still are subjects of intense investigations. The mechanism leading to the loss of equilibrium and then to the eruption may involve an ideal-MHD instability and/or non-ideal processes, such as magnetic reconnection.

Ideal processes such as helical kink and torus instabilities (Sakurai, 1976; Priest et al., 1989; Titov & Démoulin, 1999; Kliem & Torok, 2006, and references therein) are invoked as the possible initiation mechanism for the eruption. It is suggested that the kink instability enters in action when the filament experiences an excessively twist above a critical value, whereas the torus instability occurs when the filament approaches to a critical height. Alternatively, fast magnetic reconnection can also initiate an eruption without the presence of twisted pre-eruptive filaments (e.g., Karpen et al., 2012). On the other hand, the emerging flux trigger model (Chen & Shibata, 2000) was also proposed, in which a newly emerging magnetic field interacts with the preexisting field that contains the filament. The mechanisms described above can explain well the initiation of the flux-rope or filament eruption, however, from observational point of view, it is very difficult to directly measure and to detect, for example, the twist of the filament as well as the magnetic reconnection.

Filament eruptions or disappearance have been studied for a long time, although our knowledge of their close association with coronal mass ejections (CMEs) date back only to a few decades (see Webb, 2015; Gopalswamy, 2015). As is shown in Figure 1.7, nowadays it is well established that filament/prominence eruptions play an essential role in the generation process of CMEs, the latter being a major contributor to space weather at the Earth. Therefore, the monitoring and investigations of the formation, activation, and eruption of filaments are fundamental issues to advance into our understanding of CMEs.

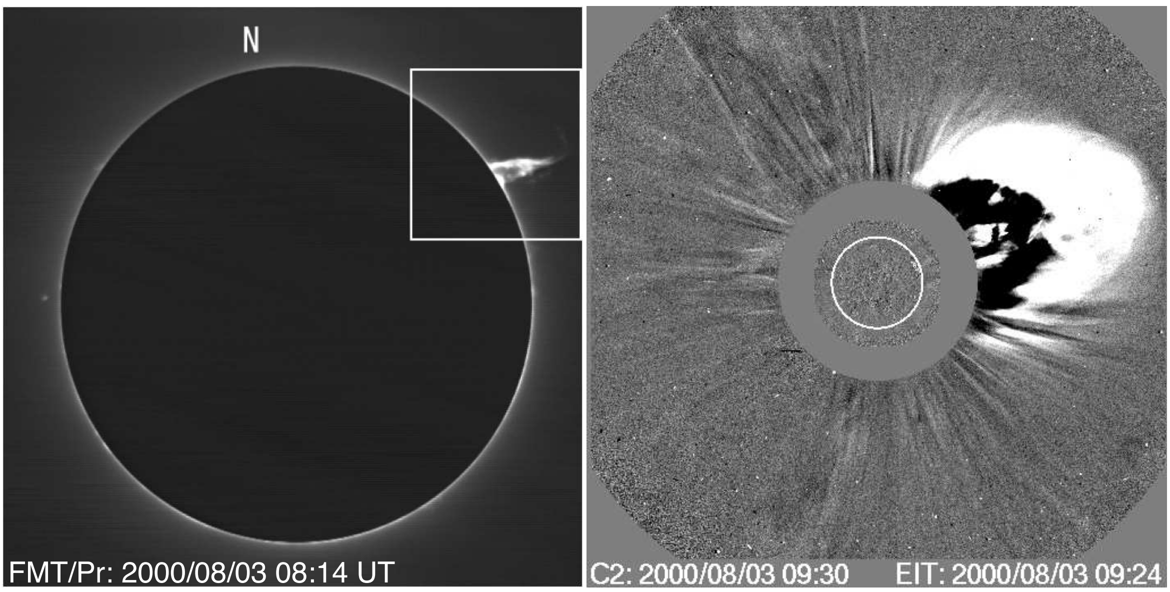

Figure 1.7: Prominence eruption on 2000 August 03 (left panel) captured by the Flare Monitoring Telescope at Hida Observatory. This eruption occurred at the west limb and produced a fast coronal mass ejection (right panel) with a speed of about 896 km s^{-1}, as recorded by the SOHO/LASCO satellite.

When a filament enters into the eruptive state, it first interact with the coronal magnetic field creating changes of the original magnetic field configuration. Hence, the key is to figure out the interaction of the filament with the neighboring magnetic structures and understand the interplay of the governing forces, such as the Lorentz force and the gravitational force. Asai et al. (2009) studied the characteristics of an active region and the formation and disappearance of a filament, the authors clearly showed that the interaction of the filament with the surrounding ambient magnetic field played a role in the generation of CMEs and the interplanetary consequences. Theoretical aspects on the eruption, propagation and the interplanetary consequences was studied in detail by Chen (1996).

Finally, there are considerable works related to the dynamics of filament and prominence eruptions in association with CMEs (see the review of Webb & Howard, 2012), and also recent statistical investigations (e.g., Shimojo, 2014; McCauley et al., 2015, and references therein). However, all of the studies, with a few exceptions (e.g., Penn, 2000; Morimoto & Kurokawa, 2003; Filippov, 2013), use as the main parameter the projected motion of the eruption in the plane-of-sky, and assumptions are taken in order to derive the real motion (line-of-sight) of the erupting materials. Because one of main objective of this thesis is to study the dynamic of filament eruptions, in Chapters 2 and 4 we present a detailed analysis of two events detected in Hα by the Flare Monitoring Telescope (FMT) and by the Solar Magnetic Research Activity Telescope (SMART), respectively. By combining Hα wing observations and applying the "cloud model", the three-dimensional velocity field of the erupting filaments are derived.

References

Anderson, G.F. 1966, University of Colorado, Boulder (Thesis)

Antiochos, S.K., DeVore, C. R., & Klimchuk, J. A. 1999, ApJ, 510, 485

Asai, A., Hara, H., Watanabe, T., et al. 2008, ApJ, 685, 622

Asai, A., Shibata, K., Ishii, T.T., et al. 2009, J. Geophys. Res., 114, A00A21

Asai, A., Ishii, T. T., Isobe, H., et al. 2012, ApJL, 745, L18

Aschwanden, M. 2004, Physics of the Solar Corona (Praxis Publishing)

Balasubramaniam, K.S., Pevtsov, A.A., Neidig, D.F. 2007, ApJ, 658, 1379

Balasubramaniam, K.S., Cliver, E.W., Pevtsov, A., et al. 2010, ApJ, 723, 587

Biesecker, D.A., Myers, D.C., Thompson, B.J., Hammer, D.M. & Vourlidas, A. 2002, ApJ, 569, 1009

Chen, J. 1996, J. Geophys. Res., Vol. 101, 27, 499

Chen, P.F., Shibata, K. 2000, ApJ, 545, 524

Chen, P.F., Wu, S. T., Shibata, K., Fang, C. 2002, ApJ, 572, L99

Chen, P.F., Fang, C., Shibata, K. 2005, ApJ, 622, 1202

Chen, P.F. 2016, Low-Frequency Waves in Space Plasmas, Monograph Series, 216, 381

Danaila, I., Joly, P., Kaber, S. M., Postel, M. 2007, An Introduction to Scientific Computing (Springer)

Delaboudinière, J.-P., Artzner, G. E., et al. 1995, SoPh, 162, 291

Delannée, C., Aulanier, G. 1999, SoPh, 190, 107

Domingo, V., Fleck, B., Poland, A. I. 1995, SoPh, 162, 1

Dodson, H.W., Hedeman, E.R. 1968, SoPh, 4, 229

Eto, S., Isobe, H., Narukage, N., et al. 2002, PASJ, 54, 481

Filippov, B. P. 2013, ApJ, 773, 10

Forbes, T.G. 2000, J. Geophys. Res., Vol. 105, 153, 165

Gilbert, H.R., Thomas, E.H. 2004, ApJ, 610, 572

Gopalswamy, N. 2015, Astrophysics and Space Science Library, Vol. 415, Solar Prominences

Handy, B.N., Acton, L.W., Kankelborg, C.C., et al. 1999, SoPh, 187, 229

Harra, L.K., Sterling, A.C. 2003, ApJ, 587, 429

Hudson, H., Khan, J.I., Lemen, J.R., Nitta, N.V., Uchida, Y. 2003, SoPh, 212, 121

Jing, J., Xu, Y., Cao, W., et al. 2016, Sci. Rep. 6, 24319

Kai, K. 1970, SoPh, 11, 310

Karpen J.T., Antiochos, S.K., & DeVore, C.R. 2012, ApJ, 760, 81

Khan, J.I., Aurass, H., 2002, A&A, 1018, 1031

Klassen A., Aurass, H., Mann, G., Thompson, B.J. 2000, A&AS, 141, 357

Kliem, B., & Torok, T. 2006, Phys. Rev. Lett., 96, 255002

Kurokawa, H., Hanaoka, Y., Shibata, K., Uchida, Y. 1987, SoPh, 108, 251

Landau, L.D., Lifshitz, E.M. 1987, Fluid Mechanics 2nd ed., (Pergamon Press)

Lemen, J. R., Title, A., Akin, D. J., et al. 2012, SoPh, 275, 17

Liu, W., Ofman. 2014, SoPh, 289, 3233

Long, D.M., Bloomfield, D.S., Chen, P.F., et al. 2016, SoPh, 297, 7

McCauley, P. I., Su, Y. N., Schanche, N., et al. 2015, SoPh, 290, 1703

Meyer, F. 1968, Structure and Development of Solar Active Regions, IUA Symp., 35, 485, (K.O. Kiepenhever)

Moreton, G. E. 1960, AJ, 65, 494

Moreton, G. E., Ramsey, H. E. 1960, PASP, 72, 357

Morimoto, T., & Kurokawa, H. 2003, PASJ, 55, 1141

Muhr, N., Vršnak, B., Temmer, M., Veronig, A.M., Magdalenić, J. 2010, ApJ, 708, 1639

Muhr, N., Veronig, A.M., Kienreich, I.W., Vršnak, B., Temmer, M., Bein, B.M. 2014, SoPh, 289, 4563

Narukage, N., Hudson, H.S., Morimoto, T., et al. 2002, ApJ, 572, L109

Narukage, N., Moritmoto T., Kadota, M., et al. 2004, PASJ, 56, L5

Narukage, N., Ishii, T.T., Nagata, S., UeNo., S., et al. 2008, ApJ, 684, L45

Nitta, N.V., Schrijver, C.J., Title, A.M., Liu, W. 2013, ApJ, 776, 58

Nitta, N.V., Aschwanden, M.J., Freeland, S.L. 2014, SoPh, 289, 1257

Penn, M. J. 2000, SoPh, 197, 313

Pesnell, W. D., Thompson, B. J., Chamberlin, P. C. 2012, SoPh, 275, 3

Priest, E., Hood, A. W., Anzer, U. 1989, ApJ, 344, 101

Priest, E. R. 2000, Solar Magnetohydrodynamics (Dordrecht: Reidel)

Priest, E. R., Forbes, T. G. 2002, A&AR, 10, 313

Priest, E. R. 2014, Solar Magnetohydrodynamics (Cambridge Univ. Press)

Sakurai, T. 1976, PASJ, 21, 177

Shibata, K., Magara, T. 2011, Living Rev. of Solar Phys., 8, 6

Shibata, K. 1999, Astrophysics and Space Science, 264, 129

Shibata, K., et al. 2007, Science, 318, 1591

Švestka, Z. 1976, Solar Flares (Dordrecht: Reidel)

Shimojo, M. 2014, Nature of Prominences and their Role in Space Weather, 300, 161

Thompson, B. J., Gurman, J. B., Neupert, W. M., et al. 1999, ApJ, 517, L151

Thompson, B. J., Myers, D.C. 2009, ApJS, 183, 225

Titov, V.S., Démoulin, P. 1999, A&A

Uchida, Y. 1968, SoPh, 4, 30

Veronig, A.M., Temmer, M., Vršnak, B., Thalmann, J. 2006, ApJ, 647, 1466

Vial, J.C. & Engvold, O. eds., 2015, Astrophysics and Space Science Library, Vol. 415, Solar Prominences

Vršnak, B., Ruždjak, V., & Rompolt, B. 1991, SoPh, 136, 151

Vršnak, B., Warmuth, A., Brajša, R., Hanslmeier, A., 2002b, A&A, 394, 299

Vršnak, B., Magdalenić, J., Temmer, T., et al., 2005, ApJ, 625, L67

Warmuth, A., Vršnak, B., Aurass, H., Hanslmeier, A. 2001, ApJL, 560, L105

Warmuth, A., Vršnak, B., Magdalenić, J., Hanslmeier, A., Otruba, W. 2004, A&A, 418, 1117

Warmuth A., Mann, G., and Aurass, H. 2005, ApJL, 626, L121

Warmuth, A. 2015, LRSP, 12, 3

Webb, D. F. 2015, Astrophysics and Space Science Library, Vol. 415, Solar Prominences

Webb, D. F, Howard, T. A. 2012, Living Rev. of Solar Phys., 9, 3

Zhang, H. 2001, A&A, 372, 676

Zel'dovich, Ya. B., Raizer, Yu. P. 2002, Physics of Shock Waves and High Temperature Hydrodynamic Phenomena (Dover Publishing, INC.)

Chapter 2

"Dandelion" Filament Eruption and Coronal Waves Associated with a Solar Flare on 2011 February 16

2.1 Motivation

Coronal disturbances associated with solar flares, such as Hα Moreton waves, X-ray waves, and extreme ultraviolet (EUV) waves are fundamental issues related to magnetohydrodynamics fast-mode waves or shocks in the solar atmosphere. In addition, filament eruptions in conjunction with flares are sometimes identified as drivers of coronal waves and CMEs. It is therefore of great importance understand the physical mechanisms of these phenomena to elucidate the connection between them.

We conducted a multiwavelength study of a solar flare and a filament eruption, as well as of the associated coronal wave. The filament eruption was captured in the Hα line by the Flare Monitoring Telescope (FMT) at Ica University, Peru. By using the FMT observations in the wing of the Hα line, we derive the three-dimensional velocity field of the filament eruption, and also the inclination of the erupting material with respect to the solar surface. The evolution of the associated flare is characterized by combining observations in soft X-ray, EUV, and Hα, whereas the dynamic of the coronal wave is investigated using EUV data. Based on Hα and EUV observations we found a clear evidence of interaction of the coronal wave fronts with quiescent filaments located at far distances from the flare site. Our analysis also shows a direct link between the filament eruption and the coronal wave, it suggests that possibly the filament eruption played a role in the propagation direction of the coronal wave.

2.2 Observations and Data

The studied flare occurred in the Active Region NOAA 11158 (S21°, W30°). It started at 14:19 UT and peaked at 14:25 UT on 2011 February 16, and was classified as M1.6 on the *GOES* scale (Figure 2.1). NOAA 11158 produced the first X-class flare in the solar cycle 24 during the previous day. Figure 2.1 shows the time evolution of the *GOES* X-ray emission for the February 16 flare.

For the analysis we use Hα data taken by FMT that provides full-disk solar images in the Hα line center (6562.8 Å), Hα −0.8 Å (blue-wing), Hα +0.8 Å (red-wing), continuum, and limb prominence images (Hα line center with occulting disk). The spatial sampling is about $\sim 2''.0$ pixel^{-1}, and the time cadence is 20 seconds. Such multiwavelength full-disk observations with high time cadence are suitable for investigating the velocity field of erupting filaments (Morimoto & Kurokawa, 2003a,b; Morimoto et al., 2010) and for detecting Moreton waves (Eto et al., 2002). FMT was relocated in March 2010 from Hida Observatory, Kyoto University to the National University San Luis Gonzaga of Ica in Peru by the international collaboration of the Continuous H-Alpha Imaging Network (CHAIN) project (UeNo et al., 2007) for coordinated solar observations.

We did not find any direct signatures of Hα Moreton waves associated with the flare either in the FMT images (in Hα line center and the ±0.8 Å wings) or in their running-difference images. However, we found indirect evidence of the coronal wave in the form of winking filaments that are located far from the flare site. Figure 2.2 shows a full-disk Hα line center image of the flare taken by FMT. We show the flaring region with f_0 and the filaments are denoted f_1 to f_5. The boxes indicate the areas over which we calculate the intensities to identify their winking features activated by the flare and the coronal waves.

Associated with the flare, we also observe a filament eruption whose shape in Hα images looks like a “dandelion”. This feature is especially prominent in the red- and blue-wing images. Figure 2.3 also presents FMT images of the flare, filament eruption, and winking filaments in Hα −0.8 Å (left), Hα line center (middle), and Hα +0.8 Å (right) passbands.

The flare was observed in EUV passbands by the Atmospheric Imaging Assembly (AIA; Lemen et al., 2012) on board the *Solar Dynamics Observatory* (*SDO*; Pesnell et al., 2012) and by the Extreme-Ultraviolet Imager (EUVI) from the Sun-Earth Connection Corona and Heliospheric Investigation (SECCHI; Howard et al., 2008) on board the *Solar Terrestrial*

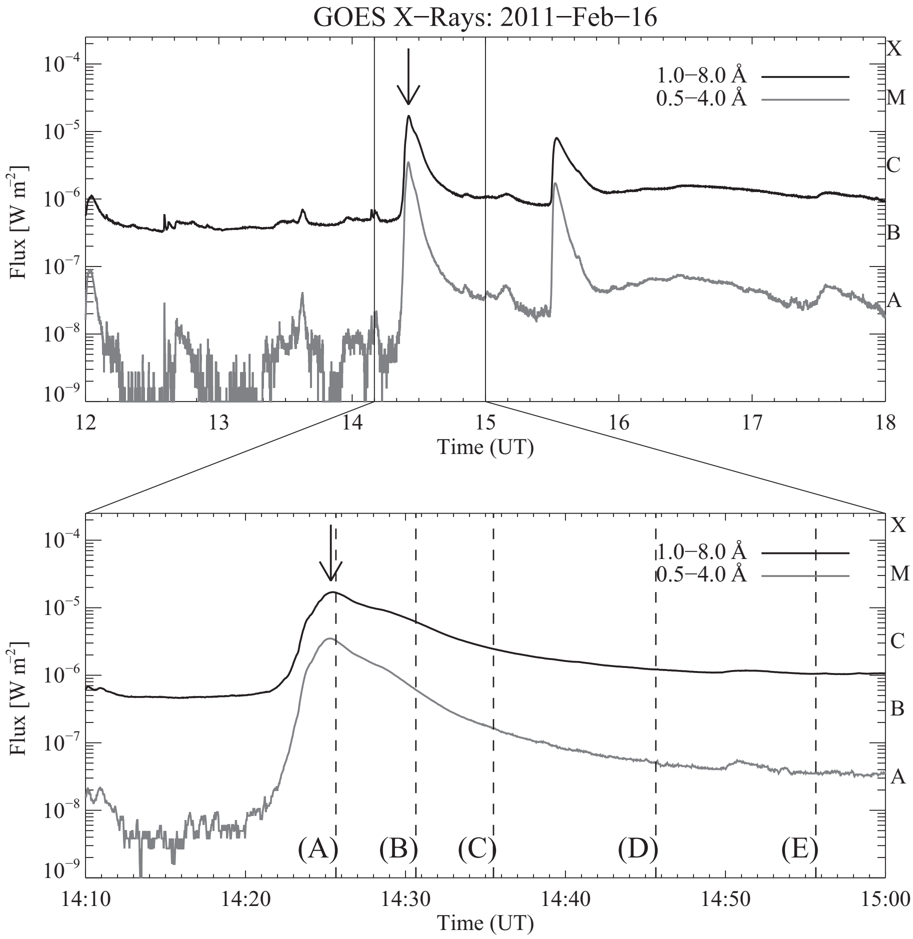

Figure 2.1: *GOES* X-ray emission at 1.0-8.0 Å and 0.5-4.0 Å channels of the 2011 February 16 flare (with extended time range at the top and an enlarged view in the bottom panel). The arrows indicate the peak of the M1.6 flare at 14:25:20 UT, which occurred in the Active Region NOAA 11158. The second peak at 15:32 UT in the top panel corresponds to a C7.7 flare that occurred in the same active region. The vertical dashed lines in the bottom panel point out the times of the images shown in Figures 2.5 and 2.6.

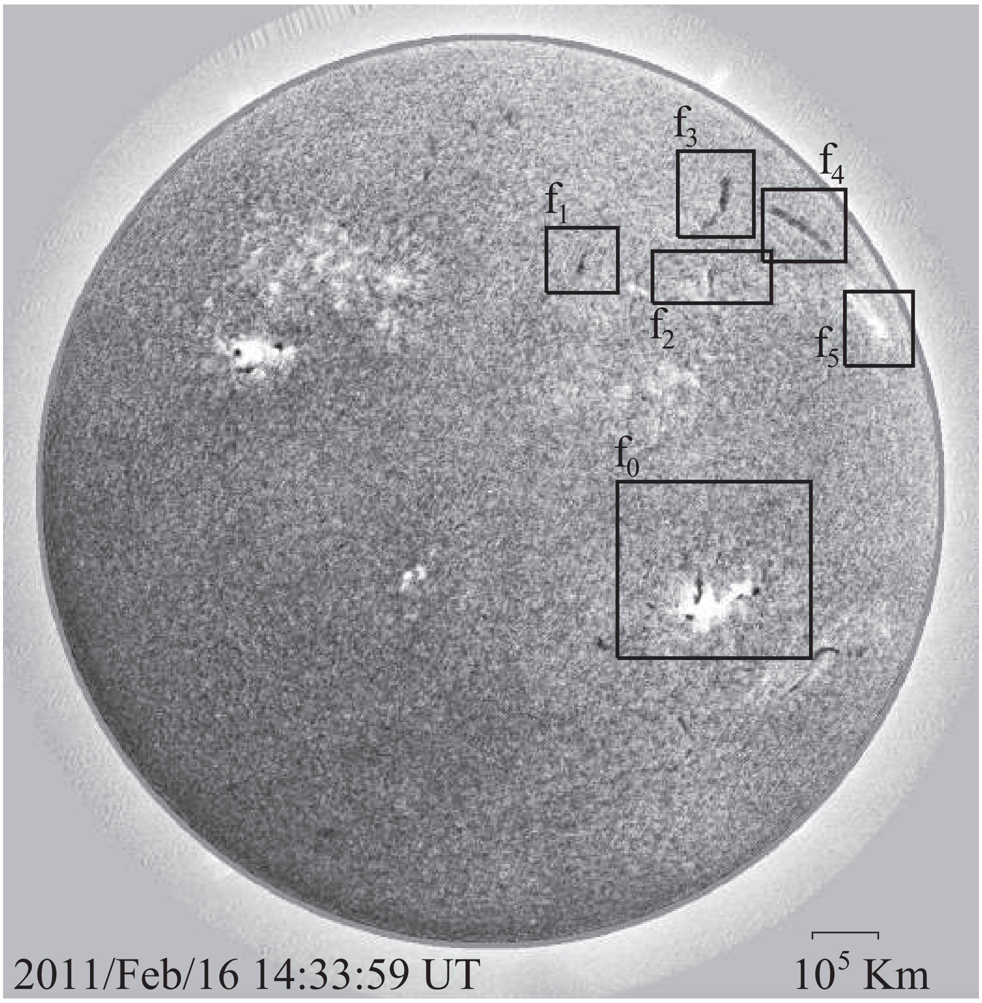

Figure 2.2: Full-disk solar image (solar north is up and west is to the right) of the flare in the Hα line center taken by the FMT at National University San Luis Gonzaga of Ica, Peru. The box f_0 shows the flaring region, whereas the fields of view f_1 to f_5 contain quiescent filaments. Filaments f_2 and f_5 are analyzed in more detail in Figure 2.7.

Relations Observatory (*STEREO*; Kaiser et al., 2008). AIA provides high-resolution full-disk images of the transition region and the corona at multiple wavelengths. We used AIA 171, 304, and mainly 193 Å images to investigate the evolution of the flare, the associated erupting filament, and the coronal waves. The temporal resolution of the AIA 193 Å data, which are attributed to the Fe XII line with the formation temperature of 1.25 MK, is 12 seconds, and the pixel size of the image is $0''.60$. At the time of the flare, *STEREO-A* was located 86.8° ahead of the Earth. *STEREO-A*/EUVI images at 195 Å, which again are mainly from the Fe XII line, have a temporal resolution and pixel size of 5 minutes and $1''.58$, respectively.

The flare was also captured in soft X-rays by the X-Ray Telescope (XRT; Golub et al., 2007) on board *Hinode*. XRT is sensitive to hot coronal plasma and can detect emissions from plasma with temperatures of the order of 1 to several tens of MK. We used partial images with $2''.5$ pixel resolution through the Thin-Be filter. In addition, to calculate the potential magnetic field, we used the Potential Field Source Surface (PFSS) extrapolation model[1] (Schrijver & DeRosa, 2003) that was applied to synoptic magnetograms taken by the Michelson Doppler Imager (MDI; Scherrer et al., 1995) on board *SOHO*, based on the LMSAL[2] forecaster program.

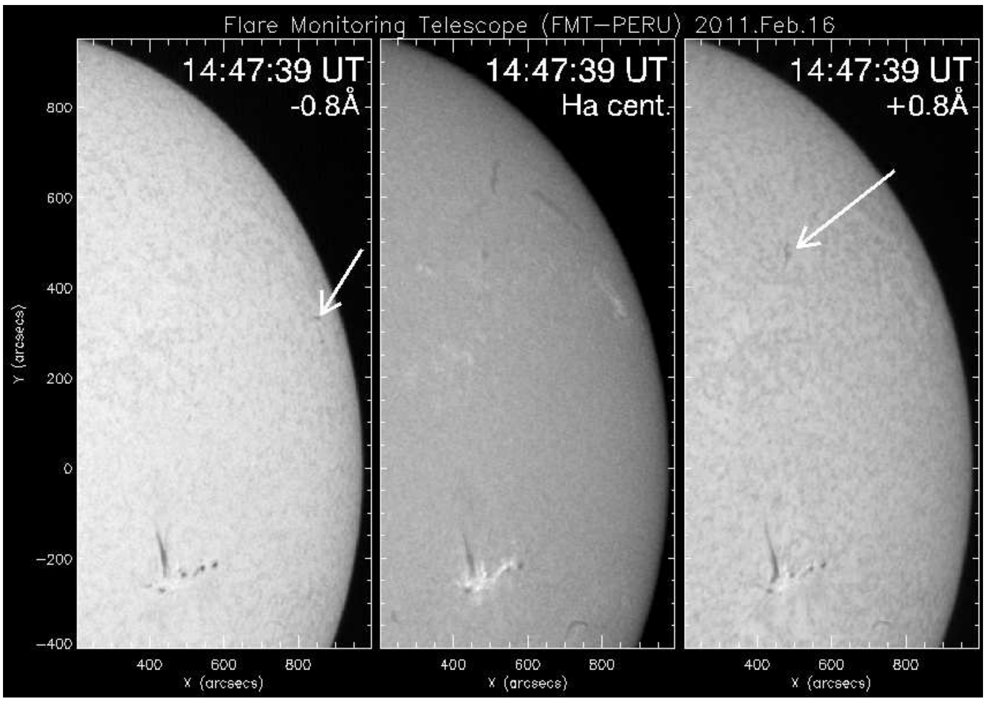

Figure 2.3: Filament eruption and the oscillating filaments (arrows), associated with the 2011 February 16 flare. Hα −0.8Å (left panel), Hα line center (middle panel), and Hα +0.8Å (right panel) images taken by FMT are shown.

[1]http://www.lmsal.com/~derosa/pfsspack/

[2]Lockheed Martin Solar and Astrophysics Laboratory

2.3 Analysis and Results

2.3.1 Overview of the Active Region and of the Flare

Figure 2.4 presents the temporal evolution of the flare at various wavelengths. Columns from left to right are images in soft X-rays Thin-Be filter, in EUV at 171 and 304 Å, and in the Hα line center; and were taken by XRT, AIA, and FMT, respectively. Before the flare starts, the so-called "sigmoid" or S-shaped magnetic field structure (e.g., Rust & Kumar, 1996; Canfield et al., 1999) that lies in the east-west direction is observed in soft X-rays (see top left panel in Figure 2.4).

During the time of the flare, NOAA 11158 was composed of several sunspots, as discussed in detail by Toriumi et al. (2013) and Sun et al. (2012). In particular, two neighboring fast flux emergences (P_0 - N_0 and P_1 - N_1 pairs) appeared in line along the east-west direction and formed a quadrupolar distribution (see top panel of the Hα -0.8 Å column in Figure 2.5). Between the following negative spot N_0 of the western bipole and the preceding positive spot P_1 of the eastern bipole, a prominent filamentary structure appeared along the magnetic neutral line on February 13, which developed for about three days. The X-class flare on February 15 occurred along the elongated neutral line between N_0 and P_1. This basic magnetic configuration remained even after the X-class flare and displayed the sigmoid structure seen in the XRT images.

The M-class flare in question, however, occurred at the eastern edge of the main neutral line between N_0 and P_1. When the impulsive phase of the flare just begins ($\sim$14:22 UT), a small bright X-ray feature appears at the eastern end of the sigmoid structure. The brightening has counterparts in the Hα and 304 Å images, which are mainly from footpoints of the flaring loops. As of 14:31 UT, the filament eruption can be distinguished in the EUV and Hα images (see bottom panels of Figure 2.4).

The starting point of the filament eruption is also located at the eastern edge of the neutral line between N_0 and P_1. This filament eruption is clearly discernible both in the Hα and EUV images, as shown in Figure 2.5. It was activated near 14:25 UT and displays an enlarging dark feature in the Hα blue-wing images, like a dandelion, whereas no manifestation is exhibited in Hα red-wing until 14:32 UT.

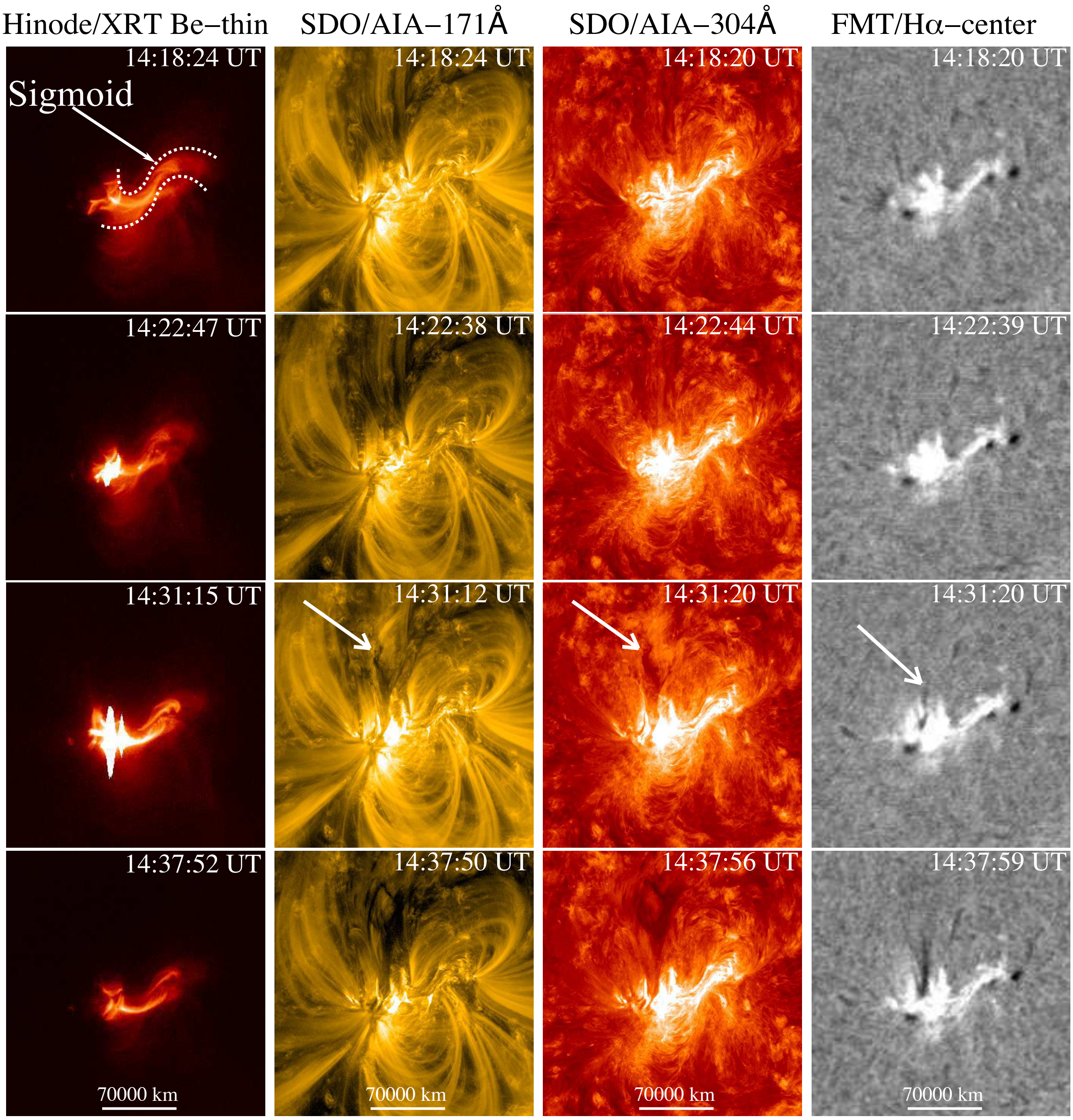

Figure 2.4: Multiwavelength time sequences of the 2011 February 16 flare. Columns from left to right are *Hinode* XRT Thin-Be broadband filter, *SDO*/AIA at 171 and 304 Å, and FMT Hα line center images. At 14:18 UT a sigmoid structure is clearly observed in the X-ray image, the dotted lines outline the sigmoidal shape prior to the flare. In the 171 Å, 304 Å, and Hα images a dark feature (filament eruption) becomes visible as of 14:31 UT. We pointed out the dark features with arrows.

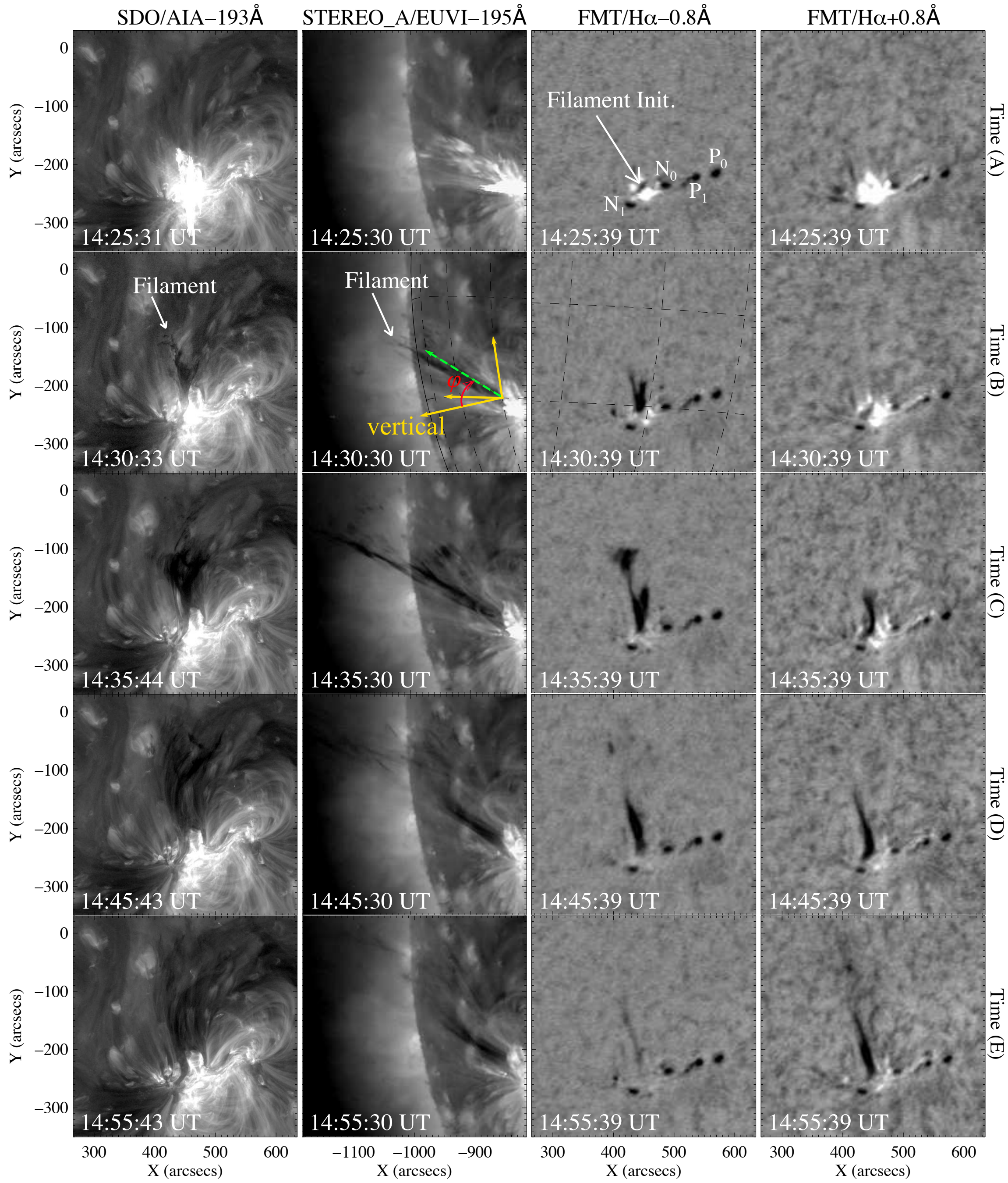

Figure 2.5: Temporal evolution of the filament eruption. From left to right: AIA 193 Å, EUVI 195 Å, and FMT Hα −0.8 and +0.8 Å images. The *STEREO-A*/SECCHI/EUVI images show the side view of the filament, since it was located 86.8° ahead of the Earth. The dashed green arrow at 14:30 UT points out the direction of the ejecta and the yellow arrows constitute the projected plane on the solar surface; φ is the inclination angle with respect to the vertical component normal to the solar surface. In the top panel of the third column, the arrow indicates the location of the erupting filament, whereas P_0, N_0, P_1, and N_1 denote the sunspots distribution.

2.3.2 Eruption of the Dandelion Filament

Here, we describe how we used Hα images to derive the three-dimensional velocity field of the erupting filament. For the line-of-sight (LOS) velocity, we modified the method by Morimoto & Kurokawa (2003a). They computed the LOS velocities of erupting filaments observed with FMT by using the method based on the Beckers' cloud model (Beckers, 1964; Mein & Mein, 1988). Morimoto & Kurokawa (2003a) adopted the single cloud model. Because FMT has only three (center and ± 0.8 Å) wavelength data points for the four unknowns (source function, optical depth, Doppler velocity, and Doppler width) of a cloud, they further assumed a fixed Doppler width in their calculation. Our method, on the other hand, deals even with the Doppler width as a free parameter. This can be implemented as follows: in the quiescent phase of the filament, we derived the parameters assuming the value of the Doppler width, as was done in Morimoto & Kurokawa (2003a). To analyze a time series, we search for the best-fit solution around the quiescent parameter values found in the initial time step, and select the "nearest" local minimum in the parameter field. This selection of the nearest values is based on the assumption that the physical parameters in a single cloud do not change so quickly. Next, we search the parameters in the next time step around the parameters derived in the previous time step, and so on. We did not set a "pre-defined range" in our method, we used the hybrid method for the fitting (Powell, 1970). The error of the derived LOS velocity is roughly comparable with the errors obtained with the method of Morimoto & Kurokawa (2003a) and is about ± 10 km s^{-1}, while the derived LOS velocity tends to be overestimated for the fixed Doppler width, since the Doppler width is thought to be larger for an erupting filament. The error could be, however, a little worse due to misalignment of the wavelengths of the FMT filters from the nominal values. Comparing the wing data, the wavelength of the red-wing ($+0.8$ Å) seems to be set closer to the line center than that of the blue-wing (-0.8 Å). The error of the LOS velocity, therefore, is roughly ± 15 km s^{-1}.

The left column in Figure 2.6 shows the derived temporal evolution maps of the LOS velocity. The colors show blueshift (i.e., moving toward us) and redshift (i.e., moving away from us) of the filament. Near 14:30 UT, the filament begins to erupt northward and simultaneously shows blueshift features, especially at the leading part, with a LOS velocity of about -30 km s^{-1}. At the root of the filament, in contrast, it shows a redshift with a velocity of about 20 km s^{-1}. The filament eruption is clearly seen until 14:35 UT. At this time, the LOS velocity at the leading edge is nearly -25 km s^{-1}. Next, the front edge gradually becomes invisible at 14:45 UT, whereas near 14:55 UT, the filament shows a dominant redshift pattern. The observed blueshift velocity of about -30 km s^{-1} is slightly larger than the result by Veronig et al. (2011), while the temporal evolution is roughly consistent.

We confirm the temporal LOS motion with the side views of the filament eruption observed from *STEREO-A*, since it was located at 86.8° ahead of the Earth. In the EUV 195 Å images of *STEREO-A*/SECCHI/EUVI, we see movement of the cold plasma as a dark feature (second column in Figure 2.5). The dark feature is ejected from the flare site, and the traveling velocity of the front (i.e., the fastest) part is about 280 km s^{-1}. The horizontal component of the velocity (i.e., the velocity in the direction from the Sun to the Earth) is about 230 km s^{-1}. FMT cannot detect clouds with velocity greater than 50 km s^{-1}, because the wavelengths of the wing data are set at ± 0.8 Å. Therefore, FMT missed the front part of the ejection.

By comparing the EUVI 195 Å and FMT Hα -0.8 Å images (Figure 2.5), the Hα filament seems to correspond to the main (i.e., the darkest) part of the filament in the 195 Å images. The main part of the filament has a velocity of about 110 km s^{-1}, and the horizontal component has a velocity of about 90 km s^{-1}. The velocity is much larger than the LOS velocity derived by FMT (30 km s^{-1}). LOS velocities derived from the cloud model reflect representative values of moving clouds, and the fine LOS velocity field in the clouds could be lost. Besides, the velocity in the Earth-Sun direction is derived by following dark features seen in EUVI images, and is not derived by tracing the moving ejecta. Alternatively, we could detect a slower component of the erupting filament, because the velocity of about 90 km s^{-1} far exceeds the detection limit of FMT.

For the tangential velocity of the erupting filament (i.e., the velocity of the filament in the plane of the sky), we traced the apparent motion of filament blobs by using the local correlation tracking (LCT) method. The middle column in Figure 2.6 shows the temporal evolution of the erupting filament with arrows that show the orientation and magnitude of the tangential velocity. The filament blobs are moving upward (i.e., northward) with a tangential velocity of about 10 km s^{-1}. The dark feature seen in EUVI 195 Å images has a northward velocity of about 65 km s^{-1}, which is faster than the tangential velocity derived from FMT. This result is explained by the excessively large mesh size used for the LCT method, which means that features moving at such high speed could not be detected even if they were present. The seeing condition prevents us from reducing the mesh size for the FMT images. Therefore, the derived tangential velocity is a somewhat averaged value of the main part of

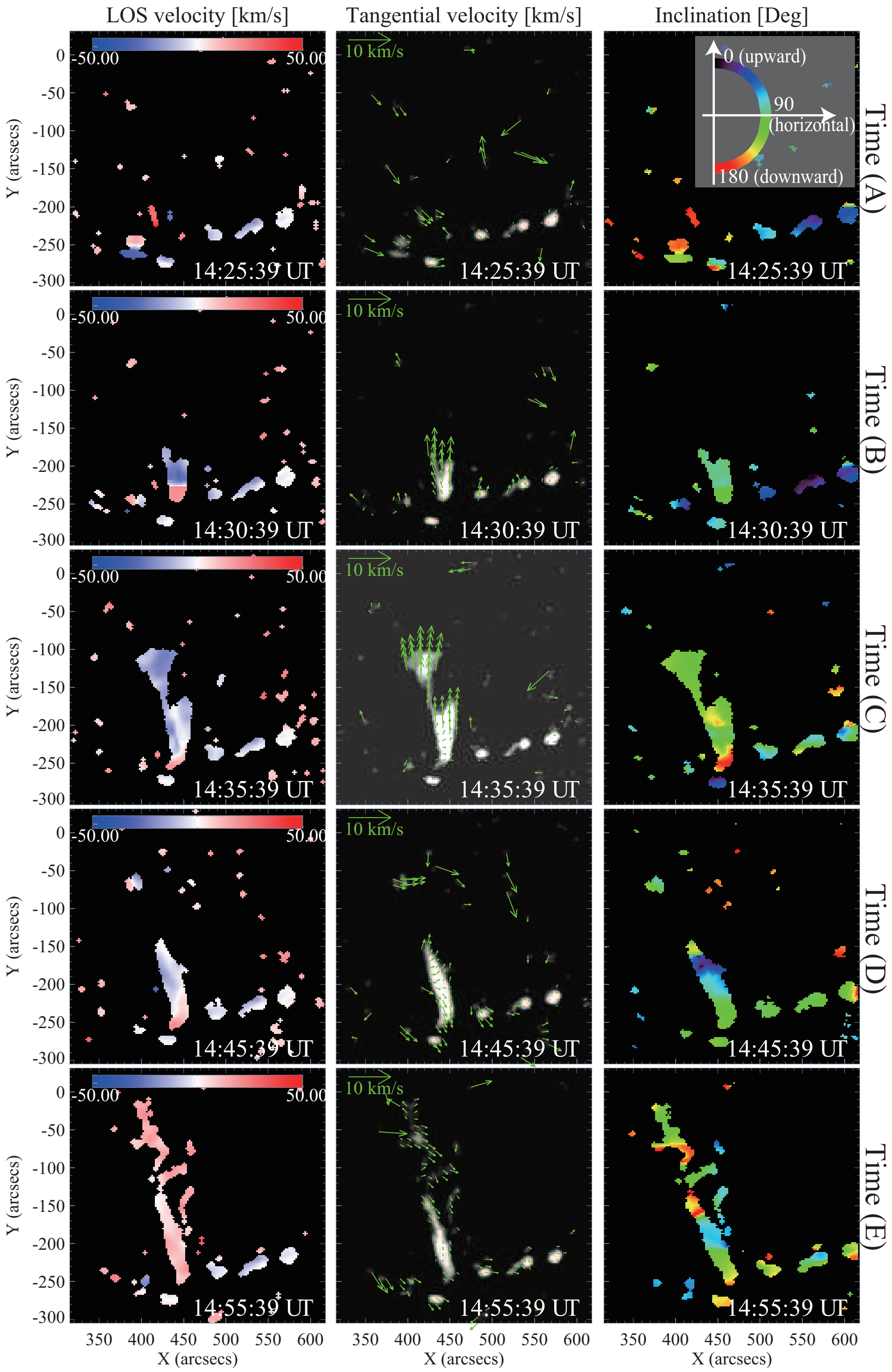

Figure 2.6: Line-of-sight (LOS) velocity (left column), tangential velocity (middle column), and inclination (right column) maps of the erupting filament. The LOS velocity was obtained by calculating the Hα profile based on the cloud model. The tangential velocity was calculated by tracing the motion of the internal structures in successive images. The inclination is the result of the coordinate transformation of the velocity vectors and corresponds to the top view of the filament, which is normal to the solar surface.

the ejected filament.

In the right column of Figure 2.6, we show the temporal evolution of the inclination of the ejecta. The inclination angle is set to zero for the upward direction normal to the solar surface. In the early phase of the ejection (around 14:30 UT), the direction is nearly horizontal with respect to the solar surface, with a slight upward inclination. During the main phase of the ejection, which occurs around 14:35 UT, the direction is still nearly horizontal but with a slight downward inclination. Next, the inclination distribution becomes complex showing upward and downward motions, probably because of the coexistence of upward and downward moving features in the later phase. Although the error in the velocity measurements is probably large, we believe that the ejecta move nearly horizontally with respect to the solar surface. Furthermore, in Figure 2.5 (EUVI panel at 14:30 UT), we depict the plane of the solar surface (yellow arrows over the heliographic coordinates) and a vertical component perpendicular to the surface (arrow labeled "vertical"). The dashed green arrow highlights the direction of the filament eruption as seen by *STEREO-A*, and φ is the inclination angle with respect to the vertical on the solar surface. From EUV observations (193 and 195 Å) we infer the geometrical components of the erupting material, which leads us to estimate $\varphi \approx 58°$. So the filament in EUVI was ejected having an elevation angle of about 32°.

2.3.3 Filament Oscillations and EUV Waves

In the Hα data, we also observe winking (activation and/or oscillation) of filaments associated with the flare. As we see in Figure 2.2, some filaments are labeled f_1 to f_5. These filaments are located far from the flare site. We identify a clear winking feature for filament f_2 and a much fainter signature for filament f_5 (see also the Figure 2.3).

The time series of the winking filament f_2 is displayed in Figure 2.7(a) at Hα -0.8 Å (left), Hα center (middle), and Hα $+0.8$ Å (right) wavelengths. The field of view of the f_2 region is the same as in Figure 2.2. At 14:40 UT, the filament starts winking. First, a dark feature becomes prominent in red-wing images, as shown by the arrow labeled $2r$ in Figure 2.7(a). The feature is dominant until 15:05 UT, and then it fades slowly away. However, at about 14:50 UT, a dark structure starts to appear in the blue-wing images, as pointed out by another arrow ($2b$). This structure is noticeable until 15:10 UT, when it disappears. In the Hα center, in contrast, no significant changes are observed.

Figure 2.7(c) plots the temporal variations of the intensities calculated for the f_2 region at three wavelengths. In the red-wing plot (dash-dotted line), we clearly identify a decrease of the intensity associated with the appearance of the dark feature in the red-wing images. The decrease starts at about 14:36 UT and reaches a maximal depletion around 14:45 UT, after which it recovers. The signal in the blue-wing plot (dotted line), however, remains roughly constant until 14:55 UT and then starts to decrease gradually. In the Hα center plot (solid line), the signal slightly increases.

A similar analysis for filament f_5 is presented in Figures 2.7(b) and (d). Unlike f_2, the dark structure appears mainly in the blue-wing (left panels). The dark feature is evident from 14:40 UT until 15:05 UT. Conversely, at 15:00 UT, we recognize a very weak feature in the red-wing (see arrow labeled $5r$ in Figure 2.7(b)). The temporal variation of the intensities is plotted in Figure 2.7(d). The winking feature dominates during the darkening in the blue-wing plot (dotted line), whereas the red-wing (dash-dotted line) and Hα center (solid line) plots show gradual variation and no clear signals caused by the filament oscillation. For the other filaments f_1, f_3, and f_4, we verified the intensity profiles and found no winking patterns.

We also examine the temporal evolution of the coronal waves associated with the 2011 February 16 flare and the relation with the oscillating filaments. The time sequences of the EUV waves produced by the flare are presented in the top panels of Figure 2.8 (panels a–d). These are AIA 193 Å running difference (20 minutes difference) images. The white arrows highlight the moving wavefronts, whereas the locations of the oscillating filaments f_2 and f_5 are marked by the boxes. The distances of the filaments (f_2 and f_5) measured from the flare site along the spherical solar surface are $\approx 5.1 \times 10^5$ and $\approx 6.4 \times 10^5$ km, respectively. We derive the speeds of the EUV wave by following the leading edge of the wave fronts consecutively along the spherical lines to the filaments f_2 (path 2) and f_5 (path 1) directions. The mean velocities computed from a linear fitting are 430 ± 29 km s^{-1} and 672 ± 24 km s^{-1}, respectively. The EUV wave have been studied by several authors (Harra et al., 2011; Veronig et al., 2011; Long et al., 2013; Nitta et al., 2013), and the propagating speed ranges from 500 to 700 km s^{-1}, which changes depending on the propagating direction. Therefore, the velocities derived in this study are comparable with those results.

At 14:28 UT (Figure 2.8a), a well-defined wave front propagates mainly toward the north, and a bright erupting material is observed that corresponds to the dandelion filament. At about 14:31 UT (Figure 2.8b), the central part of the wave front seems to stop and to exhibit a stronger amplitude: this occurs just when the wave is approaching the edges of a weak

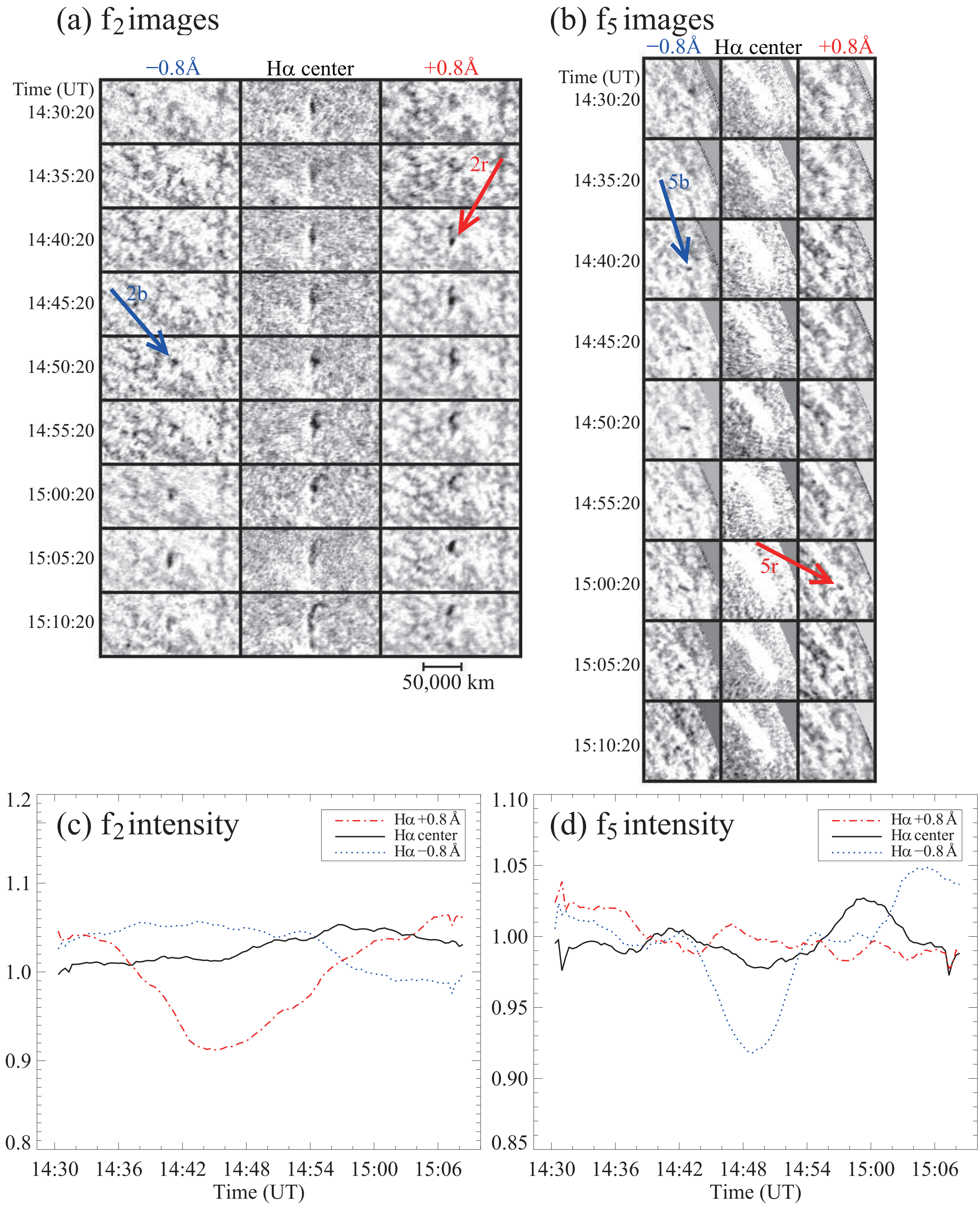

Figure 2.7: (a), (b) Hα images: Hα −0.8 Å (left), Hα center (middle), and Hα +0.8 Å (right) of the oscillating filaments f_2 and f_5, respectively. The field of view is shown in Figure 2.2. The arrows indicate the starting time of the oscillation both in Hα +0.8 Å (labeled $2r$ and $5r$) and Hα −0.8 Å ($2b$ and $5b$). (c), (d) Time profiles of intensities for regions f_2 and f_5, respectively. The horizontal axis is the time in UT, and the vertical axis is the normalized intensity. The solid, dotted, and dash-dotted lines are the intensities in the Hα center, −0.8 Å, and +0.8 Å, respectively.

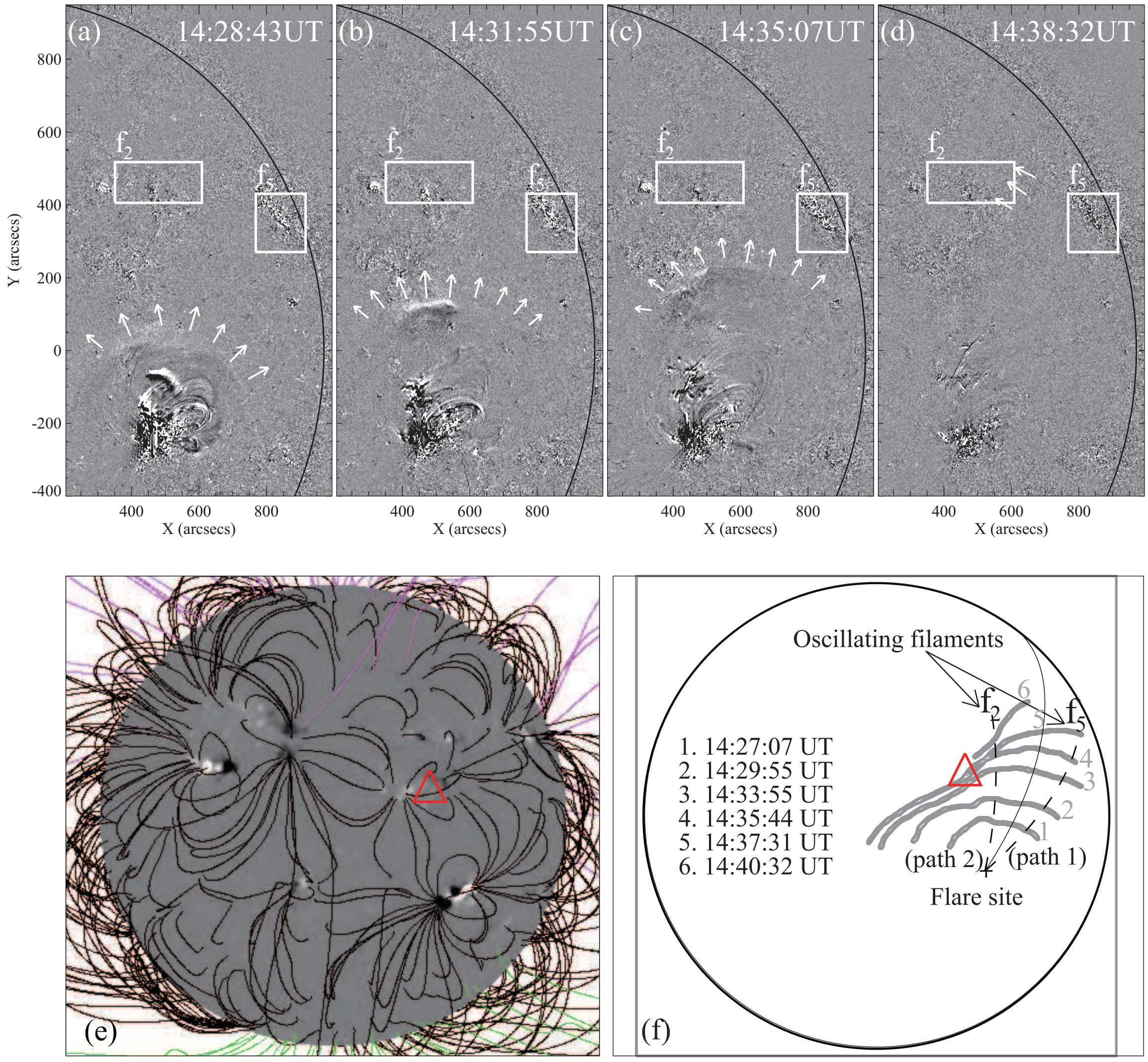

Figure 2.8: (a) – (d) Time sequences of running difference images of the *SDO*/AIA 193 Å images. The regions of the Hα filaments f_2 and f_5 are marked by the rectangles. (e) Potential magnetic field configuration extrapolated on *SOHO*/MDI magnetogram based on the PFSS model. The red triangle denotes the location of the weak active region. (f): A schematic illustration of the coronal wave progression and its interaction with the filaments f_2 and f_5. The gray strokes outline the wave fronts at the given time and the arrows indicate the filaments' position.

active region that is located north of NOAA 11158. The observed enhanced pattern and the changes in the wave front progression are tentatively attributed to the plasma compression generated by the interaction between the coronal wave and the confined magnetic system of the active region (Uchida, 1974). We plot the potential magnetic field configuration derived from *SOHO*/MDI in Figure 2.8(e). The red triangle indicates the location of the northern weak active region. We confirm that the propagating wave front tends to stop there. Note that, at 14:35 UT (Figure 2.8c), the leading part of the wave front decelerates, perhaps retained by the magnetic field configuration, whereas the west part is slightly refracted and continues traveling northwest (Figure 2.8d).

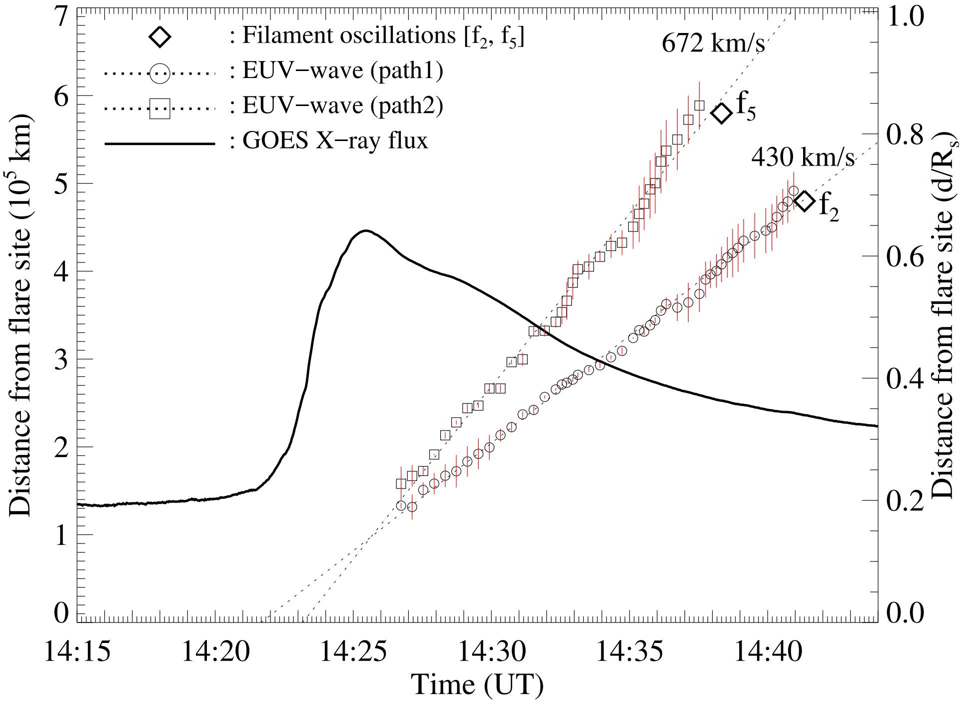

Figure 2.9: Time-distance diagram of the EUV wave and oscillating filaments f_2 and f_5, measured along the paths shown by the dashed lines in Figure 2.8(f). The diamonds $\diamondsuit$ mark the position of filaments f_2 and f_5, whereas the wavefront distances at given time are represented by $\circ$ and $\square$ together with the standard deviation (error bars) along paths 1 and 2, respectively. R_s is the solar radius (≈695 800 km). For comparison, we also plot the *GOES* X-ray flux in the 1.0-8.0 Å channel (solid line).

Figure 2.8(f) shows the progression of the most prominent fronts of the EUV wave from 14:27 to 14:40 UT, the positions of the weak active region, and the oscillating filaments f_2 and f_5. At 14:37 UT, the wavefront labeled 5 approaches f_5 and, at 14:40 UT, the wave front 6 reaches f_2. These times are consistent with those identified both in the images and in the intensity plots of f_2 and f_5 (Figure 2.7). Figure 2.9 presents the time-distance diagram of these temporal behaviors. We measured the temporal evolution of the wave fronts along the paths, as shown by the projected dashed lines in Figure 2.8(f). The squares ($\square$) and circles ($\circ$) plotted together with a linear fit (dotted lines) in Figure 2.9 show the times and the positions of the wavefronts as they move along paths 1 and 2, respectively. Diamonds ($\diamond$) indicate the oscillating filaments f_5 and f_2, which are on a straight line, as shown by the dotted lines. Therefore, the observed winking filaments are assumed to have been triggered by the passage of the EUV coronal wave.

2.4 Summary and Conclusions

We observed a filament eruption shaped like a dandelion and associated with the flare that occurred at NOAA 11158. We analyze the Hα images taken by FMT in Peru and derive the three-dimensional velocity field by using a new method. To derive the LOS velocity, we use the modified cloud model that was originally developed for the FMT data by Morimoto & Kurokawa (2003a). We compare the temporal behavior of the erupting dandelion filament with its EUV side views observed by *STEREO-A*/SECCHI/EUVI. We realize that the LOS velocity derived from the Hα images of FMT gives representative values of the moving clouds and that the very fast components seen in the *STEREO-A*/EUVI images are probably lost due to the detection limit of FMT. The tangential velocity of the dandelion filament is derived by applying the local correlation tracking (LCT) method to the Hα images. We derive a representative (averaged) tangential velocity of the main part of the filament, although we could not capture small fast-moving features, if they exist, because of the limited mesh size of the LCT method. By combining these LOS and tangential velocities, and applying a coordinate transformation, we also derive the inclination of its velocity vectors. We confirm that the dandelion filament is ejected nearly horizontally with respect to the solar surface.

We also observe the winking of Hα filaments that are located far from the flare site, and examine the relation between the winking filaments and the EUV coronal wave associated with the flare. As summarized in Figures 2.8 and 2.9, Hα filaments f_2 and f_5 start oscillating when the EUV coronal wave arrives, so we confirm that the interaction between the EUV wave and the Hα filaments causes the filaments to wink.

The derived traveling speed of the observed EUV waves is about 430 to 672 km s^{-1}. Associated with this flare, Type II radio burst was also observed (Harra et al., 2011; Nitta et al., 2013). These results are a strong indication that the observed EUV waves are MHD fast-mode waves or shocks. Moreover, we observed the filament eruption ejected tangentially to the solar surface. This seems to be suitable to generate a Hα Moreton wave, because the wavefront could easily make contact with the chromospheric plasma, even if a shock front is generated only in some restricted range at the front of the ejected filament. Nevertheless, we do not observe a Moreton wave associated with the flare. This is probably because the downward velocity of the wave front is small (about 20 km s^{-1}) toward the solar surface, as reported by Harra et al. (2011) and Veronig et al. (2011), and probably because the EUV coronal wave (or shock) is not strong enough to generate an observable Moreton wave in the Hα band.

We derived the three-dimensional velocity field of the filament eruption. We could follow the temporal evolution of the velocity field and inclination of the ejecta. We also examined the temporal behavior of the EUV waves associated with the filament eruption. These provide us with an overall picture on the development of the EUV coronal wave and a filament ejection. Although FMT may have missed capturing very fast components, the close correlation in time and the main direction of the EUV wave progression with those of the filament eruption leads us to conclude that the filament is the driver of the observed EUV wave. Although the work we did by measuring the three-dimensional velocity field of the erupting filament and examining the relation between velocity fields and coronal EUV wave showed a direct link among both phenomena, further studies are needed to fully understand filament eruptions as a driver of coronal EUV waves and CMEs. Statistical studies to derive the tendency of filament eruptions to generate coronal waves and/or CMEs could be useful for this.

References

Beckers, J. M., 1964, PhD Thesis, University of Utrecht

Canfield, R. C., Hudson, H. S., Mackenzie, D. E., 1999, GeoRL, 26, 627-630

Eto, S., Isobe, H., Narukage, N., et al., 2002, PASJ, 54, 481-491

Golub, L., Deluca, E., Austin, G., et al., 2007, SoPh, 243, 63-86

Harra, L. K., Sterling, A. C., Gömöry, P., Veronig, A., 2011, ApJL, 737, L4

Howard, R. A., Moses, J. D., Vourlidas, A., et al., 2008, SSRv, 136, 67-115

Kaiser, M. L., Kucera, T. A., Davila, J. M., St. Cyr, O. C., Guhathakurta, M., Christian, E., 2008, SSRv, 136, 5-16

Kosugi, T., Matsuzaki, K., Sakao, T., et al., 2007, SoPh, 243, 3-17

Kurokawa, H., Ishiura, K., Kimura, G., Nakai, Y., Kitai, R., Funakoshi, Y., Shinkawa, T., 1995, J. Geomag. Geoelectr., 47, 1043-1052

Lemen, J. R., Title, A., Akin, D. J., et al., 2012, SoPh, 275, 17-40

Long, D. M., Williams, D. R., Régnier, S., Harra, L. K., 2013, SoPh, 288, 567-583

Mein, P., Mein, N., 1988, A&A, 203, 162-169

Morimoto, T. & Kurokawa, H., 2003a, PASJ, 55, 503-518

Morimoto, T. & Kurokawa, H., 2003b, PASJ, 55, 1141-1151

Nitta, N.V., Schrijver, C.J., Title, A.M., Lui W., 2013, ApJ, 776, 58(13pp)

Pesnell, W. D., Thompson, B. J., Chamberlin, P. C., 2012, SoPh, 275, 3-15

Powell, M.J.D., 1970, A Hybrid Method for Non-Linear Equations, Ed.: Gordon & Breach

Rust, D. M., Kumar, A., 1996, ApJ, 464, L199-L202

Scherrer, P. H., Bogart, R. S., Bush, R. I., et al., 1995, SoPh, 162, 129-188

Schrijver, C. J., DeRosa, M. L., 2003, SoPh, 212, 165-200

Sun, X., Hoeksema, T., Liu Y., Wiegelmann T., Hayashi, K., Chen, Q., Thalmann, J., 2012, ApJ, 787, 77

Toriumi, S., Iida, Y., Bamba, Y., Kusano, K., Imada, S., Inoue, S., 2013, ApJ, 773, 128

Uchida, Y., 1974, SoPh, 39, 431-449

UeNo, S., Shibata, K., Kimura, G., Nakatani, Y., Kitai, R., Nagata, S., 2007, Bull. Astr. Soc. India, 35, 697-704

Veronig, A. M., Gömöry P., Kienreich, I. W., Muhr, N., Vršnak, B., Temmer, M., Warren P. H., 2011, ApJL, 743, L10

Chapter 3

Dynamic Processes of the Moreton Wave on 2014 March 29

3.1 Motivation

The discovery of a large chromospheric disturbance associated with a flare by Moreton (1960) and Moreton & Ramsey (1960), opened the door to new research fields in the late of 1960'. Although in the past decades important progresses have been achieved, still remain some unanswered questions about chromospheric disturbances triggered by flares. It is currently almost well established that a large-scale disturbance in the chromosphere, commonly termed as "Moreton wave", appears in connection with strong flares, and shock waves in the corona; but interestingly the Moreton wave only is observed in some occasions, which is puzzling. So, the natural question that arises here is: what is the difference between flares and/or shock waves with and without Moreton waves? It is argued that when the shock wave in the corona is strong enough, it could easily make contact with the plasma in the chromosphere and as a result one would expect to observe a Moreton wave. However, quantifying the strength of the shock in the corona is not straightforward, but when multiwavelength observations of a large-scale disturbance in the solar atmosphere are available, it is possible to investigate the shock propagation in the corona and the reaction of the underlying chromosphere.

In this Chapter we present a detailed study of a Moreton wave associated with a X1.0-class solar flare that occurred on 2014 March 29. The flare and the Moreton wave were successfully captured in multiwavelength imaging in the Hα line (H$\alpha \pm 0.8$ Å) by the Flare Monitoring Telescope (FMT). We analyze the dynamic of the Moreton wave with special emphasis on the Doppler characteristics, which enabled us to quantify and discuss the downward/upward motion of the plasma in the chromosphere caused by the wave propagation. One of our important findings is that the plasma moving downward at the front of the Moreton wave attains a maximum velocity of about 4 km s^{-1}, whereas the propagation speed ranges between 640 and 859 km s^{-1}. Furthermore, using the weak-shock approximation in conjunction with the velocity amplitude of the chromospheric motion induced by the Moreton wave, we derive the Mach number of the incident shock in the corona. We also used the MHD linear theory to infer the plasma velocity in the corona and its relation with the chromospheric disturbance. In addition, we performed the temperature-emission measure analysis of the coronal wave based on the SDO/AIA observations, which allowed us to estimate the compression ratio distribution, and to derive the Alfvén and fast-mode Mach numbers. These results led us to discuss the characteristics of the shock front and the interaction with chromospheric plasma.

3.2 Observations and Data

The 2014 March 29 flare is one of the best observed events because it was captured in a wide range of wavelengths with unprecedented temporal and spatial resolution by advanced space-borne and ground-based instruments. This powerful flare classified as X1.0 on the *GOES* scale occurred in active region 12017 (N11, W32), and was accompanied by various associated phenomena: fast-filament eruption, chromospheric evaporation, large-scale propagating disturbance in the corona and the chromosphere, filament activation/oscillation, and ultimately a CME.

The Moreton wave on 2014 March 29, was detected in high cadence images obtained by the Flare Monitoring Telescope (FMT: Kurokawa et al., 1995; UeNo et al., 2007; Shibata et al., 2011), which is in operation at National University San Luis Gonzaga, Ica, Peru. The FMT provides simultaneous full-disk solar images at several wavelengths: the Hα line center (6562.8 Å), Hα -0.8 (6562.0 Å; blue wing) and Hα $+0.8$ (6563.6 Å; red wing), and continuum (6100 Å), also in prominence mode (Hα line center with occulting disk), with a time cadence of 20 s and spatial sampling of $\sim 2''\!.0$ pixel^{-1}. These characteristics make the FMT a suitable instrument for detecting Moreton waves (e.g., Eto et al., 2002; Narukage et al., 2002, 2004), for deriving the velocity field of filament eruptions (e.g., Morimoto & Kurokawa, 2003a,b; Morimoto et al., 2010; Cabezas et al., 2017), and for studying the long-term variation of UV radiation (S. UeNo et al. 2019, in prep). Because Moreton waves are best observed in the wing of the Hα line (see Moreton & Ramsey, 1960; Narukage et al., 2008; Chen et al., 2005), for the analysis we made use of the FMT wing (red and blue) observations. This further enabled us to investigate the Doppler characteristics of the Moreton wave.

In Figure 3.1(a) we present a full-disk time-difference image at Hα +0.8 Å (red wing), taken by the FMT on 2014 March 29 at 17:49:20 and 17:49:59 UT. The Moreton wave is clearly seen as an arc-shaped front propagating northeast from the flare site following a trajectory of a solid angle. The great-circle dashed lines projected onto the solar surface outline the paths P_1, P_2, P_3, and P_4 that we considered in our analysis to estimate the horizontal propagation speed of the Moreton wave and to derive the velocity amplitude in the chromosphere. Figure 3.1(b) shows the soft X-ray flux by *GOES* together with the hard X-ray emission by *RHESSI* in the energy range 25–50 keV. According to the *GOES* plot, which is predominantly thermal emission from the corona, the flare started at ∼17:35:30 UT reaching its maximum at ∼17:48:00 UT; whereas the *RHESSI* profile shows a different behavior during the impulsive and the main phase of the flare because it results from non-thermal bremsstrahlung emission. Figure 3.1(b) also indicates the time period at which the Moreton wave is observed, as represented by the gray shaded area extending from 17:45:20 to 17:53:20 UT.

The coronal wave associated with the flare under study was captured in X-ray wavelength by the X-Ray Telescope (XRT; Golub et al., 2007) on board the *Hinode* satellite (Kosugi et al., 2007). We use full frame images through the Ti-poly filter with a temporal resolution of ∼40 s and pixel size ∼8$''\!.$2 pixel^{-1}, and partial images in Al-poly and Be-thin filters with a temporal resolution and spatial sampling of ∼1 min and ∼1$''\!.$0 pixel^{-1}. The XRT channels are sensitive to very hot coronal plasma capable of detecting emission from ∼1 to more than 10 MK. For our study we also used extreme ultraviolet (EUV) data taken by the Atmospheric Imaging Assembly (AIA; Lemen et al., 2012) on board the *Solar Dynamics Observatory* (*SDO*; Pesnell et al., 2012). We examine the morphology and the kinematics of the coronal wave by using emission lines at 304, 211, and 94 Å, which are dominated by He II ($\log T \sim 4.7$), Fe XIV ($\log T \sim 6.3$), and Fe XVIII ($\log T \sim 6.8$), respectively. To characterize the local plasma responses to the EUV wave passage, we carry out differential emission measure (DEM) analysis based on the method introduced by Cheung et al. (2015). We performed DEM maps using six AIA (94, 131, 171, 193, 211, and 335 Å) coronal temperature data, with full cadence (12 s) and spatial sampling of ∼ 0$''\!.$6 pixel^{-1}.

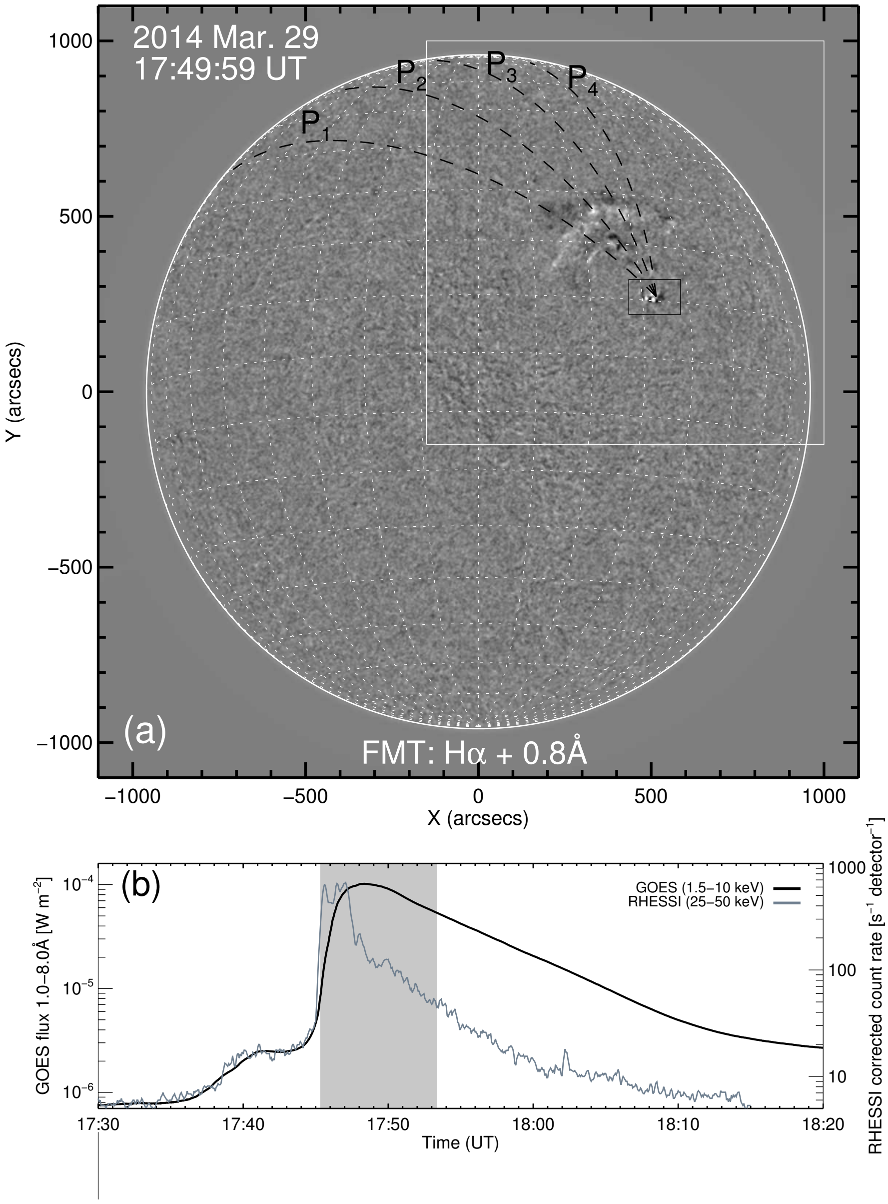

Figure 3.1: (a) Time-difference image of the full-disk Sun at Hα +0.8 Å captured by the Flare Monitoring Telescope (FMT) on 2014 March 29 at 17:49:59 UT. The image was subtracted with its precedent taken at 17:49:20 UT. The dashed black lines labeled P_1, P_2, P_3, and P_4 projected onto the solar surface outlines the paths along which the analysis of the Moreton wave is performed. The black rectangle marks the flare site, while the large white box depicts the field of view presented in Figure 3.2. (b) *GOES* X-ray emission at 1.0–8.0 Å (1.5–10 keV, black solid line) and *RHESSI* count rate (25–50 keV, gray solid line) of the X1.0 flare. The shaded area starting from 17:45:20 to 17:53:20 UT denotes the time period at which the wave front is identified in our Hα data.

3.3 Wave Morphology and Kinematics

The morphology of the Moreton wave and its associated coronal counterpart is characterized by performing running-difference maps, while the kinematics is inferred from intensity variation through artificial slits and by carrying out time-distance measurements of the wave front. For the kinematics we take into account the great-circle paths P_1–P_4 (shown in Figures 3.1, 3.2), projected over an angular extent on the solar surface in the wave propagation direction.

3.3.1 Morphology

Figure 3.2(a)-(c) show time-difference coronal counterpart images of the Moreton wave on 2014 March 29 in X-ray channel (Ti-poly), in the EUV band at 94 Å, and a composite tri-color image (RGB = 211, 193, and 171 Å), respectively. For comparison we also include time-difference images in He II (304 Å)(panel d) and Hα $\pm$0.8 Å (panels e, f) to see how the different layers of the solar atmosphere respond to the effects of the wave propagation. As the temperature changes from hot to cool, the disturbance develops differently, exhibiting several aspects and components of the coronal wave.

In X-ray and 94 Å (Figure 3.2a, b) the morphology of the coronal wave is quite similar in space and time, both representing emissions of hotter coronal plasma >6.0 MK. In Figure 3.2(c), which is a composite map of warm (211, 193 Å) and cool (171 Å) AIA channels, a dome-shaped structure similar to a shock propagating ahead of the disturbed surface or its footprint is visible, the latter predominantly seen in the cool channel. In much cooler line, i.e., He II (Figure 3.2d), which provides diagnostics of the upper chromosphere and the transition region ($\sim 5 \times 10^4$ K), only the footprint of the coronal wave is clearly observed as a bright arc-like feature moving toward the northeast. This thin layer might be strongly affected by the pressure excess created by the globally propagation shock in the corona, resulting in this enhanced emission. On the other hand, the signature of the disturbance in the wing of the Hα line at $\pm$0.8 Å (Figure 3.2e, f) appears more diffuse and somewhat similar in morphology to that in He II line. Naturally, the change observed in Hα indicates an increase in the local Doppler velocity, and this aspect is addressed in Section 3.4.

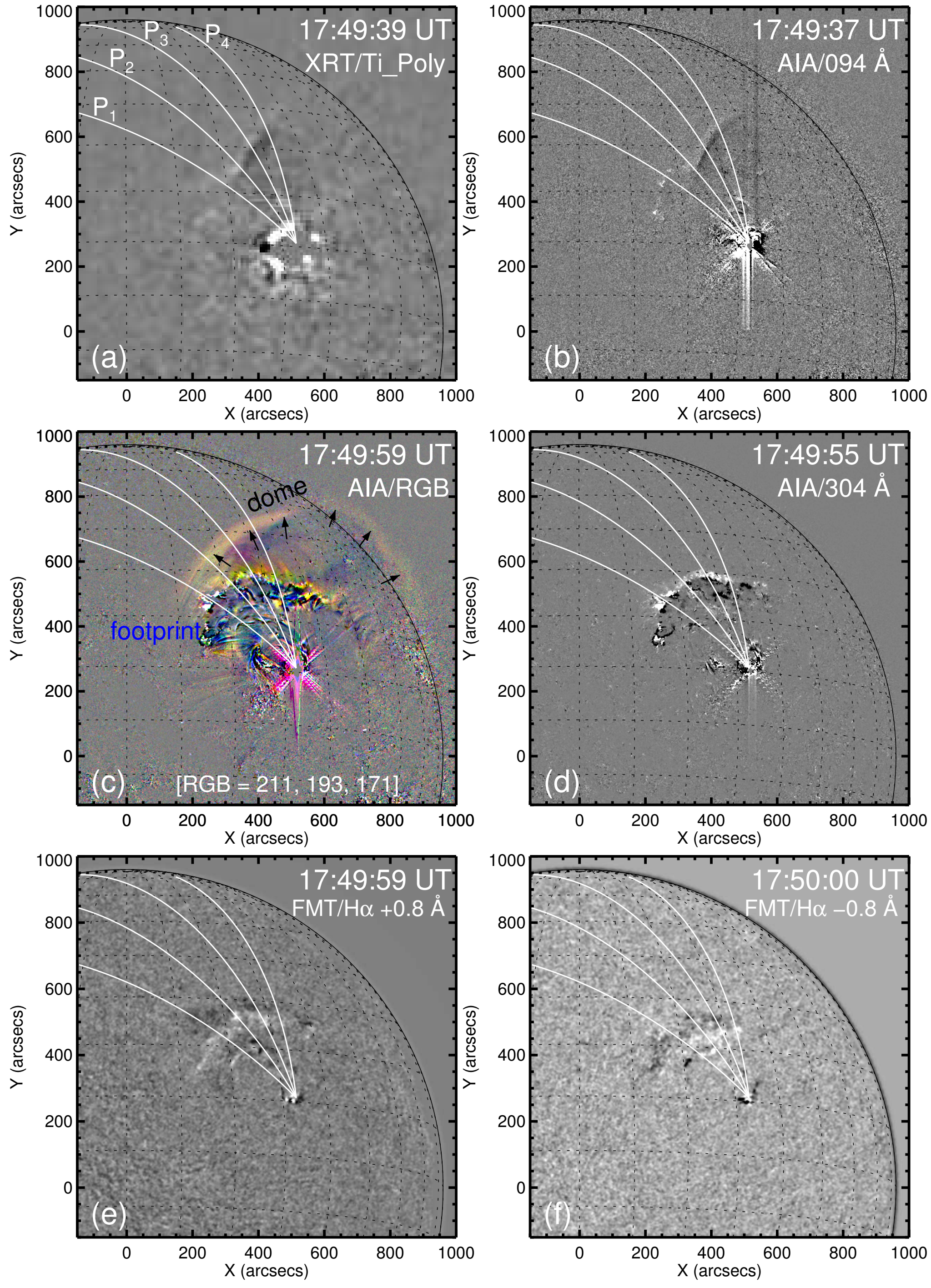

Figure 3.2: Coronal counterpart and Moreton wave associated with the X-class flare on 2014 March 29. The maps show different heights of the solar atmosphere, including the hotter component (∼6 MK) of the corona in X-ray and 94 Å (panels a, b), the intermediate component (1–2 MK) as a composition of AIA 211 Å (red), 193 Å (green) and 171 Å (blue) (panel c), the transition region ($\sim 5 \times 10^4$ K) at 304 Å (panel d), and the chromosphere ($\sim 10^4$ K) at Hα ± 0.8 Å (panels e, f). The maps illustrate the response of the solar atmosphere to the global disturbance triggered by the large-scale wave propagation. In panel (c) the arrows highlight the dome-like expansion of the coronal wave propagating ahead of the disturbed surface (footprint).

3.3.2 Kinematics

We performed Hα -0.8 and $+0.8$ Å running-difference intensity maps in order to enhance the wave contrast. Then, we extracted the intensity variation along the slits P_1–P_4 shown in Figure 3.2 (panels e, f). The results are presented in Figure 3.3 as time-distance diagrams, in which the wave signature at Hα $+0.8$ Å (upper panels) appears first as dark then as bright narrow stripes, while at Hα -0.8 Å (lower panels) as bright and dark lanes; both display identical evolution and similar tendency in the propagation speed. In the time-distance diagram P_2, we can also identify signatures of the wave front interacting with quiescent filaments that are located in the propagation direction of the Moreton wave.

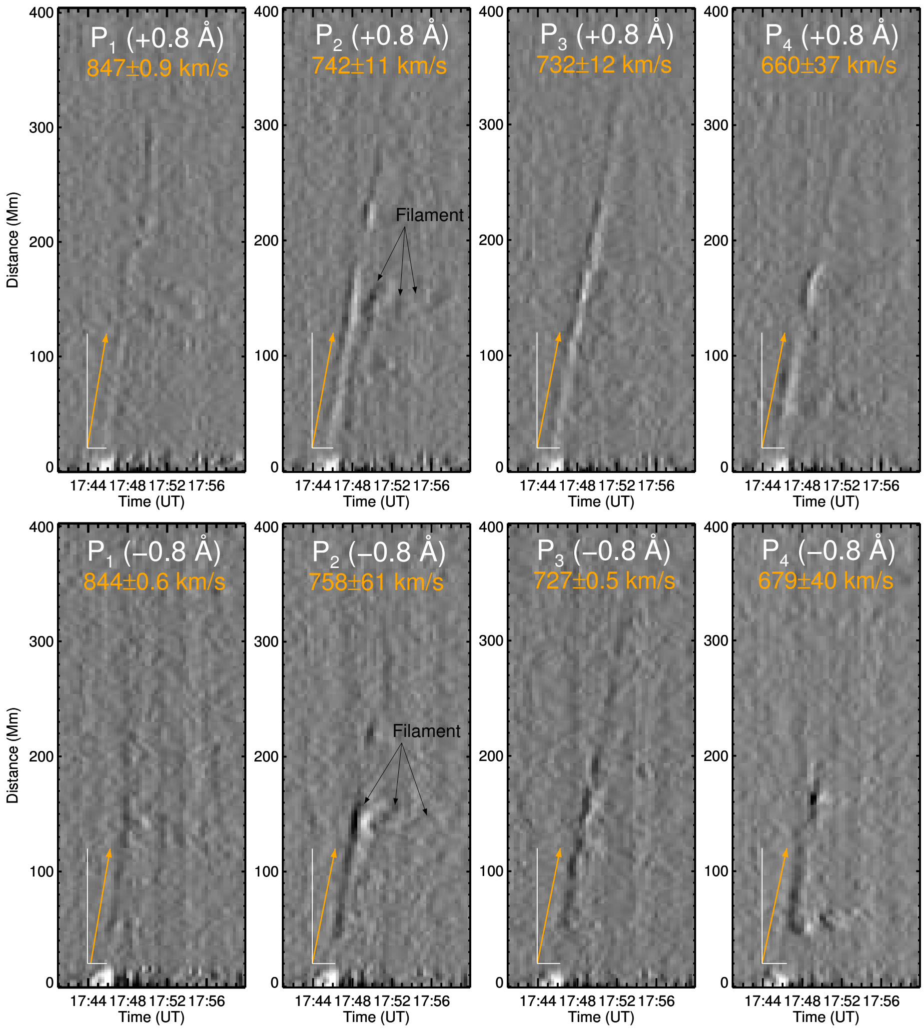

Figure 3.3: Time-distance diagrams of the Moreton wave obtained from running-difference images along trajectories P_1–P_4 (see panels e, f in Figure 3.2). The distance is expressed in megameters (Mm) starting from the flare site. The upper panels show results at Hα $+0.8$ Å and the lower panels at Hα -0.8 Å, wherein the orange arrows in each panel outline the earlier propagation speed of the Moreton wave. On the other hand, the black arrows in panels P_2 point out signatures of a filament activation due to the interaction with the Moreton wave.

In order to compare the nature of the Moreton wave with its associated coronal wave, time-distance diagrams from EUV and X-ray observations are also performed, whose results, obtained through slit P_3 (see Figure 3.2) are shown in Figure 3.4. The following characteristics can be drawn from the multiwavelength time-distance diagrams:

1. Taking the starting time of the GOES flux enhancement as reference, the corona, transition region, and the chromosphere reacted almost simultaneously to the extremely large propagating disturbance in the solar atmosphere, even though we note some delay in the response of more dense layers, i.e., the transition region and the chromosphere.

2. A similarity of the wave signature in terms of velocity and development is observed in Hα and He II (304 Å) lines, although in the latter the signature appears brighter and sharper (see also panel d in Figure 3.2). The enhanced emission in He II suggests that the transition region is evidently more affected than the chromosphere by the pressure jump as a consequence of the coronal wave passage.

3. Several characteristics at 211 Å are identified: a main or fast-component traveling at $\sim$969 km s^{-1} and a slow-component moving behind it with a speed of about 387 km s^{-1}. Here it is worth adding some comments on the observed features. The rapid expansion and the large propagation speed are inherent characteristics of a fast-mode magnetosonic wave. In contrast, the slower component possibly results from the deformation and restructuring of the ambient corona after the shock passage.

4. In the AIA hotter channel (94 Å) and X-ray Ti-poly the wave progression behaves identically, although the intensity variation due to the disturbance lasts for only about 6 minutes. The observed short period in these hotter channels can be ascribed to the temperature response of the instruments because they are sensitive to hotter coronal emission well above 6 MK. Therefore, it is more likely that the 94 Å and Ti-poly filters mainly detected the hottest part of the coronal wave that was possibly present during the early stage of the wave propagation.

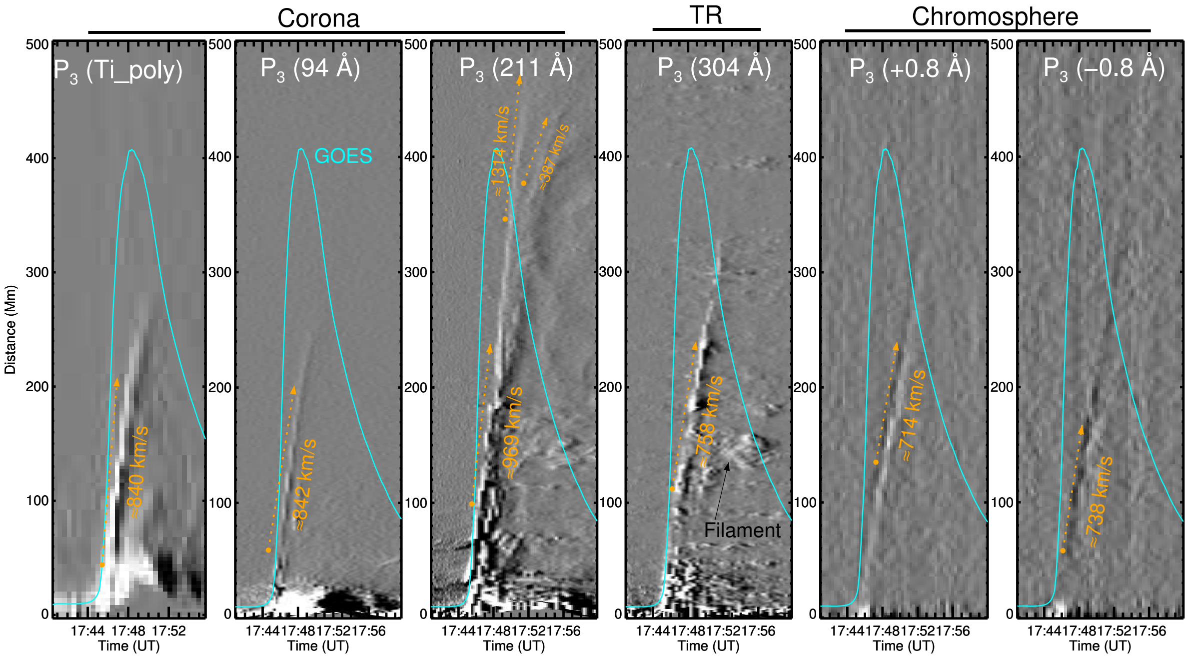

Figure 3.4: Time-distance diagrams of the disturbance in the corona, transition region (TR), and the chromosphere caused by the coronal wave on 2014 March 29. The intensity variation is calculated from running-difference images along trajectory P_3 shown in Figure 3.2. From left to right: X-ray Ti-poly filter ($\log T \sim 6.7$, with short time-range), EUV at 94 ($\log T \sim 6.8$), 211 ($\log T \sim 6.3$), and 304 Å ($\log T \sim 4.7$), and the wing of Hα at +0.8, −0.8 Å ($\log T \sim 4.0$), respectively. The cyan curves are the *GOES* X-ray emission at the 1–8 Å channel. The time-distance diagrams reveal that the corona, transition region, and the chromosphere reacted almost simultaneously to the global-scale wave propagation (see the text).

On the other hand, we also estimated the propagating distances of the Moreton wave by tracking the leading edge of the wave front in successive images. The measurements were made along four great-circle paths (P_1–P_4), the same trajectories for the time-distance diagrams, and assuming the flare site as the wave origin. The mean propagation velocity of the Moreton wave is calculated by applying the linear fitting to the time-distance plots. The results for Hα −0.8 and +0.8 Å are presented in Figure 3.5 (top panels), along with the results of the wave progression derived from He II line (304 Å). The plots show that the Moreton wave moves faster in the P_1 direction, both at Hα −0.8 and +0.8 Å with a mean velocity of 859 and 850 km s^{-1}, respectively. It is observed that there is a tendency in the speed of the Moreton wave to slow down as the path changes from trajectory P_1 to P_4. The derived mean velocities along paths P_2, P_3, and P_4 vary from 773 to 663 km s^{-1} at Hα −0.8 Å, and from 778 to 640 km s^{-1} at Hα +0.8 Å, respectively. The characteristics of the wave evolution at 304 Å are somewhat identical to that in Hα. Such identical features are clearly recognized by looking at the wave-front speeds along paths P_1–P_4, which are comparable to the derived speeds from

Hα observations, which also show a tendency of reduction in the propagation speed as the wave moves away from trajectory P_1 towards the northwest. The similarities of the wave progression in He II and Hα lines, and also in morphology as described in Section 3.3.1, is a clear indication that the plasma in the transition region and the chromosphere reacted in a similar manner to the action of the large-amplitude disturbance in the corona.

A similar analysis is conducted using AIA coronal lines at 211 and 94 Å, as well as hotter coronal emission captured by the XRT Ti-poly filter. Figure 3.5 (bottom panels) shows the time-distance plots derived from 211 Å, 94 Å, and Ti-poly observations, measured along paths P_1–P_4. They are same as for Hα and He II lines. It is shown that the wave in the corona develops in a different manner in terms of speed and propagation direction. For example, at 211 Å the estimated values of the mean velocity extends from 795 to 1369 km s^{-1}, which increases as the wave travels in the northwest direction (paths P_3, P_4). The same tendency is shown in the wave evolution at 94 Å and in the Ti-poly filter, having a mean velocity from 612 to 914 km s^{-1}, and 631 to 949 km s^{-1}, respectively, although only the earlier stage of the wave-front progression is identified in these hotter channels. Here it is worthwhile to point-out the following: because of the complex 3D dome-like expansion of the coronal wave and the projection effect, the results presented in the bottom panels of Figure 3.5 do represent the kinematics of the wave evolution at high altitudes rather than at the coronal base or the solar surface. In Table 3.1 we present a summary of the propagation speeds of the Moreton wave and the associated coronal wave calculated along the four paths, also including the mean value for each wavelength domain.

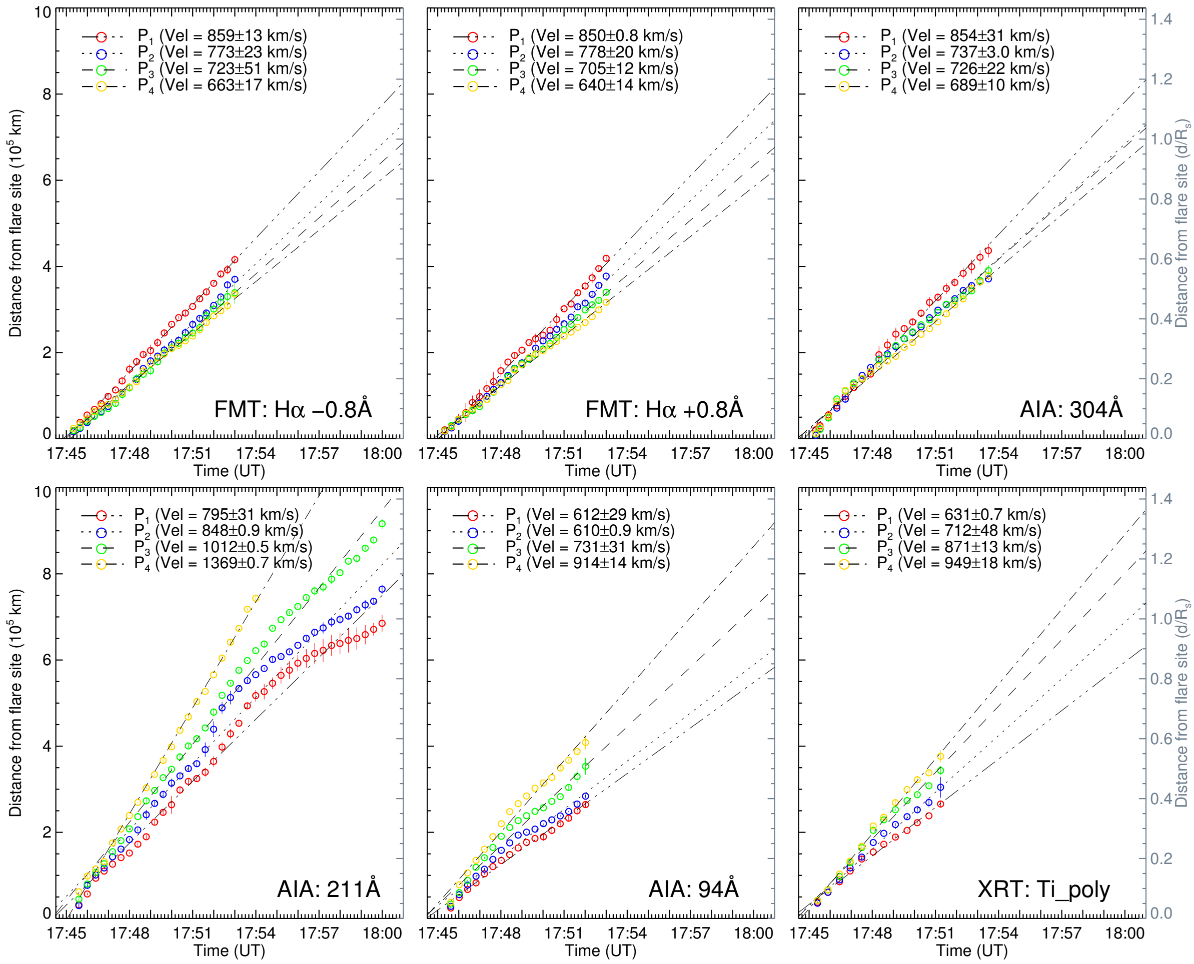

Figure 3.5: Time-distance plots of the Moreton wave and its associated coronal wave, measured from the flare site along paths P_1–P_4 shown in Figure 3.2. The top panels show Hα −0.8 Å (blue wing), Hα +0.8 Å (red wing) and He II (304 Å), while the bottom panels show AIA 211 and 94 Å, and the XRT Ti-poly filter. The corresponding mean velocity of the wave front derived from linear fitting is also shown. The uncertainty is estimated from the standard deviation. The right vertical axis in each panel, highlighted with gray, are in units of solar radii ($1R_s \approx 695,800$ km).

Table 3.1: Propagation speeds of the Moreton wave and its Associated Coronal Wave on 2014 March 29

Path	Hα -0.8 Å	Hα +0.8 Å	304 Å	211 Å	94 Å	XRT/Ti-poly
P_1	859 ± 13	850 ± 0.8	854 ± 30	795 ± 31	612 ± 29	631 ± 0.7
P_2	773 ± 23	778 ± 20	737 ± 3.0	848 ± 0.9	610 ± 0.9	712 ± 48
P_3	723 ± 51	705 ± 12	726 ± 22	1012 ± 0.5	731 ± 31	871 ± 13
P_4	663 ± 17	640 ± 14	689 ± 10	1369 ± 0.7	914 ± 14	949 ± 18
Mean	754.50	743.25	751.50	1006.00	716.75	790.75

(in km s^{-1})

3.4 Doppler Characteristics of the Moreton Wave

The Moreton wave is interpreted as a down-up swing disturbance in the chromosphere, as a result of the plasma being pushed downward by the globally expanding fast-mode wave or shock in the corona. This characteristic is regarded as compression followed by a relaxation process of the chromospheric material and induces the Doppler shift of Hα line and the brightness change in off-band images. In this section we investigate the Doppler characteristics of the Moreton wave.

3.4.1 Hα Intensity Profiles

As a general picture, the signature of the Moreton wave in the Hα line appears as a dark front in absorption in the red wing and as bright front in the blue wing, followed by a wider reversed disturbance in brightening and darkening in the red and blue wing, respectively. Because the FMT provides Hα wing observations at two wavelength that lie at equal distance from the line center, the absorption and brightening patterns of the wave front can be characterized by means of Doppler shift of the intensity profiles. To do so, we first normalized the Hα +0.8 (I_{red}) and −0.8 Å (I_{blue}) intensity maps to the spatially averaged quiet-Sun level measured at disk center. Next, considering the flare site as the wave origin and the four individual trajectories (P_1–P_4), same as for the kinematics analysis described in Section 3.3, intensity profiles as a function of distance x and time t are computed in red $I_r(x,t)$ and blue $I_b(x,t)$ wings by averaging the pixels intensities over consecutive areas of ∼44 arcsecs^2 (1×11 pixels) along each trajectory. Because the interest here is to determine the relative change of the intensity with respect to the unperturbed background, pre-event intensity profiles $I_r(x,t_0)$, $I_b(x,t_0)$ at 17:42:39 UT are obtained at the same positions of each corresponding trajectory, and are subtracted from the intensity profiles; that is, $\Delta I_{r,b} = I_{r,b}(x,t) - I_{r,b}(x,t_0)$.

In Figure 3.6 we present the obtained intensity profiles at Hα +0.8 and −0.8 Å, computed along the four paths (P_1–P_4) for the time steps 17:45:59 and 17:47:20 UT. The profiles reveal perturbations as depression and enhanced patterns caused by the arrival of the coronal wave to the chromosphere. This manifestation which is observed simultaneously as a strong depression in absorption in the red wing and as a moderated enhancement in the blue wing, corresponds to the downward motion of the chromospheric material caused by the collision between the coronal wave moving downward with the uppermost chromospheric layer. The characteristics observed in the profiles of the Hα wing suggests that the Hα spectral line is predominantly shifted redward in the initial response. In Figure 3.6 it is also interesting to note that right after the downward motion, the disturbed chromospheric layer exhibits a reversed pattern, i.e., brightening in the red wing and darkening in the blue wing (panels at 17:47:20 UT). This is because a restoration process takes place in the chromosphere after the plasma was forced to move downward, resulting in this down-up swing disturbance.

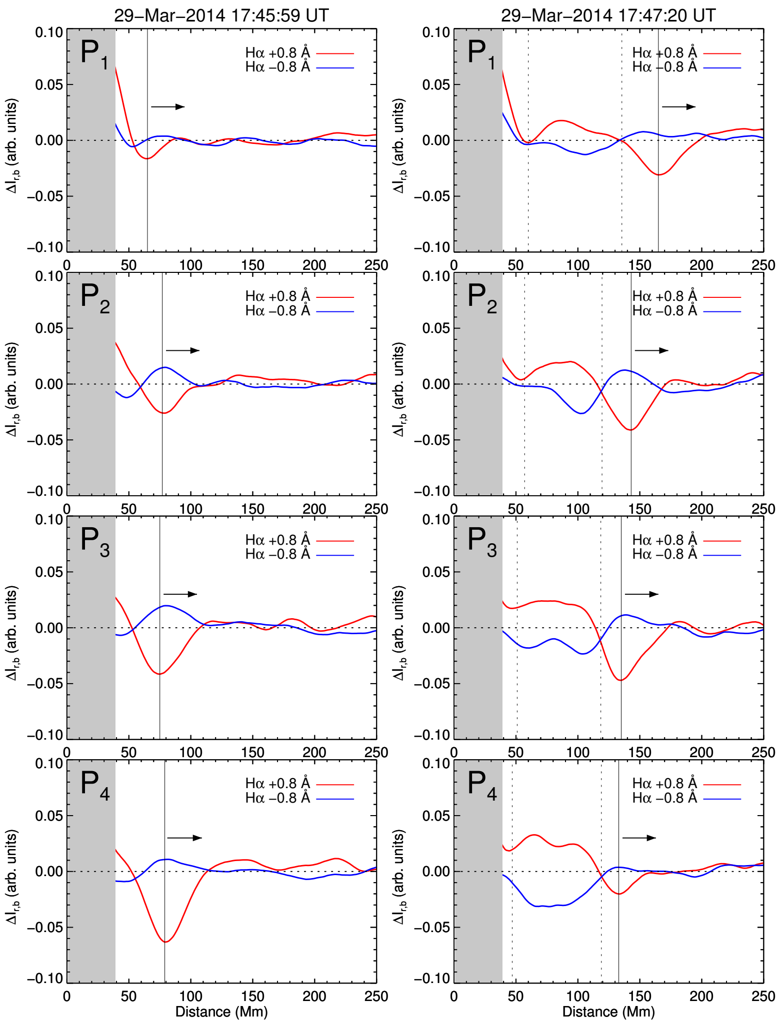

Figure 3.6: Hα intensity profiles relative to the quiet-conditions at +0.8 Å (red wing) and −0.8 Å (blue wing), computed along trajectories P_1–P_4 at 17:45:59 and 17:47:20 UT, respectively. The gray area in each panel covers the contaminated signal by the scattered light of the flare. The profiles show perturbations as depression and enhanced patterns caused by the arrival of the coronal wave to the chromosphere (vertical solid lines). The profiles at +0.8 Å exhibit a strong dip (redward), while at the same time the profiles at −0.8 Å is slightly enhanced (blueward). This intensity changes is an indication that the Hα spectral line is predominantly shifted redward. The intensity profiles also show subsequent disturbances to the wave passage (delimited by vertical dashed lines at 17:47:20 UT) showing a reversed pattern, i.e., enhancement in the red wing and reduction of the intensity in the blue wing. These delayed disturbances are related to the relaxation or recomposition state of the chromosphere.

3.4.2 Velocity Amplitude

We further examine the strength of the disturbance in the chromosphere by computing the velocity amplitude of the chromospheric plasma. The combination of the normalized intensity maps performed previously allows us to produce Doppler signals. The following expression is applied to obtain the Doppler signal

$$DS = \frac{I_r(x,t) - I_b(x,t)}{I_r(x,t) + I_b(x,t)}, \tag{3.1}$$

where I_r and I_b are the Hα intensity recorded at +0.8 (red wing) and −0.8 Å (blue wing) from the line center, respectively. Note that a positive Doppler signal corresponds to a blueshift (upward motion), and it is opposite to the convention.

To quantify the Doppler signal obtained along paths P_1–P_4, we correlate them with a synthetic Doppler signal resulting from the convolution of the Hα solar spectrum with the FMT filter-transmission profiles centered at 6562.0 and 6563.6 Å. Because the synthetic Doppler signal provides insights into the amount of wavelength shift $\Delta\lambda$ with respect to the core wavelength λ_0, we can directly determine the Doppler velocity $v = (\Delta\lambda/\lambda_0)c$, where c is the speed of light. Representative profiles of the FMT filter-transmission together with the profile of the atlas solar spectrum are shown in Figure 3.7. The relation between the line-of-sight velocity and the Doppler signal is also shown in the lower panel of Figure 3.7.

In Figure 3.8 we show the estimated Doppler velocity of the Moreton wave expressed as perturbation profiles, obtained along four trajectories (P_1–P_4) for six different time steps. The perturbation profiles show a clear evolution of the wave-front progression, revealing downward motion and a subsequent relaxation process as upward motion of the local chromospheric plasma. This represents the velocity amplitude of the moving mass at the front of the Moreton wave. Carrying out an inspection to the perturbation profiles, we see a successive depletion (downward velocity) in the P_2, P_3, and P_4 directions for the time interval between 17:45 and 17:50 UT, meaning that the chromospheric material is being pushed downward as the wave front hits and expands through the chromosphere. The maximum depletion caused by the wave front is observed along trajectory P_4 at 14:45:59 UT, it occurs relatively close to the source region (i.e, flare site) at a distance of ∼80 Mm, reaching a highest value of about −4 km s^{-1}. At the same time and distance the perturbation profiles along P_2 and P_3 show that the plasma moves downward with a velocity of −2.4 and −3.5 km s^{-1}, respectively, whereas at this time the effect of the wave front along P_1 is less pronounced. Another strongest signature of plasma compression is noted at 17:47:20 UT in P_2 and P_3 directions located ∼140 Mm from the flare site with velocities of −2.9 and −3.3 km s^{-1}, respectively, and at 17:48:20 and 17:48:59 UT along trajectories P_4 and P_3 with velocities of about −2.5 and −2.7 km s^{-1}, respectively. It is noted that the amplitude of the velocity profiles decreases with increasing distance. For example, this effect is much more evident in the P_2, P_3 and P_4 directions, suggesting that the strength of the large-amplitude coronal disturbance weakens with time.

The perturbation profiles in Figure 3.8 also exhibit strong steepness (upward motion) along paths P_1, P_2, and P_3, particularly at 17:48:20 and at 17:48:59 UT. These features are not due to the response of the local chromospheric plasma to the wave-front passage, but are due to the interaction with quiescent filaments that lie in the propagation direction of the Moreton wave.

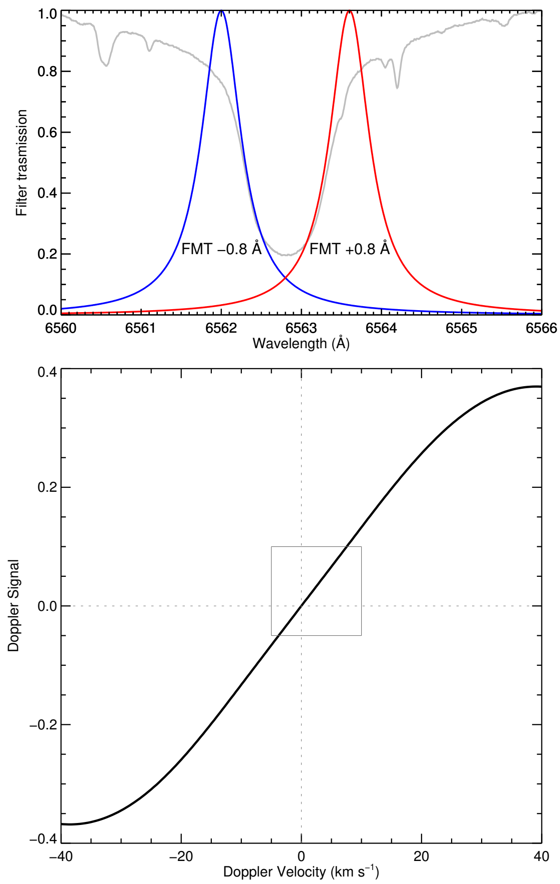

Figure 3.7: Upper: FMT filter-transmission profiles centered at 6562.0 Å (blue) and 6563.6 Å (red), respectively, both with a nominal FWHM of 0.6 Å. The gray background profile is the atlas solar spectrum of the Hα line normalized to the continuum. Lower: synthetic Doppler signal as a result of convolving the FMT filter-transmission profiles with the solar spectrum. The inset box in the plot outlines the range of the Doppler signal obtained from our observation.

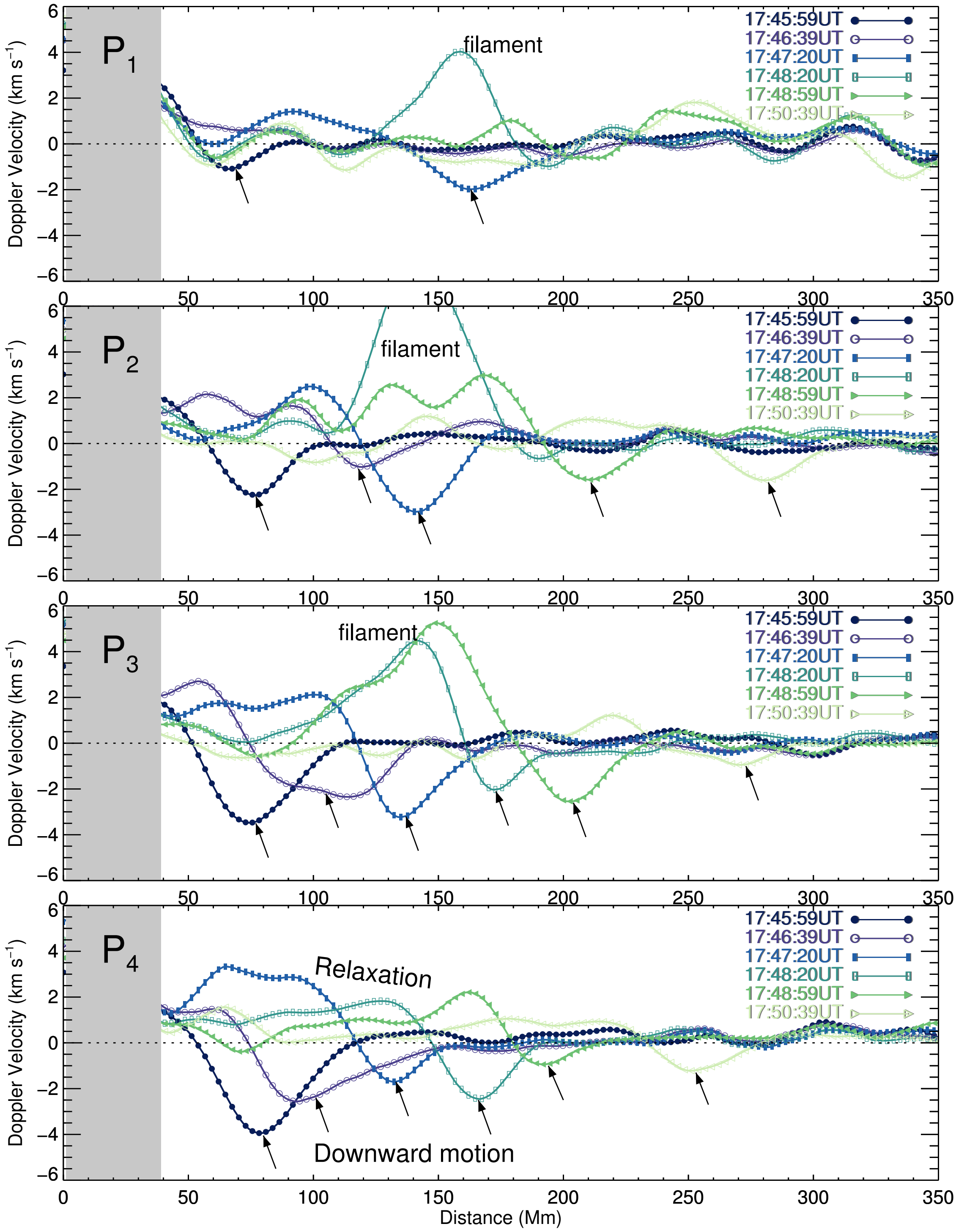

Figure 3.8: Doppler velocity of the Moreton wave on 2014 March 29 for six time steps along trajectories P_1–P_4. The velocity was estimated by correlating the obtained perturbation profiles with a synthetic Doppler signal (see the text). The profiles show the velocity amplitude of the moving mass at the front of the Moreton wave, wherein the arrows point out the downward motion of the chromospheric plasma produced by the global disturbance in the corona. A subsequent relaxation process of the chromospheric layer is also observed. At about 17:48:20 and 17:48:59 UT the profiles also exhibit strong steepness (upward motion) along paths P_1, P_2, and P_3. These features are due to the wave interaction with quiescent filaments standing in the propagation direction of the Moreton wave.

3.4.3 Velocity Map

The intensity maps described in Section 3.4.1 are also used to characterize the mass motion of the local chromospheric material caused by the progression of the Moreton wave. Applying Equation (3.1), we produced Doppler signal maps, then base-difference maps were obtained by subtracting a pre-event map taken at 17:42:39 UT. The subtraction essentially permits us to preserve the wave-front signatures as residuals, as well as to enhance the wave contrast. Following the procedure for determining the velocity amplitude in Section 3.4.2, we calculated the line-of-sight velocity at every pixel of the map by cross-correlating the base-difference maps with the synthetic Doppler signal. The results are presented in Figure 3.9 as time-series Doppler maps, wherein it is revealed that the leading edge of the traveling wave front appears as downward motion of the chromospheric structure, followed closely by a much wider disturbance seen as the upward motion due to the restoration of the chromospheric layer. It can be noted that the wave fronts develop semicircular shapes, showing a preferential propagation direction northeast from its origin, possibly moving toward the regions of low Alfvén speed distribution (see discussion in Section 3.6.1). As in the perturbation profiles (Figure 3.8), high downward velocity is observed in the initial stage of the wave propagation. It is also observed that the Moreton wave becomes progressively more diffuse and irregular; the wave signature is no longer recognized after 17:53:20 UT (see the animation of Figure 3.9 in the online version of the published paper).

3.5 Coronal Shock Diagnostic

In this section we focus on the characteristics of the coronal shock wave and its interaction with the underlying chromosphere. We explore the scenario in which the Moreton wave is created under the action of the MHD fast-mode wave propagation in the corona.

3.5.1 Corona–chromosphere Interaction

In Figure 3.2(c) it is noted that the footprint of the dome-like expanding coronal wave morphologically and spatially corresponds to the wave front observed in the He II and Hα lines (Figure 3.2c–f). The manifestation of the local plasma in these cooler lines is in response to the compression exerted by the downward-propagating disturbance in the corona, as discussed in previous sections.

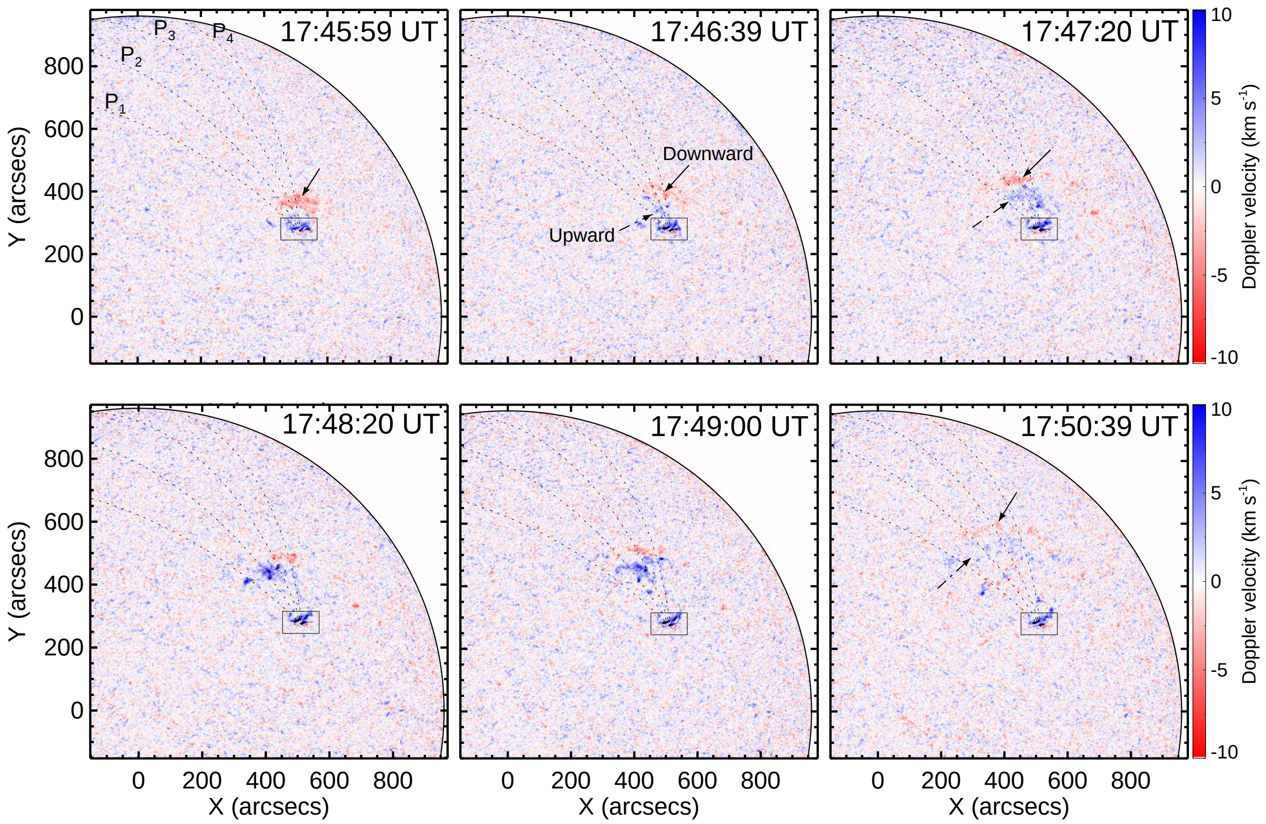

Figure 3.9: Doppler maps of the Moreton wave on 2014 March 29. The time period is the same as that shown in the perturbation profiles (Figure 3.8). The wave fronts highlighted in red and blue correspond to downward and upward motions of the chromospheric plasma (see the text). The leading edge of the Moreton wave observed in red may be related to plasma compression, while the trailing seen in blue is an indication of recovery or relaxation process of the chromosphere. The rectangles in each panel depict the flare site, and the dashed lines outlines the trajectories P_1–P_4 considered in our analysis.

The interaction of the corona and chromosphere can be treated as a discontinuity problem. In Figure 3.10(a) we present a schematic picture of a globally propagating shock in the corona intersecting the transition region and the chromosphere. The illustration also shows two instants of interaction (Figure 3.10b), namely the shock wave propagating in the corona just before the collision with the transition region ($t < t_1$), and the subsequent period ($t > t_1$). In this scheme the transition region acts as the interface layer between the corona and chromosphere, which in our analysis represents the contact discontinuity. Because the transition region is a thin layer, strong effects are expected because of the collision. At the time of shock arrival in the transition region, the downward motion of the plasma traveling behind the shock with a velocity v_i, which is the velocity amplitude of the incident wave, leads instantaneously to a downward motion of the local plasma, pushing the transition region down and setting the motion in the chromosphere with a velocity v_t. This latter represents the velocity amplitude of the transmitted wave from the corona to the chromosphere right after the collision, and can be interpreted as the velocity amplitude of the chromosphere observed in the Hα line during the passage of the Moreton wave. In addition, because of the sudden density jump between the corona and chromosphere, a reflected wave traveling in the corona in the opposite direction is also expected, and the velocity of the upward-moving plasma is denoted by v_r in our analysis (see Figure 3.10b).

In the 1D discontinuity problem and with the aid of the conservation laws of momentum flux and energy flux, the shock wave transmission from the corona into the chromosphere can be related as follows:

$$\rho_{co}(v_i - v_r)c_{co} = \rho_{ch} v_t c_{ch} \tag{3.2}$$

$$\rho_{co}(v_i^2 - v_r^2)c_{co} = \rho_{ch} v_t^2 c_{ch}. \tag{3.3}$$

In the above equations, v is the velocity amplitude of the wave, where the subscripts denote the incident i, reflected r, and transmitted t waves, as discussed above. The plasma density and the phase velocity of the MHD fast-mode wave in the corona co and chromosphere ch are denoted by ρ_{co}, ρ_{ch} and c_{co}, c_{ch}, respectively. Similar to Takahashi et al. (2015), we find from Equations (3.2) and (3.3) a direct relation between the velocity amplitude of incident and transmitted waves,

$$v_i = \left(\frac{1+\sqrt{a}}{2}\right) v_t, \tag{3.4}$$

here $a = \rho_{ch}/\rho_{co}$ is the density ratio of the chromosphere and corona. The velocity amplitude we derived from Hα observation (Figure 3.8) is a direct indicator of v_t.

The result of the velocity amplitude of the incident wave v_i calculated with Equation (3.4) is listed in Table 3.2. The calculation is made assuming the density in the chromosphere and the corona to be $\rho_{ch} \approx 10^{11}$ and $\rho_{co} \approx 10^9 \text{cm}^{-3}$, respectively, and also taking as v_t the highest downward velocity that is observed in the perturbation profiles of the Moreton wave.

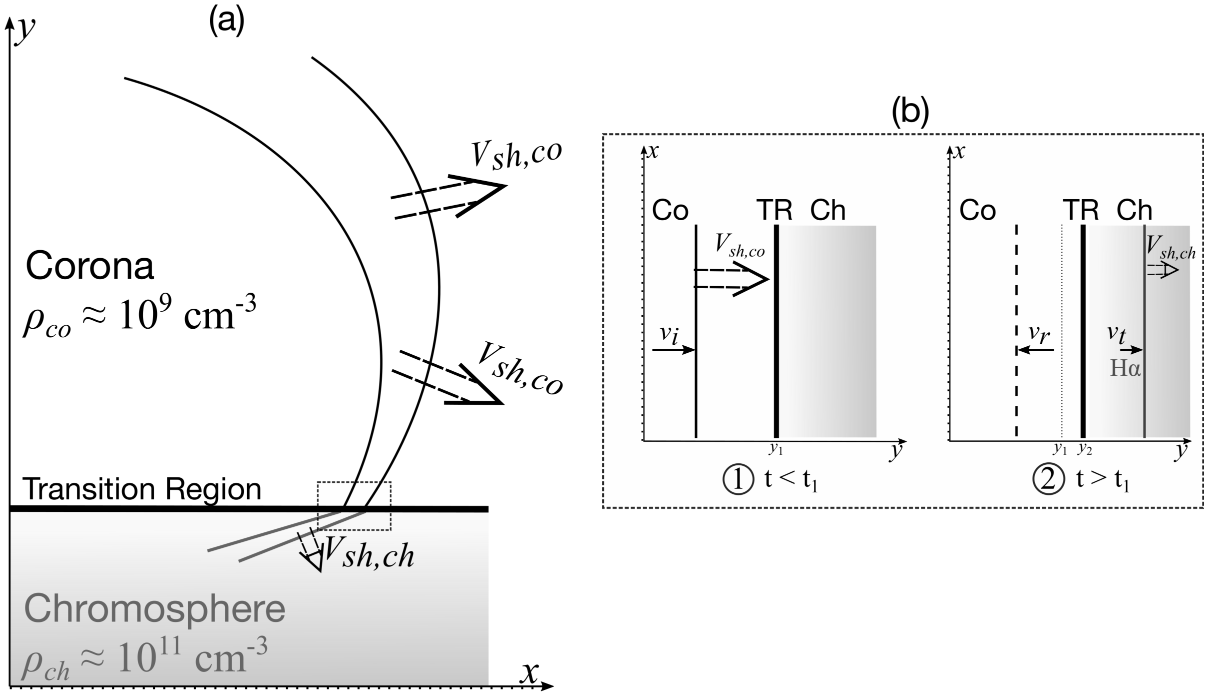

Figure 3.10: (a) Schematic picture of a globally propagating shock wave in the corona $V_{sh,co}$ that intersects the transition region and the chromosphere $V_{sh,ch}$. (b) Enlarged view of the interaction of corona and chromosphere (dotted rectangle in panel (a), note the change of axis orientation). The illustration shows two instants of interaction: (1) a shock wave propagating in the corona just before the collision with the transition region ($t < t_1$), and (2) the subsequent period ($t > t_1$). At the time when the shock wave reaches the transition region, the downward motion of the plasma traveling behind the shock with a velocity v_i (incident wave) leads to a downward shift in the transition region from y_1 to y_2, this occurs at $t > t_1$. As a consequence, the chromosphere is forced to move downward with a velocity v_t, this is the velocity amplitude of the transmitted wave from the corona to the chromosphere right after the collision and can be regarded as the velocity amplitude of the Moreton wave seen in the Hα line. Additionally, due to the density discontinuity at the corona–chromosphere boundary, a reflected wave v_r is also identified that travels in the opposite direction in the corona.

Table 3.2: Velocity Amplitude of Incident v_i and Transmitted v_t Waves along Trajectories P_1–P_4.

Time (UT)	P_1		P_2		P_3		P_4	
	v_i	v_t	v_i	v_t	v_i	v_t	v_i	v_t
17:45:39	6.05	1.1	6.05	1.1	13.7	2.5	15.9	2.9
17:45:59	6.60	1.2	13.2	2.4	19.2	3.5	22.0	4.0
17:46:20	6.05	1.1	8.25	1.5	11.0	2.0	15.9	2.9
17:46:39	–	–	6.05	1.1	13.2	2.4	13.7	2.5
17:46:59	–	–	8.80	1.6	18.1	3.3	11.0	2.0
17:47:20	11.0	2.0	15.9	2.9	18.1	3.3	10.4	1.9
17:47:39	8.80	1.6	11.0	2.0	20.35	3.7	8.25	1.5
17:47:59	7.69	1.4	9.90	1.8	19.8	3.6	13.2	2.4
17:48:20	5.50	1.0	–	–	12.6	2.3	13.7	2.5
17:48:39	–	–	5.50	1.0	8.25	1.5	11.0	2.0
17:49:00	–	–	–	–	14.8	2.7	5.50	1.0
17:49:20	7.69	1.4	9.90	1.8	11.0	2.0	4.40	0.8
17:49:39	–	–	–	–	13.2	2.4	3.30	0.6
17:50:00	11.0	2.0	3.30	0.6	12.6	2.3	3.30	0.6
17:50:20	–	–	–	–	10.4	1.9	7.15	1.3
17:50:39	–	–	8.80	1.6	5.50	1.0	6.60	1.2
17:50:59	–	–	8.25	1.5	3.85	0.7	6.05	1.1

(in units of km s^{-1})

3.5.2 Shock Strength in the Corona Based on the Moreton Wave Velocity Amplitude

The purpose of this Section is to show how our Hα results can further be used to characterize the strength of the incident shock in the corona. Using the Rankine-Hugoniot relations and taking advantage of the weak-shock approximation, which states that the discontinuity in every quantity is small (see Landau & Lifshitz, 1987), that is, the shock speed is slightly higher than the sound speed, we can relate the velocity amplitude of the shock in the corona to that of the velocity amplitude of the disturbance in the chromosphere, the latter being the Hα velocity amplitude of the Moreton wave. The following expression summarizes the above statements:

$$v_t = -\frac{4}{\gamma+1}(M_i^2-1)\frac{c_{ch}}{1+c_{ch}/c_{co}}, \tag{3.5}$$

where v_t is the velocity amplitude of the disturbance in the chromosphere, M_i is the Mach number of the incident shock in the corona, and c_{ch} and c_{co} are the propagation speed of the shock in the chromosphere and corona, respectively. The derivation of this equation is presented in Appendix A along with and illustration (Figure A.1). Equation (3.5) allows us to estimate the Mach number of the shock in the corona for a given value of the Hα velocity amplitude.

Let us discuss Equation (3.5) in more detail. Under the weak-shock approximation, the propagation speed of the shock in the corona is the sound speed. Under this condition, the situation in the chromosphere may also be the same. For example, for a typical temperature in the chromosphere $T \approx 10^4$ K, the sound speed is $c_s = \sqrt{(\gamma\ k\ T)/m_p} \approx 10$ km s^{-1}, where k is the Boltzmann constant, m_p is the proton mass, and γ is the adiabatic index of the gas. In weak-shock events, this sound speed would be comparable to the speed of the shock in the chromosphere, as we noted above. Furthermore, because the sound speed in the corona is about one order of magnitude higher than that in the chromosphere, or even more, the term c_{ch}/c_{co} in the equation can be neglected.

Taking into account the above considerations and making use of the derived velocity amplitude of the Moreton wave v_t along with the adiabatic index $\gamma = 5/3$, Equation (3.5) can be now evaluated. The results are shown in Table 3.3. We stress that the calculation presented here is in a 1D regime and a pure hydrodynamic approach, no magnetic field effect is considered. A future work will be devoted to this calculation and will include many more details.

Table 3.3: Mach Number of the Incident Shock in Corona Along Trajectories P_1–P_4, Based on the Moreton Wave Velocity Amplitude.

Time (UT)	P_1	P_2	P_3	P_4
17:45:39	1.04	1.04	1.08	1.09
17:45:59	1.04	1.08	1.11	1.12
17:46:20	1.04	1.05	1.06	1.09
17:46:39	–	1.04	1.08	1.08
17:46:59	–	1.05	1.10	1.06
17:47:20	1.06	1.10	1.11	1.06
17:47:39	1.05	1.07	1.11	1.05
17:47:59	1.05	1.06	1.11	1.08
17:48:20	1.03	–	1.07	1.08
17:48:39	–	1.03	1.05	1.06
17:49:00	–	–	1.08	1.03
17:49:20	1.04	1.06	1.06	1.03
17:49:39	–	–	1.08	1.02
17:50:00	1.06	1.02	1.07	1.02
17:50:20	–	–	1.06	1.04
17:50:39	–	1.05	1.03	1.04
17:50:59	–	1.05	1.02	1.03

3.5.3 Shock Characteristics in the Corona

According to the MHD shock theory, the jump relation that describes an oblique shock is defined as (Priest, 2000)

$$(v_1^2 - Xv_{A1}^2)^2\{Xc_{s1}^2 + \frac{1}{2}v_1^2\cos^2\theta(X(\gamma-1)-(\gamma+1))\} + \frac{1}{2}v_{A1}^2 v_1^2 \sin^2\theta\ X$$
$$\times\{(\gamma + X(2-\gamma))v_1^2 - Xv_{A1}^2((\gamma+1)-X(\gamma-1))\} = 0, \tag{3.6}$$

where $X \equiv \rho_2/\rho_1$ is the compression ratio or density jump at the front of the shock, θ is the angle between the upstream magnetic field and the shock normal, and c_s and v_A are the sound and Alfvén speeds, respectively. Taking for the adiabatic index $\gamma = 5/3$ and the sound speed $c_s^2 = (\gamma\beta/2)v_A^2$, Equation (3.6) can be rewritten in terms of the Alfvén Mach number M_A as follows (see Appendix B, also Vršnak et al., 2002a):

$$(M_{A1}^2 - X)^2\{5\beta X + 2M_{A1}^2\cos^2\theta(X-4)\} + M_{A1}^2\sin^2\theta\ X$$
$$\times\{M_{A1}^2(5+X) + 2X(X-4)\} = 0. \tag{3.7}$$

Equation (3.7) depends on the inclination θ, the compression ratio X, and also on the ratio of the plasma to the magnetic field pressure β. Under the assumption that the proton number density n of the coronal emitting plasma is constant along the line-of-sight, the compression ratio may roughly be estimated from the emission measure $EM \simeq n^2 l$, where l is the depth of the emitting plasma along the line-of-sight. Because the coronal mass density is $\rho \simeq nm_p$, m_p being the proton mass, it is reliable to express the following quantities as $EM_2/EM_1 = \rho_2^2/\rho_1^2$, here the subscripts 1 and 2 denote the emission measure and mass density ahead of and behind the shock front, respectively, and we assume that l is common between them. Therefore we can write

$$X \equiv \frac{\rho_2}{\rho_1} = \sqrt{\frac{EM_2}{EM_1}}. \tag{3.8}$$

The emission measure is estimated from AIA observations by applying DEM inversion method of Cheung et al. (2015). As a first step, we constructed DEM maps for a set of 21 temperature bins, spanning $\log T/\mathrm{K} = 5.7$–7.7. We note that DEM solutions for $\log T/\mathrm{K} < 6.1$ do not clearly show signatures of the wave front-progression, and although solutions for $\log T/\mathrm{K} > 6.4$ exhibit signs of the wave front, it is greatly influenced by the scattered light of the flare. Because our interest is to trace the wave propagation, we restrict the temperature grid to $6.1 \leq \log T/\mathrm{K} \leq 6.4$, at which the coronal wave front in DEM maps is best observed (see Figure 3.11). Next, considering four trajectories from the flare site (P_1–P_4), the same as for the Moreton wave (see Section 3.4), we proceed to obtain perturbation profiles by spatially averaging the DEM solutions along each trajectory shown in Figure 3.11. Last, the computed DEM perturbation profiles in the temperature range $6.1 \leq \log T/\mathrm{K} \leq 6.4$ were integrated to obtain the total emission measure EM, which enabled us to derive the compression ratio X by applying Equation (3.8). It should be noted that for the calculation of the compression ratio we have considered as EM_1 in Equation (3.8) a pre-shocked emission measure at 17:42:37 UT. Figure 3.12 shows the obtained compression ratio distribution along four trajectories, corresponding to the nearest time interval of the Moreton wave velocity amplitude shown in Figure 3.8.

On the other hand, the pre-shocked plasma temperature in the corona was constrained by applying the XRT filter ratio method (Narukage et al., 2011) on two pairs of filters (Al-poly/Be-thin), which results in $T_1 \simeq 2.5$ MK. With this value, the sound speed in the corona $c_s = \sqrt{(\gamma\ k\ T_1)/m_p}$ is 185 km s^{-1}. Moreover, based on XRT Ti-poly observations, the speed

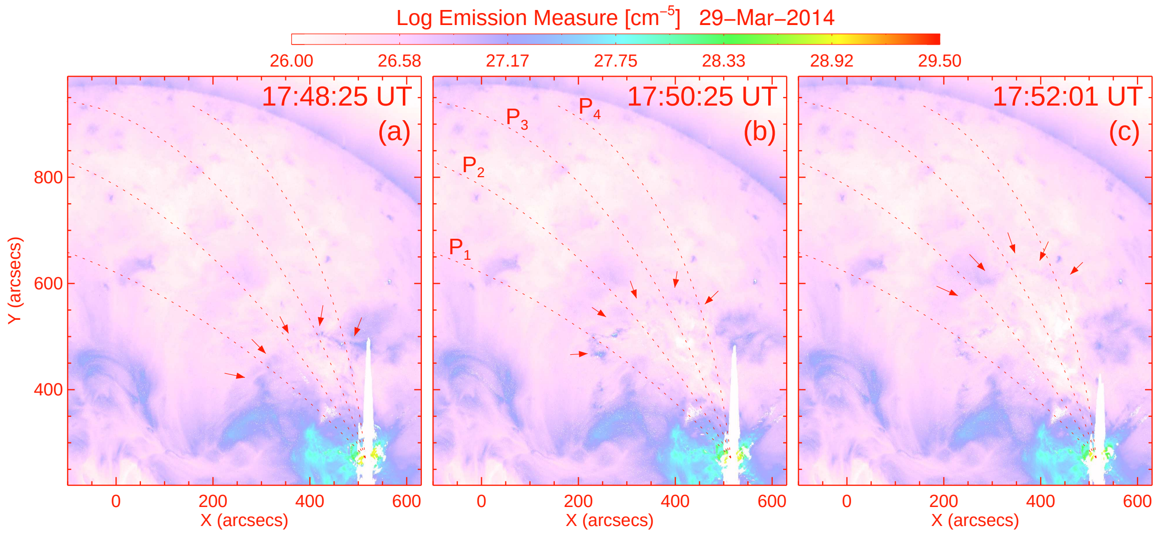

Figure 3.11: Differential emission measure maps showing three instants of the coronal wave on 2014 March 29. We used the method of Cheung et al. (2015), which enabled us to obtain DEM maps for a set of temperature bins. The panels show DEM solutions for a temperature range of $6.1 \leq \log T/\mathrm{K} \leq 6.4$ (see the text), wherein the manifestation of wave propagation (arrows) clearly can be distinguished as traveling northeast. Based on these results, we calculate DEM perturbation profiles along trajectories P_1 to P_4 (dashed lines), which were used to derive the compression ratio X presented in Figure 3.12.

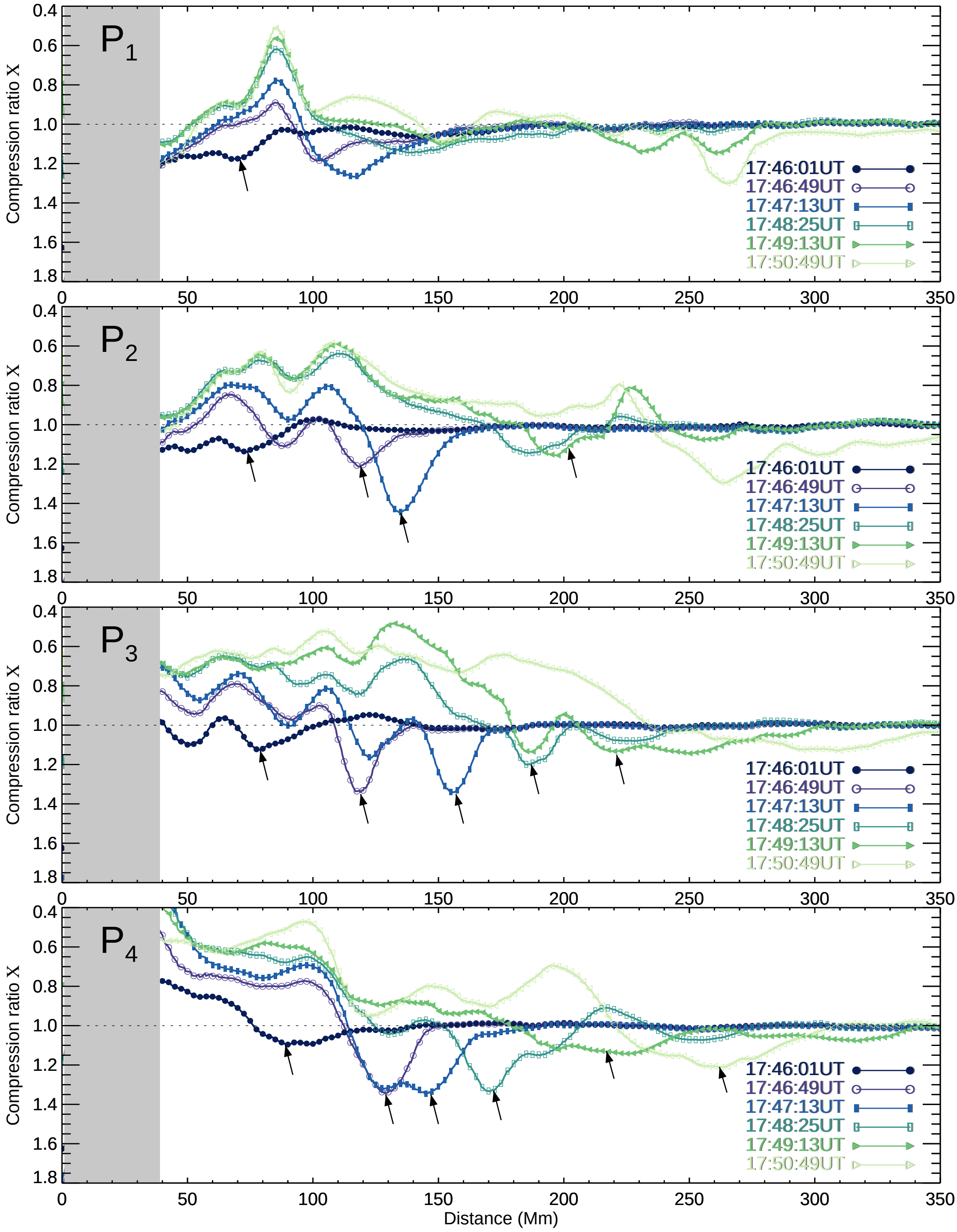

Figure 3.12: Compression ratio X estimated from DEM maps along trajectories P_1–P_4 shown in Figure 3.11. We obtained the total emission measure by integrating the DEM perturbation profiles over a temperature range, then Equation (3.8) was applied to estimate the compression ratio (see the text). The pre-shocked emission measure EM_1 in Equation (3.8) is that resulting from DEM map at 17:42:37 UT. The compression ratio profiles along each trajectory correspond to the nearest time interval of the Moreton wave velocity amplitude presented in Figure 3.8. Note that the vertical axes are inverted for better comparison of the observed characteristics (arrows) with those in the Moreton wave perturbation profiles.

of the fast-mode wave in the corona can be assumed to be $c_f \simeq 790$ km s^{-1}, corresponding to the mean value of the speeds along trajectories P$_1$–P$_4$ (see Table 3.1). In the case of perpendicular wave propagation ($\theta = 90\,\text{deg}$), the Alfvén speed in the corona is defined as $v_A = \sqrt{c_f^2 - c_s^2}$, which yields $v_A = 768$ km s^{-1}. Finally, with the results we obtained for the sound speed and the Alfvén speed, the plasma-to-magnetic pressure ratio in the corona is estimated as $\beta = 0.06$, allowing us now to evaluate Equation (3.7) and find solutions for the Alfvén Mach number M_A for given values of the inclination θ. Furthermore, when we assume the velocity of the shock in the corona to be v_{sh}, it is straightforward to relate the Alfvén Mach number $M_A = v_{sh}/v_A$ along with the sound speed c_s to the fast-mode (or fast magnetosonic) Mach number $M_f = v_{sh}/c_f$. Again, for a perpendicular case, the following relation holds:

$$M_f = \frac{M_A}{\sqrt{1 + \gamma\beta/2}}. \tag{3.9}$$

In Figure 3.13 we present solutions of Equation (3.7) for the Alfvén Mach number. The calculations were made by considering two scenarios of shock propagation: horizontal ($\theta = 0\,\text{deg}$) and perpendicular ($\theta = 90\,\text{deg}$) (see Appendix B), and taking the highest possible values of the compression ratio profiles in the four trajectories; those that are closely connected to the positions of the most prominent downward motion of the Moreton wave at each instance. Figure 3.13 also compares the fast-mode Mach number estimated with Equation (3.9). This based on the Alfvén Mach number derived for the perpendicular case.

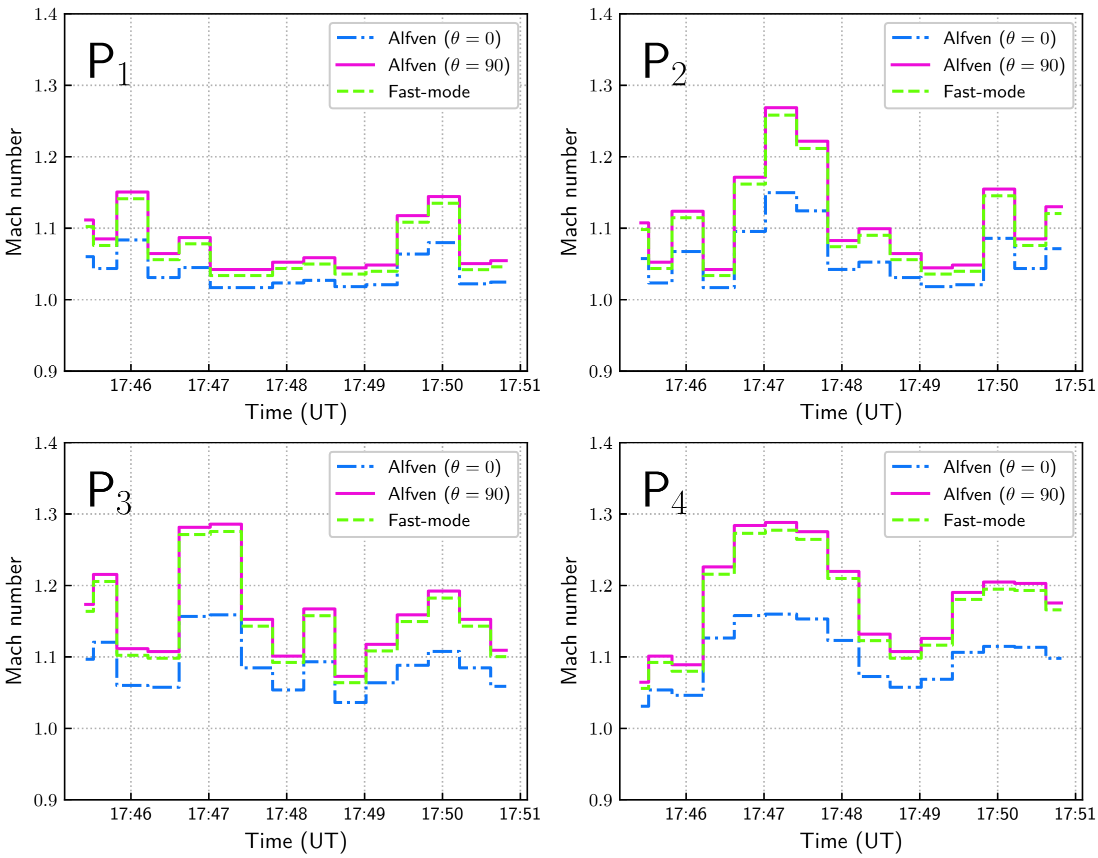

Figure 3.13: Alfvén and fast-mode Mach numbers of the coronal wave on 2014 March 29 along trajectories P_1–P_4. The Alfvén Mach number is based on the solution of Equation (3.7) using the compression ratio derived from the differential emission measure. The profiles in blue and magenta show solutions for horizontal ($\theta = 0$ deg) and perpendicular ($\theta = 90$ deg) shock propagation cases, respectively. For the calculation we take the highest values of the compression ratio profiles in each trajectory, those that are closely connected to the positions of large downward motion of the Moreton wave. On the other hand, the fast-mode Mach numbers (green profiles) are solutions of Equation (3.9) taking the results of the Alfvén Mach number for the perpendicular case.

3.6 Discussion

3.6.1 Morphology and Propagation Speed of the Moreton Wave

The Moreton wave on 2014 March 29 has brought interesting insights into our picture of chromospheric disturbances associated with flares. Thanks to the multiwavelength coverage, it was possible to reveal details of this wavelike phenomenon happening in the chromosphere in conjunction with its coronal counterpart. It is not surprising that the derived propagation speed of the Moreton wave is comparable to that of the propagation speed of the coronal wave obtained from AIA and XRT observations, and the morphology of the wave front seen in the chromosphere also shows a good correspondence in space and time with the footprints of the expanding dome-like structure in the corona (Figure 3.2). This scenario further confirms that Moreton waves are the chromospheric manifestation of an MHD fast-mode shock wave traveling through the corona, as theoretically anticipated by Uchida (1968). Furthermore, the multiwavelength time-distance diagrams presented in Figure 3.4 show that each region of the solar atmosphere reacts and evolves quasi-simultaneously, implying that a globally propagating shock in the corona is the triggering source of the observed disturbances.

We found that the mean velocity of the Moreton wave varies depending on the wave propagation direction (Figure 3.5, top panels). Similar behavior is also observed in the coronal wave propagation speed (Figure 3.5, bottom panels), although in the latter case the situation is much more complex due to the 3D expansion and the projection effect. The difference of the propagation velocity along the analyzed trajectories can be attributed to the plasma condition and the inhomogeneous topology through which the wave propagates. In the solar atmosphere both the density and the magnetic field change considerably in the vertical direction, i.e., the density starts to decrease rapidly in the low corona, while the magnetic field drops much faster in the outer corona. This aspect determine the ambient Alfvén speed, which is an important parameter for characterizing wave propagation in the corona and their subsequent effects. The Moreton wave we studied also exhibits a confined propagation direction to a certain sector, i.e., northeast from the flare site. The reason for this confinement is that the MHD fast-mode wave cannot reenter the chromosphere in directions in which strong magnetic field exists. Strong magnetic field also implies that high Alfvén velocity distribution dominates these regions; and because the wave front tends to propagate avoiding strong magnetic regions, the wave energy flux concentrates in directions of low Alfvén velocity. Therefore, the occurrence of this condition in the low corona favors the appearance of the Moreton wave in a restricted direction (see Uchida et al., 1973). Indeed, the Moreton wave on 2014 March 29 was directed towards non-magnetic or weak-field regions, i.e., high latitudes from the flare site, but not in opposite direction or towards the equatorial zone, places where high concentration of magnetic field could exist because of the presence of magnetic structures and some active regions. Zhang et al. (2011) also showed that the waves tend to propagate within a boundary of weak magnetic field regions based on the analysis of a set of Moreton waves.

3.6.2 Doppler Velocity of the Moreton Vave

The quantitative results of the perturbation in the chromosphere presented as the Doppler velocity in Figure 3.8 provide a direct sign of the disturbance in the corona and its effect on the chromosphere. The perturbation profiles show that the arrival of the coronal wave in the chromosphere produces disturbances along the four trajectories (P_1–P_4). However, its effect differs from one trajectory to another, and there is no a clear correlation among them in terms of amplitude as a function of distance and time. The wave propagation along path P_1 causes a very weak disturbance, whereas in the P_2, P_3, and P_4 directions the disturbances becomes gradually much more significant. It is also noted that in the earlier stage, i.e., at 17:45:59 – 17:47:20 UT, the highest downward velocity is observed particularly along the P_2, P_3 and P_4 trajectories. The velocity amplitude decreases later on. The difference of the velocity amplitude we found along each trajectory may be a consequence of the non-homogeneous layer (density and field strength) over which the wave propagates in the corona. In addition, because the downward component of the coronal wave interacts with a much denser layer, i.e., the chromosphere, most of its energy is reflected back into the corona and only a small fraction of it is able to reach deeper layers, triggering disturbances with strong effect in some localized regions, as observed in the Hα perturbation profiles. Furthermore, the wave fronts seen in the Doppler maps (see Figure 3.9 and the associated movie) progressively becomes wider and diffuse. This is indicative that the strength of the disturbance in the corona gets weaker at far distances from the source, meaning that some dissipative process is ongoing, and as a result, damping of the wave takes place, similar to the perturbation profiles. Vršnak et al. (2016) showed in their simulation results that after a certain time, the velocity amplitude of the chromospheric disturbance develops a small amplitude. The authors also reproduced the restoration process of the perturbed plasma, consistent with our observational results.

3.6.3 Characteristics of the Coronal Wave Based on Hα Observation

We have shown in Section 3.5.1 that the MHD linear theory and the Hα velocity amplitude of the Moreton wave, this latter interpreted as the velocity amplitude of the transmitted wave v_t from the corona to the chromosphere, allowed us to infer the velocity amplitude of the incident wave v_i in the corona under the assumption that the density ratio of chromosphere and corona is $a \approx 100$. It is important to emphasize that our calculation of v_i should be understood as the associated counterpart of v_t acting at the base of the corona. Taking the ratio of the velocity amplitude of transmitted and incident waves, we define the velocity transmittance $T_v = v_t/v_i$. This provides clues on how much fraction of the plasma velocity in the corona is transferred to the chromosphere when the shock front passes a specific location of the dense chromospheric layer. To illustrate this point, we assume that a extends from 1 to 100, and we also take $v_t = 4$ km s^{-1} and $v_i = 22$ km s^{-1}, corresponding to the derived values along path P_4 at 17:45:59 UT (see Table 3.2). It is shown in Figure 3.14 that as a increases, T_v is significantly reduced, so the effect of the density increase, e.g., the corona–chromosphere density jump, plays an important role. Takahashi et al. (2015) also found a similar tendency of velocity transmittance from 1D simulation of shock transmission to a prominence in their Figure 11.

From our findings we can further speculate that a wave traveling downward at the base of the corona with a velocity $\gtrsim 10$ km s^{-1}, this being the mean velocity amplitude of the incident wave calculated along trajectories P_3 and P_4 in Table 3.2, could be able to produce a noticeable disturbance in the chromosphere. We are aware that this is simply based on a linear analytic solution, but if the amplitude of the disturbance is so small, such as in the limit corona–chromosphere, the linear theory is applicable. Harra et al. (2011) and Veronig et al. (2011), based on *Hinode*/EIS observation of a coronal wave on 2011 February 16, reported a downward motion of the plasma in the corona with a velocity of about 20 km s^{-1}. The authors argued that the coronal wave pulse moving with such a speed was not strong enough to produce disturbances in the chromosphere. Indeed there was no Moreton wave, but activation of filaments in Hα line were identified associated with the referred coronal wave (see Cabezas et al., 2017). It should be mentioned that the reported downward motion was observed in Fe XII and Fe XVI spectral lines, which provide plasma diagnostics of coronal emission at $\log T/K \gtrsim 6.1$, whose formation region is believed to be located in the low or mainly in the intermediate corona, and it is likely that plasma moving downward with 20 km s^{-1} in such a place could not effectively travel deeper to overcome the inert chromosphere and produce a Moreton wave.

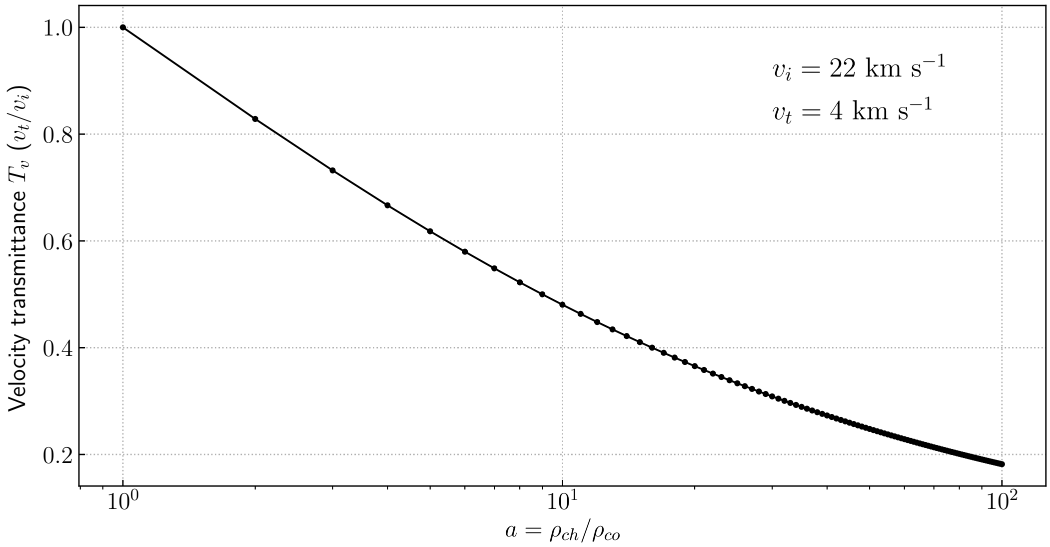

Figure 3.14: Velocity transmittance T_v defined as the ratio of the velocity amplitude of transmitted v_t and incident v_i waves. This provides clues on how much fraction of the plasma velocity in the corona is transferred to the chromosphere during the shock wave propagation. For illustration, the density jump a extends from 1 to 100, and we take $v_t = 4$ km s^{-1} and $v_i = 22$ km s^{-1}, corresponding to the trajectory P_4 at 17:45:59 UT (see Table 3.2). The plot shows that as a increases, T_v is significantly reduced.

3.6.4 Shock Strength in the Corona Based on DEM Analysis

The compression ratio profiles shown in Figure 3.12 reveal that the coronal wave propagates by exhibiting an irregular pattern along the different trajectories. It is found that the compression ratio, which is directly related to the shock strength, varies nonuniformly as a function of distance and time. On the basis of the shock-wave theory, the propagation and strength of the shock in the corona is governed by the action of the magnetic field and the ambient Alfvén speed distribution, and in the absence of a strong magnetic field, a high compression ratio is expected. Therefore, the high values of the compression ratio observed in the P_2, P_3, and P_4 directions, implying high Mach number (see Figure 3.13), suggest that these locations are more likely weak magnetic field regions. Consequently, the shock traveling in these directions could produce strong compression, resulting in a chromospheric disturbance with a relatively large amplitude. In fact, strong downward motions in the chromosphere are observed along the trajectories we described. This can be seen by comparing Figures 3.8 and 3.12, in which the highest values of the compression ratio along trajectories P_2, P_3, and P_4 approximately match in distance and time the large downward motion caused by the Moreton wave (see the associated animation of Figure 3.12 in the online journal). Of course, a comparison between the compression ratio and the velocity amplitude of the Moreton wave cannot be made directly because the compression ratio based on DEM ($6.1 \leq \log T/\mathrm{K} \leq 6.4$) is a plasma diagnostic of the wave traveling above the low corona. We are missing information of the plasma in the lowest-part of the corona. Nevertheless, the compression ratio profiles and the velocity amplitude of the Moreton wave show a good correspondence.

The disturbance created by the wave propagation would also result in an increase of the local plasma temperature. As we pointed out in Section 3.5.3, DEM solutions for $\log T/\mathrm{K} < 6.1$ do not show clear signs of the wave propagation. In contrast, in a range of much higher temperature, the disturbance seen as emission enhancement becomes more noticeable. Similar findings from a DEM analysis of coronal waves were also reported by Vanninathan et al. (2015) and Liu et al. (2018). Emission that increases at high temperatures is an indication of plasma heating, which is locally enhanced due to plasma compression as a result of the wave propagation. The heating effect also causes an intensity variation of much cooler emission lines. For example, at AIA 171 Å ($\log T{\sim}5.8$) coronal dimming (not shown here) is observed at the place of the wave front as a consequence of the plasma being heated to much higher temperatures (e.g., Wills-Davey & Thompson, 1999; Delannée, 2000; Liu et al., 2010; Nitta et al., 2013; Liu et al., 2018).

3.7 Summary and Conclusion

In this work we have studied in detail the Moreton wave on 2014 March 29 and its associated coronal counterpart. We combined multiwavelength observations, including Hα ±0.8 Å, He II (304 Å), coronal emission lines from AIA, and *Hinode* X-ray. This data set permitted us to further understand the nature of a globally wave propagation and its subsequent effects at different layers of the solar atmosphere. Such a global effect is clearly evidenced in Figure 3.4, wherein it is observed how the corona, transition region, and the chromosphere reacted to the large-scale disturbance. A co-spatial evolution of the wave in the corona and the Moreton wave in the transition region and the chromosphere are also noted, particularly in the initial stage of the propagation. This confirms a common origin.

Thanks to the observations in the wing of the Hα line performed by the FMT, we discussed the Doppler characteristics of the Moreton wave. We have shown that it is possible to quantify the downward motion of the chromospheric material traveling at the front of the Moreton wave. The plasma at this location attains a maximum velocity of about 4 km s^{-1}, which corresponds to the velocity amplitude of chromospheric motion associated with the Moreton wave. Our findings also showed that the chromospheric disturbance develops nonuniformly in terms of amplitude along the analyzed trajectories (see Figure 3.8). Furthermore, with the aid of the MHD linear theory, we also related our results of the Moreton wave velocity amplitude to that of the plasma velocity in the corona, allowing us to infer the velocity amplitude of the incident wave from the corona to the chromosphere. Additionally, we showed that by using the weak-shock approximation in conjunction with the velocity amplitude of the Moreton wave, the Mach number of the incident shock in corona could be estimated, and we obtained a consistent result with the AIA analysis. Very recently Long et al. (2019) attempted to characterize the perturbation caused by the Moreton wave studied in this paper, but the authors only used Hα line core observations, in which the signature of the perturbation cannot easily be distinguished.

The compression ratio analysis led us to conclude that the wave in the corona develops in a complex manner. This may depend on the conditions through which the wave propagates. As we noted in Figure 3.12, the compression ratio profiles vary as a function of distance and time, and also from one trajectory to another. This aspect also has a direct consequence on the change of the Alfvén and fast-mode Mach numbers, as presented in Figure 3.13. As for the Mach number, the values we calculated (i.e., $M_A \approx$1.06–1.28 and $M_f \approx$1.05–1.27) should be understood as representing the strength of the shock in a confined region of the solar corona because we restricted the compression ratio analysis to a DEM temperature range $6.1 \leq \log T/\mathrm{K} \leq 6.4$, the missed lowest part of the corona should be taken into account for further conclusions.

Finally, an extension of the present work will be important, especially focusing on the Doppler characteristics of the Moreton wave, a topic that is not fully understood and scarcely explored. More studies will help us to advance and clarify the direct connection between the downward-propagating component of the coronal wave and the chromospheric reaction leading to a Moreton wave. To this end, a combination of numerical experiments and observational results will be crucial. As for the observational matter, it will be further constrained with the Solar Dynamics Doppler Imager (SDDI; Ichimoto et al., 2017), now in operation on SMART telescope at Hida Observatory, Kyoto University, which provides high-resolution filtergrams with the spectral profiles in a wide spectral window around the Hα line center.

References

Cabezas, D.P., Martínez, L.M., Buleje, Y.J., et al. 2017, ApJ, 836, 33

Chen, P.F., Ding, M.D., Fang, C. 2005, ssr, 121, 201

Cheung, M.C., Boerner, P., Schrijver, C.J. 2015, ApJ, 807, 143

Delannée, C. 2000, ApJ, 545, 512

Eto, S., Isobe, H., Narukage, N., et al. 2002, PASJ, 54, 481

Golub, L., Deluca, E., Austin, G., et al. 2007, SoPh, 243, 63

Harra, L.K., Sterling, A.C., Gömöry P., Veronig, A. 2011, ApJL, 737, L4

Ichimoto, K., Ishii, T.T., Otsuji K., Kimura, G., et al. 2017, SoPh, 292, 63

Kosugi, T., Matsuzaki, K., Sakao, T., et al. 2007, SoPh, 243, 3

Kurokawa, H., Ishiura, K., Kimura, G. et al., 1995, JGG, 47, 1043

Landau, L.D., Lifshitz, E.M. 1987, Fluid Mechanics 2nd ed., (Pergamon Press)

Lemen, J. R., Title, A., Akin, D. J., et al. 2012, SoPh, 275, 17

Liu, W.L., Nitta, N.V., Schrijver, C.J., et al. 2010, ApJL, 723, L53

Liu, W., Jin, M., Downs, C., Ofman, L., et at. 2018, ApJL, 864, L24

Long, D.M., Jenkins, J., & Valori, G. 2019, ApJ, 882, 90

Moreton, G. E. 1960, aj, 65, 494

Moreton, G. E., Ramsey, H. E. 1960, PASP, 72, 357

Morimoto, T. & Kurokawa, H. 2003a, PASJ, 55, 503

Morimoto, T. & Kurokawa, H. 2003b, PASJ, 55, 1141

Morimoto, T., Kurokawa, H., Shibata, K., Ishii, T. T. 2010, PASJ, 62, 939

Narukage, N., Hudson, H.S., Morimoto, T., et al. 2002, ApJ, 572, L109

Narukage, N., Moritmoto T., Kadota, M., et al. 2004, PASJ, 56, L5

Narukage, N., Ishii, T.T., Nagata, S., UeNo., S., et al. 2008, ApJ, 684, L45

Narukage, N., Sakao, T., Kano, R., et al. 2011, SoPh, 269, 169

Nitta, N.V., Schrijver, C.J., Title, A.M., Liu, W. 2013, ApJ, 776, 58

Pesnell, W. D., Thompson, B. J., Chamberlin, P. C. 2012, SoPh, 275, 3

Priest, E. R. 2000, Solar Magnetohydrodynamics (Dordrecht: Reidel)

Shibata, K., Kitai, R., Katoda, M., et al., 2011, Solar Activity in 1992-2003, (Kyoto: Kyoto University Press)

Takahashi, T., Asai, A., Shibata, K. 2015, ApJ, 801

Uchida, Y. 1968, SoPh, 4, 30

Uchida, Y., Altschuler, M., Newkirk, G. 1973, SoPh, 28, 495

UeNo, S., Shibata, K., Kimura, G., Nakatani, Y., Kitai, R., Nagata, S. 2007, Bull. Astr. Soc. India, 35, 697

Vanninathan, K., Veronig, A.M., Dissauer, K., et al., 2015, ApJ, 812, 173

Veronig, A. M., Gömöry P., Kienreich, I. W., ApJL, 743, L10

Vršnak, B., Magdalenić, J., Aurass, H., & Mann, G. 2002a, A&A, 396, 673

Vršnak, B., Žic, T., Lulić, S., Temmer, M., Veronig, A.M. 2016, SoPh, 219, 89

Wills-Davey, M.J., Thompson, B.J., 1999, SoPh, 190, 467

Zhang, Y., Kitai, R., Narukage, Y., et al. 2011, PASJ, 63, 685

Chapter 4

A Fast-filament Eruption Observed in the Hα Line by SMART/SDDI: I. Observational Aspects

4.1 Motivation

It is currently well known that filament and prominence eruptions are one of the principal sources of coronal mass ejections (CME), and also it is argued that the parameters that determine the geoeffectiveness of CMEs when impact with the Earth's magnetosphere are the velocity and the magnetic orientation. Besides, investigations of prominence/filament eruptions have also revealed that there is a good correlation between the ascending speed and the direction of the filament eruptions with CMEs. Therefore, the dynamic of the erupting filaments can be used as a diagnostic tool for investigating the very beginning stage of the CME formation and its kinematics.

The dynamics of filament eruptions and/or filaments disappearance in the Hα line, have extensively been studied in the last decades, even in the present days. However, the majority of the studies use the projected motion of the erupting filaments as representing values of the velocity, lacking information about the line-of-sight component; while other studies only show line-of-sight velocities of a few km s^{-1}. The difficulties in detecting the line-of-sight component of a filament eruption relies mainly on the very limited spectral range in which the filtergrams are recorded, and the small FOV is case of spectrographs. Because of the importance in detecting the line-of-sight velocity of filament eruptions, particularly of those composed of very large bulk motions that can produce geoeffective CMEs, in 2016 a new instrument called the Solar Dynamics Doppler Imager (SDDI; Ichimoto et al., 2017) has been installed on the SMART telescope at Hida Observatory. The SDDI is capable to record filtergrams in a wide range of wavelengths around the Hα line, and is suitable to capture high-speed eruptions with velocities up to 400 km s^{-1} along the line-of-sight. These characteristics allows us to perform imaging and spectral diagnostics of high-speed events.

In this Chapter we present a study of a fast-filament eruption observed by the SDDI on 2017 April 23. The eruption was captured in a wide spectral window around the Hα line center. We applied the "cloud model" to derive the line-of-sight velocity of the overall erupting filament, and also we performed a spectral analysis of the eruption focusing on the filament apex. The spectral analysis reveals signatures of strongly blue-shifted plasma up to −8.0 Å from the line center, meaning that the filament was ejected with a velocity of ~365 km s^{-1} in direction to the Earth. We also estimated the apparent velocity and acceleration of the eruption at the apex, resulting in 700 km s^{-1} and 3 km s^{-2}, respectively. Furthermore, by using the results of the "cloud model" we attempted to estimate mass density of the filament, which lead us to discuss the mechanical energy of the filament during the eruption.

4.2 Observations

4.2.1 SMART/SDDI Observation

The Solar Magnetic Activity Research Telescope (SMART; UeNo et al., 2004) consists of four refractive telescopes (see Ishii et al., 2013; Nagata et al., 2014). SMART/T1 telescope designed to observe full-disk solar images in the Hα line had an observing system covering a very short number of wavelengths (up to ±1.2 Å). That is, the former filter-scan of T1 only permitted detections of relatively small Doppler velocity of filament and prominence eruptions because the wavelength offset of the Hα filter was insufficient to detect high speed events. Since 2016, the observing system of SMART/T1 was upgraded with a new Hα imaging instrument called the Solar Dynamics Doppler Imager (SDDI; Ichimoto et al., 2017). This unique instrument consisting of a Lyot type birefringent tunable filter incorporates liquid-crystal variable retarders, and is capable to record successively full-disk solar images at 73 wavelength positions of the Hα spectral profile, spanning −9 to +9 Å from the line core with a wavelength step of 0.25 Å. We are therefore not only able to perform imaging analysis, but also spectroscopy diagnostics of high-speed mass motions comprised of large dynamic range of Doppler velocity (±400 km s^{-1}). The spatial sampling and time cadence of the SDDI is $\sim 1''.23$ pixel^{-1} and 15 s (for the 73 wavelengths), respectively.

We applied standard calibration procedures of dark-current subtraction and gain corrections (flat-fielding) to the data presented in this work. Because the flat-pattern is wavelength dependent of the tunable filter, we implemented individual flat-field images for each of the 73 SDDI spectral positions by using the method of Kuhn-Lin-Loranz (Kuhn et al., 1991). The resulting flat-field images were applied wavelength-by-wavelength to the corresponding data sequence. Figure 4.1 shows a full-disk solar image in the Hα line taken by the SDDI on 2017 April 23 at 05:10:36 UT. In the bottom panel of the figure we also present the Hα spectral profile obtained from a quiet region and re-scaled to the Atlas solar spectrum. Additionally, we show the result of the convolution of the Atlas solar spectrum with the SDDI filter-transmission profile. An example of strongly blue-shifted spectral profile, corresponding to the lateral part of the filament eruption at 05:44:50 UT is also included in the figure.

4.2.2 SDO/AIA and STEREO/EUVI Observations

We complement our investigation with Extreme Ultraviolet (EUV) observations taken by the Atmospheric Imaging Assembly (AIA; Lemen et al., 2012) onboard the Solar Dynamics Observatory (SDO; Pesnell et al., 2012), and the side-view by the Extreme-Ultraviolet Imager (EUVI) from the Sun-Earth Connection Corona and Heliospheric Investigation (SECCHI; Howard et al., 2008) onboard the Solar Terrestrial Relations Observatory (STEREO; Kaiser et al., 2008). We use AIA and EUVI images at 304 Å dominated by He II and sensitive to a temperature of $\log T/K \sim 4.7$. The spatial sampling of the AIA and EUVI are $\sim 0\farcs6$ pixel^{-1} and $\sim 1\farcs58$ pixel^{-1}, while the temporal resolution 12 s and 5 min, respectively. On 2017 April 23, the separation angle between STEREO-A and the Earth was about 138 deg. Figure 4.2 shows the evolution of the filament eruption as observed by AIA and EUVI instruments in the EUV passband (304 Å).

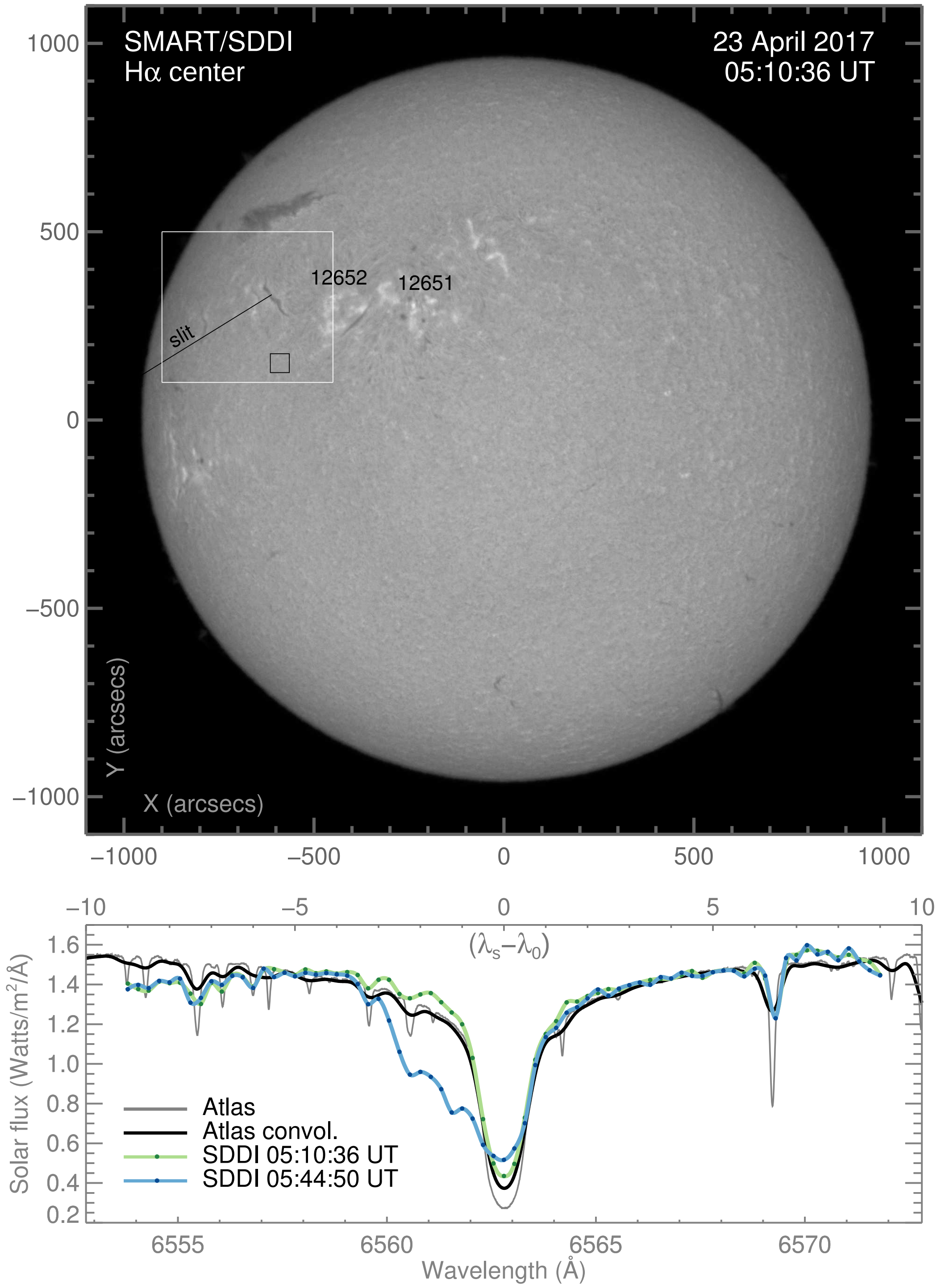

Figure 4.1: Upper: solar disk image at Hα +0.0 Å recorded by the Solar Dynamics Doppler Imager (SDDI) at Hida Observatory. The white box outlines the FOV studied in this work, while the small black box ($50'' \times 50''$) surrounds the quiet-Sun region from which the spectral profile is obtained and plotted in the bottom panel. In the FOV an artificial slit is positioned along the direction of the eruption intended to trace the leading edge (apex) of the erupting material. Bottom: Atlas solar spectrum of the Hα line (gray), and the result after convolving the atlas with the SDDI filter-transmission profile (black). It is also shown SDDI spectral profiles of a quiet region (green dots with standard spline interpolation) obtained at 05:10:36 UT, and an example of a strongly blue-shifted profile (blue dots with spline interpolation) obtained from the lateral part of the filament eruption at 05:44:50 UT. The SDDI spectral profiles are re-scaled to the atlas profile, where each dot does correspond to the wavelength offsets λ_s from the line center λ_0 (6562.8 Å) at which the SDDI performs the observations.

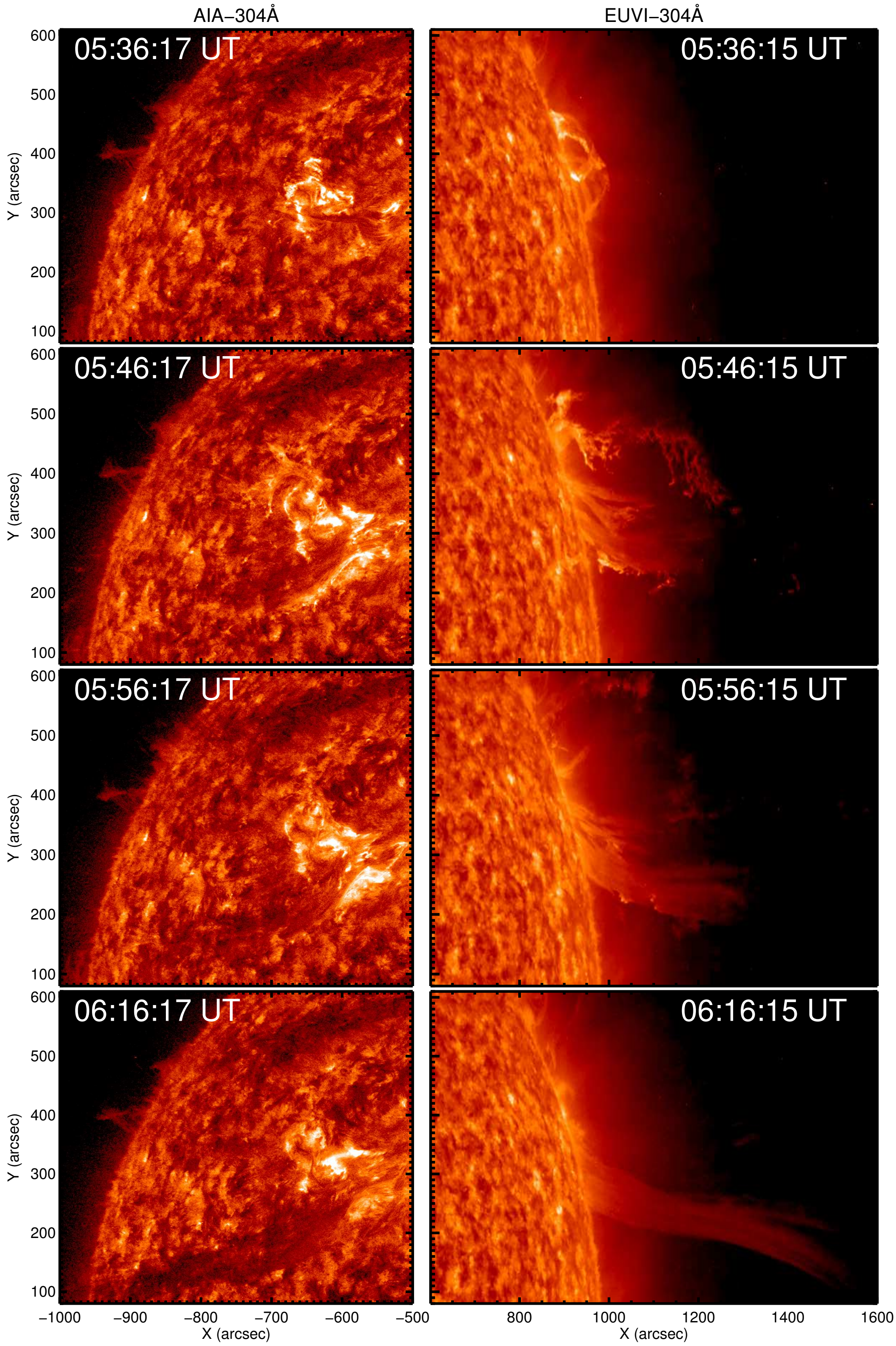

Figure 4.2: Filament eruption captured in EUV (304 Å) by AIA and EUVI instruments on 2017 April 23. The STEREO-A/EUVI images (right panels) show the side view of the eruption, because during the eruption it was located 138 deg ahead of the Earth.

4.2.3 Overview of the Event

On 2017 April 23, the position of the studied target in heliographic coordinates was N16 E45 ($X = -652''$, $Y = 329''$), located in the easter side of active region 12652 (see Figure 4.1). Signatures of activation and slow-rising of the filament are observed from 05:24 to 05:30 UT, which becomes more visible in core-wing wavelengths (0.25–2.0 Å). Then, at about 05:30 UT a growing arc-shaped structure starts to expand rapidly whose characteristics in absorption becomes noticeable in the far blue-wing of the Hα line (see Figure 4.3). As the expansion takes place, signs of untwisting motions is also identified in the legs, but they remain anchored to the solar surface. The disruption occurs on the top of the arc-shaped structure (apex), and it happens at about 05:38 UT. This may indicate the instance at which the growing structure reached to a critical height, as theorized by several authors (e.g., Filippov & Den, 2001; Kliem & Torok, 2006, and references therein). Subsequently, the cool material is expelled into the interplanetary space, but the plasma comprised in the legs remain rooted and expands sideward. At about 05:41 UT part of the ejected filament falls back onto the solar surface but a great portion persists ascending, then it simply fades from the Hα images. This suggests that the ejecta reached higher altitudes of the solar atmosphere, and also because it is expected that the temperature and the ionization rate increases during the eruption, the hot moving plasma does no longer emit the chromospheric lines.

A time-series of the filament eruption is presented in Figure 4.3. The maps are results of the difference between the mean intensity of the blue- and red-wing images, that is, mean intensities calculated from a set of images in the wavelengths range of H$\alpha \pm [0.25 : 2.0]$, H$\alpha \pm [2.25 : 4.0]$, H$\alpha \pm [4.25 : 6.0]$, and H$\alpha \pm [6.25 : 8.0]$, respectively. The maps illustrate the overall evolution of the filament eruption, in which the material directed toward the Earth is observed in absorption blue-shift (dark), while the component moving in opposite direction is seen in emission red-shift (bright). From 05:41 UT, highly blue-shifted material is detected at very far-wing wavelengths (H$\alpha \pm [6.25 : 8.0]$), indicating that part of the filament was ejected having a line-of-sight velocity higher than 285 km s^{-1}.

In the GOES soft X-ray data, an enhancement of the emission begins at about 05:37 UT associated with an B2-class flare. This weak flare is very likely related to the filament eruption, but we should point out that because the time lag between the onset of the eruption and the GOES flux enhancement, the flare may be is a consequence of the filament eruption but not the triggering source.

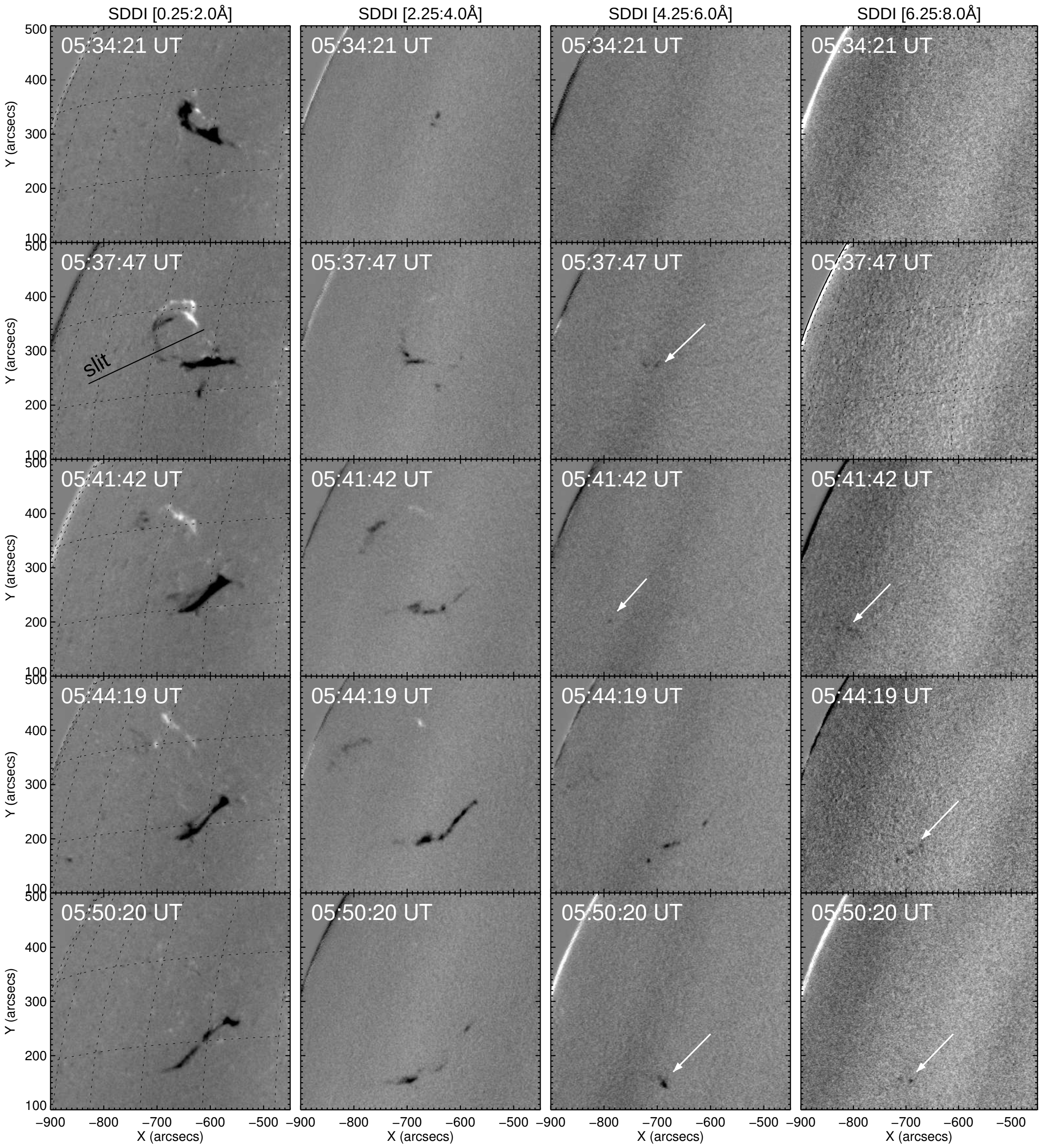

Figure 4.3: Time sequence of the filament eruption captured by the SDDI on 2017 April 23. The maps show dark and bright features of the erupting material, in which the dark structures correspond to the material moving toward the observer, while the bright features indicate the motion of the material in opposite direction. As the eruption develops highly blue-shifted material (in absorption) can be recognized at wavelengths larger than 6.25 Å from the line center, indicating that part of the filament was ejected with a line-of-sight velocity higher than 285 km s^{-1}.

4.3 Analysis and Results

4.3.1 Velocity and Acceleration Profiles

Apparent Motion

In Section 4.2.3, we mentioned that the arc-shaped filament exhibits a rapid growing characteristics from about 05:30 UT. To clearly show the rising evolution of the filament, we performed height-time measurements based on the Hα intensity variation through an artificial slit positioned in the direction of the fast-rising structure (filament apex) (see Figure 4.3). The intensity variation is obtained from mean intensity maps, resulted from the combination of Hα images in a wide range of wavelength, similar to the maps shown in Figure 4.3. In principle the height-time diagrams obtained from our observations allows to trace the leading edge of the erupting material in the plane-of-sky, however, because the SDDI records filtergrams at several positions around the Hα line, the height-time diagrams also provide insights into the line-of-sight component of the erupting material. In Figure 4.4 we present the results, wherein it is noted that depending on the wavelength range at which the height-time plots are obtained, different components at the apex of the filament eruption are observed. In the core and near-wing height-time diagrams (H$\alpha \pm [0.0 : 2.0]$) the slow-ascending phase and the onset of the eruption is observed exhibiting an exponential-like evolution. In contrast, in more far-wing diagrams (H$\alpha \pm [2.25 : 4.0]$, H$\alpha \pm [4.25 : 6.0]$), the fastest component of the eruption becomes more evident indicating also strong blue-shifted plasma during the main eruption.

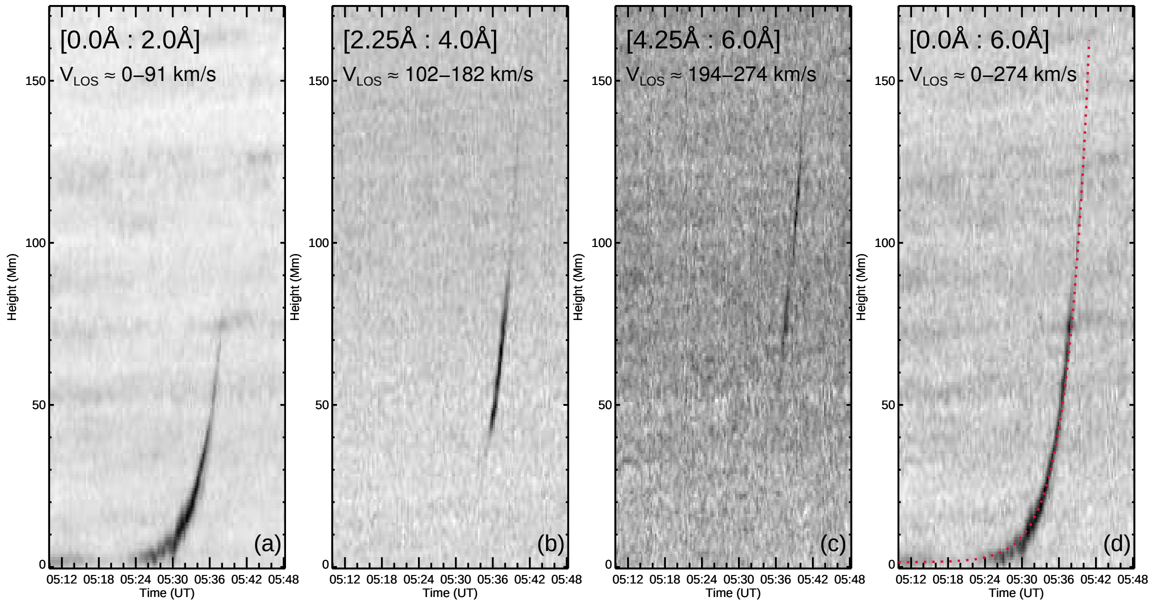

Figure 4.4: Height-time diagrams obtained from the intensity variation along an artificial slit placed in the direction of the leading edge of the filament eruption. The diagrams were obtained from composite maps resulted from the combination of images in the Hα center and in the red and blue wings, that is, H$\alpha \pm [0.0 : 2.0]$ (panel a), H$\alpha \pm [0.25 : 4.0]$ (panel b), H$\alpha \pm [4.25 : 6.0]$ (panel c), and H$\alpha \pm [0.0 : 6.0]$ (panel d), respectively. The height-time diagrams provide not only the time evolution of the eruption in the plane-of-sky, but also information of the line-of-sight component. In the diagrams the following characteristics of the ejection can be seen: the slow-ascending motion at core-wing wavelengths, and the fastest-rising at far-wing wavelengths. In the height-time diagram of panel (d), the red dotted line is the best-fit based on the selected points measured along the dark lane (ejection).

Similarly, based on the intensity variation along an artificial slit located in the direction of the leading edge of the eruption, height-time diagrams are also obtained from AIA-304 Å intensity and running-difference maps (Figure 4.5). In the height-time diagram of 304 Å, in addition to the leading edge of the filament eruption, it is also noted much cool structures of the eruption moving behind (left panel in Figure 4.5). The right panel of Figure 4.5 shows a comparative height-time profiles of 304 Å and Hα, obtained by fitting the measured points in each height-time diagram. The profiles show that before the rising and the main phase of the eruption, the structure evolves identically in Hα and at 304 Å; although at 304 Å which provides diagnostics of the transition region, signs of the eruption lasts for much longer period and attains greater heights. The profiles also reveal a slow-rising and fast-rise exponential evolution of the eruption, both in Hα and at 304 Å. We note that the height-time profile of Hα is well fitted by an exponential function, while the profile at 304 Å results from the combination of an exponential function for the fast-rise and a polynomial function for the later phase.

Based on the fitting results of the height-time profiles presented in Figures 4.4 and 4.5, the height, velocity and acceleration profiles of the leading edge (apex) of the filament eruption are obtained (Figure 4.6). The velocity profiles show that the filament starts to grow exponentially at about 05:30 UT, when the filament attained a height $h \simeq 10$ Mm. The velocity profiles derived from Hα and 304 Å progresses quasi-identically until 05:39 UT, time when the profile at 304 Å starts to slow-down and drastically falls-back at around 05:41 UT. This time also corresponds to the instant at which signatures of the eruption in Hα becomes invisible. The acceleration profiles also develop similarly in Hα and at 304 Å during the early and main stage of the eruption, then at 304 Å start to rise ahead of Hα. As in the velocity profile, the acceleration at 304 Å experiences a sudden decrease, a strong deceleration starts to occur at about 05:39 UT. It should be mentioned that the involved error in the estimation of the velocity and acceleration could be large because the role of the projection effect in the height-time measured points, and further the uncertainty becomes larger as one takes successive time derivatives.

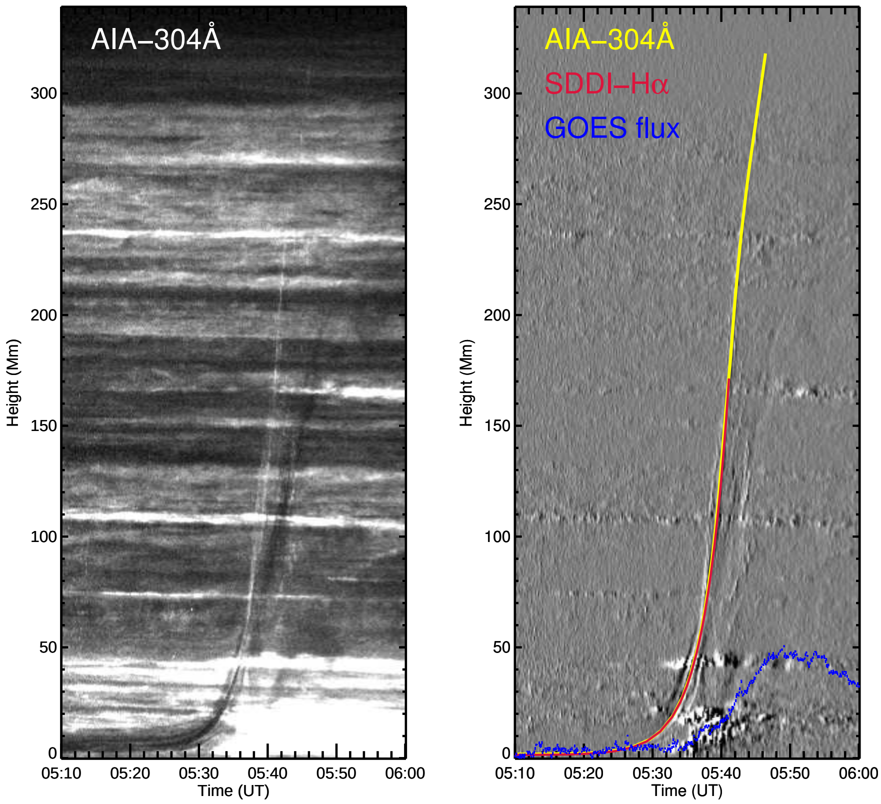

Figure 4.5: Left: height-time plots of AIA-304 Å along the rising direction of the filament eruption, obtained from the intensity variation along an artificial slit (see the text). In the diagram two main characteristics are observed, a bright leading part or fastest component and a more wider dark structure moving behind. Right: the background image is same as in the left panel but resulted from running-difference AIA-304 Å maps. The yellow and red profiles are the best-fitting results of the measured positions along the AIA-304 Å and Hα height-time plots, respectively. The GOES flux $(1 - 8$ Å$)$ is also plotted to show the time evolution of the associated B-class flare.

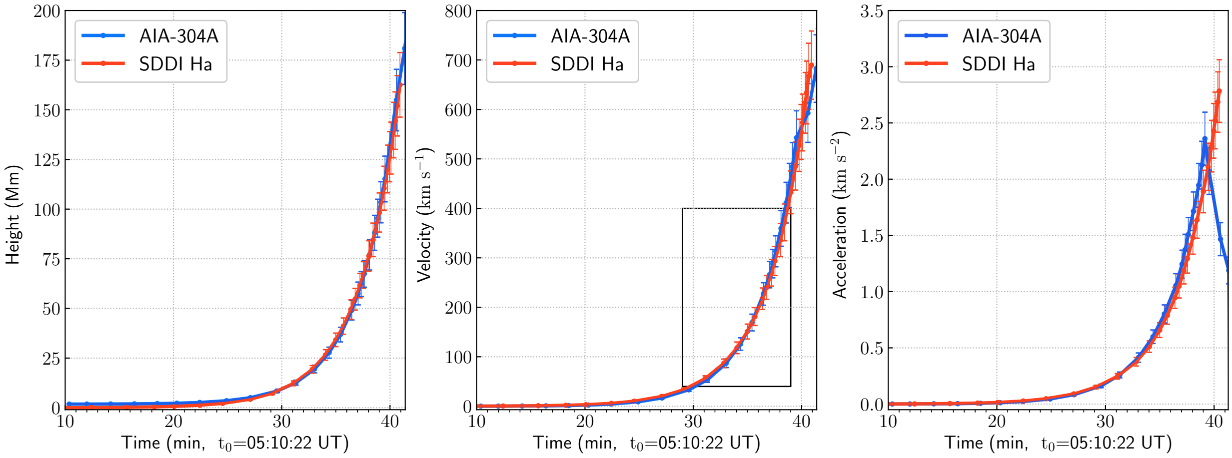

Figure 4.6: Height, velocity, and acceleration profiles of the filament eruption on 2017 April 23. The profiles were obtained by fitting the selected points in the height-time diagrams of AIA-304 Å and Hα, respectively (see the text). The inset box in the velocity profile outlines the time period of the fast-rising stage of the eruption that is considered for further analysis.

Transverse Velocity

The motion of fine structures inside the filaments and in others solar features are often measured by applying optical flow techniques, such as the local correlation tracking (LCT) method. The LCT method computes the displacement vectors between two consecutive images by tracing the blobs contained inside the structure, and thus, the transverse velocity of the moving structure can be determined. We applied the LCT method to automatically track the horizontal flows inside the filament in x and y directions, and the obtained parameters are used to calculate the velocity vectors. Figure 4.7 (upper panels) shows a sequence of transverse velocity maps derived from our Hα data, wherein the directions of the velocity vectors are represented by the arrows. In the Figure and with the help of the velocity vectors, one sees that as the eruption progresses the filament undergoes an untwisting motion. Additionally, in the bottom panels of Figure 4.7 we show velocity maps of the filament eruption at 05:35:08 UT obtained from the LCT method. The maps show the velocity distribution of the eruption in the x and y directions, and also the magnitude computed by combining the x and y components. Because the magnitude is a quantity that describes how fast an object is moving as a function of time regardless the direction, it is noted that the fastest component of the eruption is concentrated mainly at the leading edge of the eruption having an apparent velocity higher than 140 km s^{-1}.

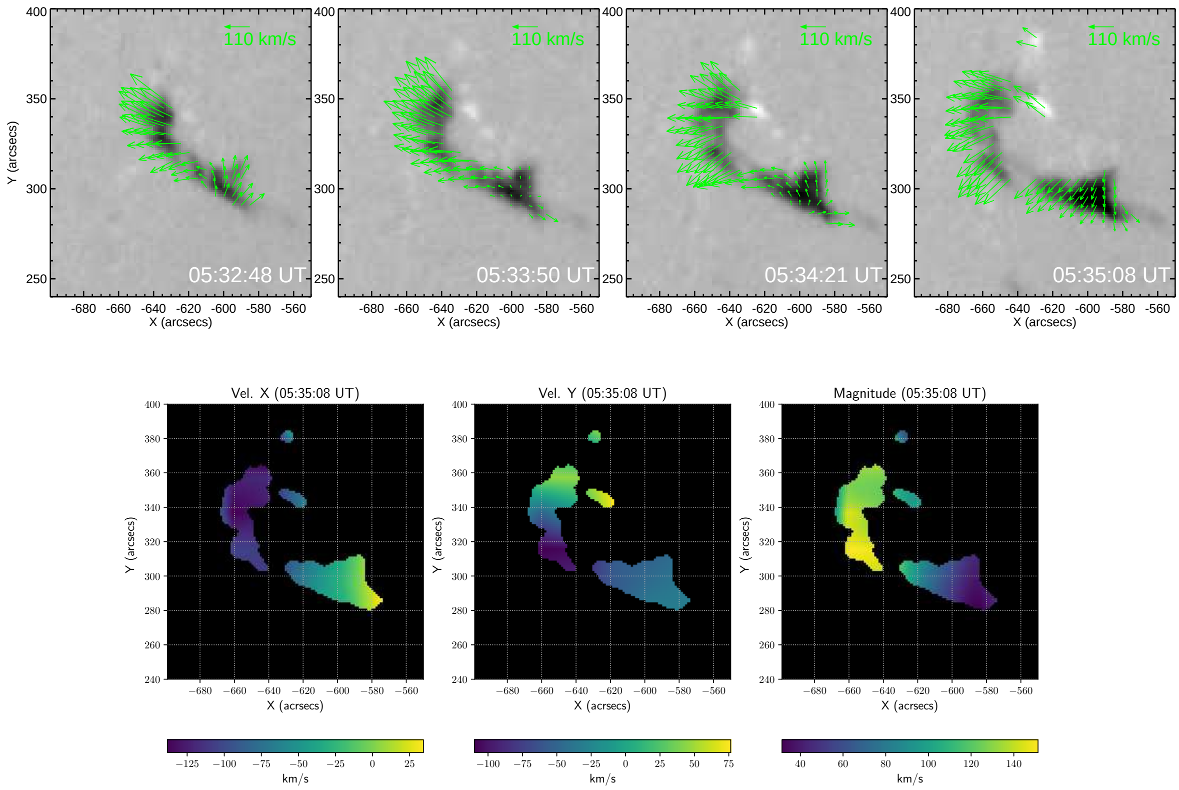

Figure 4.7: Upper: time-sequence of flow velocity based on LCT method (see the text). In the maps it is noted that the velocity vectors (arrows) outline well the motions of the structures contained in the filament body. The observed characteristics resembles an expansion and untwisting motion of the filament eruption. Bottom: velocity distribution in x and y directions, and the magnitude of the filament eruption at 05:35:08 UT derived from the LCT method.

4.3.2 Line-of-sight Velocity of the Filament Eruption

Cloud Modeling

The classical "cloud model" introduced by Beckers (1964) is an effective tool for deriving the line-of-sight velocity of chromospheric fine structures, and also of eruptive filaments and prominences. In the model such structures are considered as chromospheric "clouds" located well above from the solar surface, which absorb the incident radiation coming from below. The mathematical form of the "cloud model" is based on the radiative transfer equation, in which the radiation passing through and emerging from the cloud-like structure is defined as

$$I(\Delta\lambda) = I_0(\Delta\lambda)e^{-\tau(\Delta\lambda)} + \int_0^{\tau(\Delta\lambda)} S_t e^{-t(\Delta\lambda)} dt, \tag{4.1}$$

where $I(\Delta\lambda)$, $I_0(\Delta\lambda)$, $\tau(\Delta\lambda)$, and S are the observed intensity, the background or incident radiation, the optical depth, and the source function, respectively. The formal solution of

Equation (4.1) is based on the assumption that the structure or filament is fully isolated from the underlying chromosphere and, the source function, the Doppler width, and the absorption coefficient are constant along the line-of-sight. Under this condition the radiative transfer equation is rewritten as (Tziotziou, 2007):

$$I(\Delta\lambda) = I_0(\Delta\lambda)e^{-\tau(\Delta\lambda)} + S(1 - e^{-\tau(\Delta\lambda)}). \tag{4.2}$$

Taking this solution the contrast profile $C(\Delta\lambda)$ is defined as follows

$$C(\Delta\lambda) = \frac{I(\Delta\lambda) - I_0(\Delta\lambda)}{I_0(\Delta\lambda)} = \left(\frac{S}{I_0(\Delta\lambda)} - 1\right)(1 - e^{-\tau(\Delta\lambda)}), \tag{4.3}$$

where the variables at the left-part of Equation (4.3) can be determined from the observations. Furthermore, it is assumed that the optical depth is well represented by a Gaussian profile

$$\tau(\Delta\lambda) = \tau_0 e^{-\left(\frac{\Delta\lambda - \Delta\lambda_I}{\Delta\lambda_D}\right)^2}, \tag{4.4}$$

here τ_0 is the optical depth at the line center, $\Delta\lambda_I = \lambda_0 v/c$ is the Doppler shift of the line due to the line-of-sight motion of the cloud being λ_0 the Hα line center wavelength, and $\Delta\lambda_D$ is the Doppler width. Taking the previous considerations, we applied the "cloud model" to our Hα observations for deriving the physical parameters described above of the filament eruption on 2017 April 23, that is: the source function, optical depth, Doppler width, and the Doppler shift.

Using the results of the Doppler shift, we obtained velocity maps of the filament eruption that are presented in Figure 4.8. The figure shows the Doppler characteristics of the filament eruption, wherein it is observed that after the disruption that occurs at about 05:38:17 UT, a great portion of the erupting material is launched in direction to the Earth (line-of-sight) with a velocity of about 300 km s^{-1}. In Figure 4.9 we present the resulting maps of the Optical depth and Doppler width at 05:36:44 UT, the figure also includes the time-profile of these parameters obtained at the filament apex. The Optical depth and the Doppler width profiles are used to estimate the mass density of the filament, and the result is presented in Section 4.3.3.

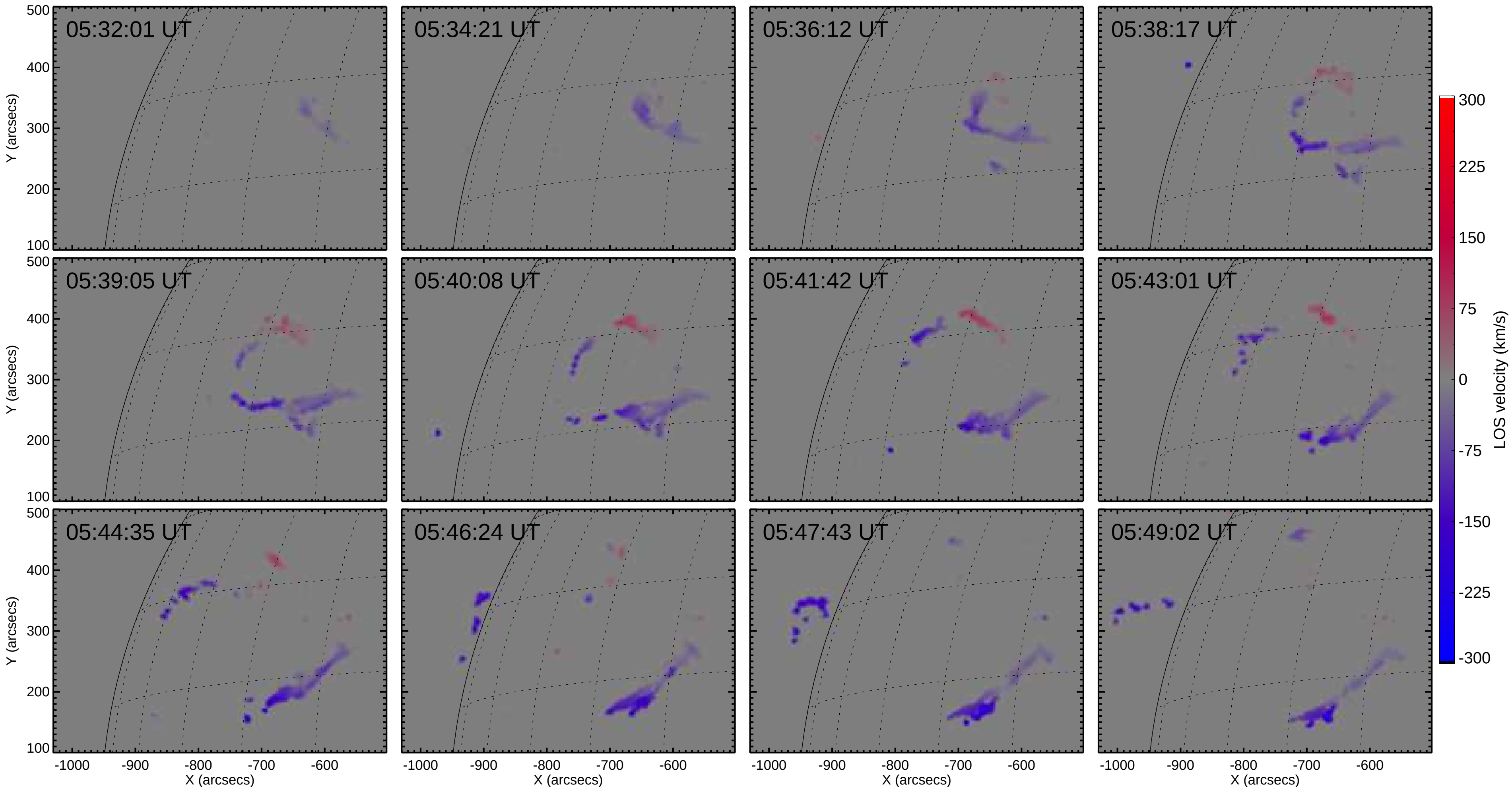

Figure 4.8: Velocity maps of the filament eruption derived from the "cloud model". The event was captured by the SDDI on 2017 April 23, at Hida Observatory. The maps show the Doppler characteristics of the filament eruption, wherein clearly can be seen that a great portion of the erupting material is moving in direction to the Earth (the negative values represent the motion towards the observer).

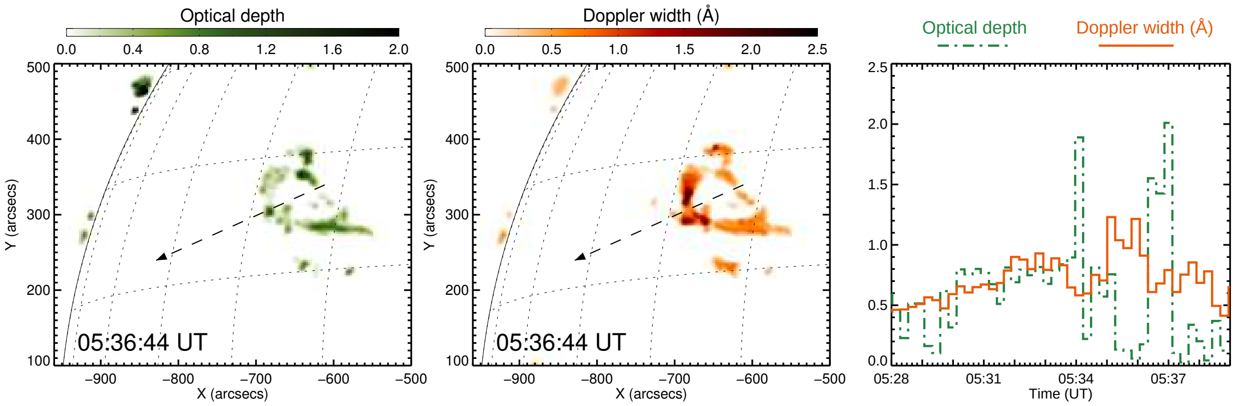

Figure 4.9: Optical depth and Doppler width maps obtained from the "cloud model". In the maps the straight dashed lines outline the path of the fast-rising part of the eruption (apex), along which the time evolution of the optical depth and Doppler width are measured from successive images (right panel). Based on these results the mass density of the filament eruption is calculated (see the text).

Spectral Analysis

The observing system of the SDDI is optimized to map full-disk solar images by recording a series of filtergrams at 73 positions of the Hα spectral profile, therefore, we can also obtain 2d-spectrum at any point and location on the solar disk. Because our interest is to study the filament eruption, with special attention of the leading edge (apex), we obtained a series of 2d-spectrum positioning an artificial slit along the rising direction of the filament, same as for the height-time diagrams in Section 4.3.1. This is a convenient manner to trace the structure of the erupting material in space, time, and wavelength $\Delta\lambda$. From the resulting 2d-spectrum, we further calculate the contrast by using Equation (4.3), in which the spectrum at 05:25:29 UT was taken as the background radiation $I_0(\Delta\lambda)$. The 2d-contrast images allows to extract contrast profiles at every positions of the eruption, which are physically more meaningful than the intensity profiles themself. This leads us to estimate more precisely the Doppler shift and to derive the line-of-sight velocity at the apex of the filament eruption. Examples of the 2d-contrast images, contrast profiles, and fitting results corresponding to the filament apex are presented in Figure 4.10.

In the contrast images (top panels of Figure 4.10) the erupting material is seen as an elongated dark structure originating from the line core (6562.8 Å), it becomes faint as the time goes on, indicating that possibly the material reached higher altitudes of the solar atmosphere. In the contrast profiles (middle and bottom panels of Figure 4.10) the leading, core, and the following parts of the eruption are highlighted in green, black, and red, respectively (see the positions in the top panels). The depletion in the contrast profiles indicate the line-shift of the

Hα profile. We note that during the later stage of the eruption the amplitude of the depletion is reduced, but become wider and strongly shifted blue-ward. We use as representing line-of-sight velocity the fitting results of the core contrast profiles (black), which are used to calculate the total velocity of the filament eruption. Although it should be mentioned that higher line-of-sight velocity is present especially in the later phase of the eruption, that are seen weakly in the leading contrast profiles (green).

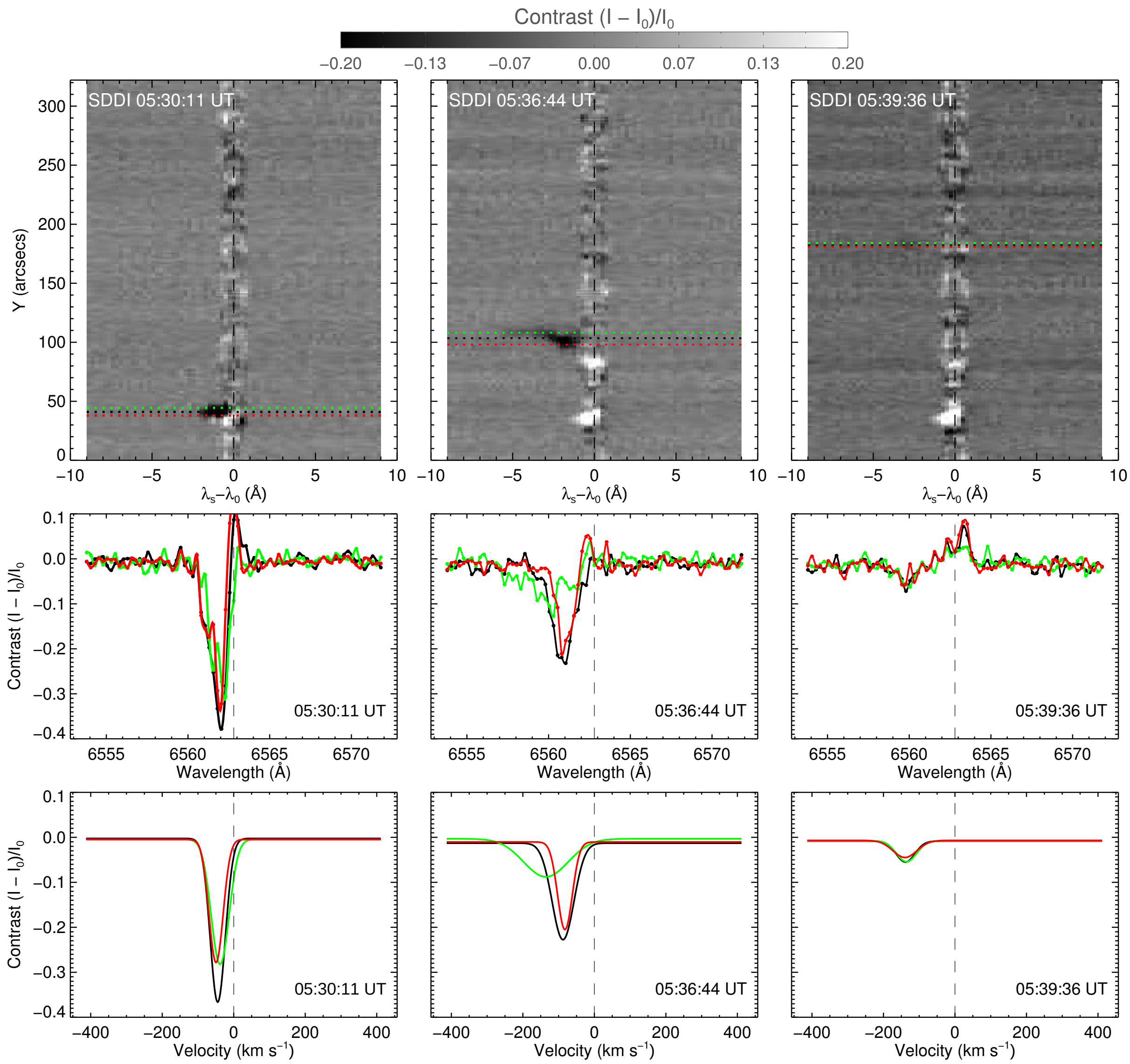

Figure 4.10: Top row: 2d-spectrum (contrast) at three instants of the filament eruption. The erupting material is observed as absorption (dark structure) propagating upward from the line center (6562.8 Å). The horizontal dotted lines (green, black, and red) outline the positions from which the contrast profiles are obtained. Middle and bottom rows: contrast profiles extracted from the 2d-spectrum and the fitting results, respectively. The green, black, and red profiles represent the leading, core, and the following parts of the erupting material. The middle row show the line-shift caused by the eruption, while in the bottom row it is shown their corresponding line-of-sight velocity. In the profiles at 05:30:11 and 05:36:44 UT (middle row), up-down patterns are identified, possibly related to internal motions inside the filament which causes asymmetric shapes of the spectral profile.

4.3.3 The Mechanical Energy of the Filament Eruption

In studying the dynamic of the filament eruption it is also useful to investigate the mechanical energy. The governing equation of the mechanical energy E_{mc} of an erupting filament is defined as the sum of the kinetic E_k and the potential E_p energies (see also Morimoto et al., 2010):

$$E_{mc}(x,t) = \frac{1}{2}\rho_m \; v(x,t)^2 + \int_{R_\odot}^{H(x,t)+R_\odot} G\frac{M_\odot . \rho_f}{r^2} dr, \tag{4.5}$$

here E_{mc} is the energy gained by an element x inside the volume of the filament at an arbitrary time t. In the kinetic part of Equation (4.5) the mass density of the filament is denoted by ρ_m, while $v(x,t)$ represents the total velocity of the filament eruption. The potential part of the equation is composed by the solar radius $R_\odot$, solar mass $M_\odot$, gravitational constant G, and the radial height $H(x,t)$; the later being a function of the upward velocity. In our analysis the total velocity at the apex of the eruption is calculated by combining the plane-of-sky and line-of-sight velocities, as illustrated in Figure 4.11. The calculation of the total velocity is focused on the fast-rising stage of the eruption, in the time-range 05:29 to 05:39 UT (see also Figure 4.6). We recall that the plane-of-sky velocity is based on the height-time measurements, while the line-of-sight velocity comes from the line-shift observed in the contrast profiles.

An important parameter in Equation (4.5) is the mass density of the filament, which in principle cannot be derived only from Hα observations. Besides, the problem we are dealing with is a case of highly moving filament eruption rather than a quiescent or a static situation. Therefore, either we can simply assume a constant value for the mass density (e.g, Hanaoka & Shinkawa, 1999; Morimoto et al., 2010) or move forward. We attempted to estimate the mass density of the erupting material using the already derived optical depth and Doppler width from the cloud model (Figure 4.9), also considering the relations introduced in Yakovkin & Zeldina (1975) and Tsiropoula & Schmieder (1997). Under the assumption that the path length of the filament along the line-of-sight is $d \approx 10^4$ km, we obtained the time variation of the number density in the second hydrogen level N_2, the electron density Ne, the total particle density of hydrogen N_H, and the needed mass density ρ_m. We stress that our calculation of the mass density is very crude, because the used equations constitute solutions for small cloud velocities (< 10 km s^{-1}), such as chromospheric fine structures, mottles, spicules, and for penumbral fibrils (see Tsiropoula, 2000). In case of eruptive prominences and filaments that are comprised of large bulk motions, one has to take into account the influence of the so-called Doppler brightening effect (DBE). In the literature it is documented that the DBE takes place when the amount of the photospheric-chromospheric radiation incident on the moving cloud increases due to the relative motion of the scattering cloud with respect to the solar surface (Heinzel & Rompolt, 1987). For instance, we will not consider the effect of the DBE in the present study, a future paper will discuss details of the DBE. The estimated N_2, Ne, N_H, and ρ_m at the filament apex are presented in Figure 4.12, which correspond to the fast-rising period of the eruption. The resulting mass density is used to derive the kinetic and potential energies of the filament eruption, as given in Equation (4.5).

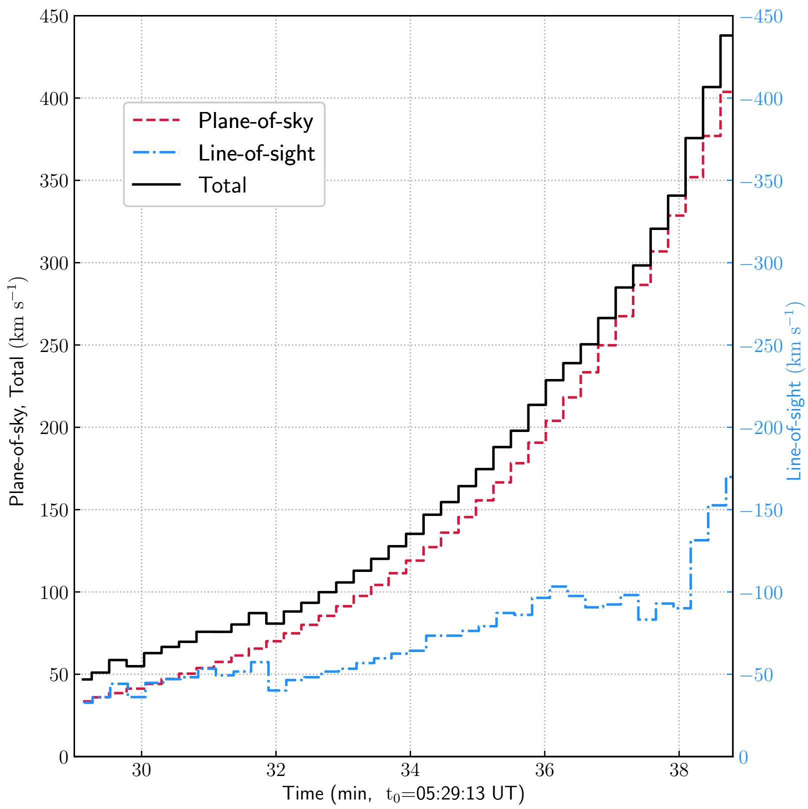

Figure 4.11: Velocity profiles of the filament eruption calculated at the apex during the fast-rising phase. The line-of-sight velocity (blue) is obtained from the line-shift of contrast profiles (Figure 4.10), while the plane-of-sky velocity (red) from the height-time profile (Figure 4.6). The total velocity (black) results from the combination of the line-of-sight and plane-of-sky velocities.

As for the potential energy in Equation (4.5), it is reduced to $\rho_m g_h r$. Here $g_h = g_\odot(\frac{R_\odot}{R_\odot+h})$ is the gravitational acceleration, where $g_\odot = 2.74 \times 10^4$ cm s^{-2} and $R_\odot = 6.96 \times 10^5$ km, are the solar radius and r the radial distance. Taking the derived mass density and the distance estimated from the height-time measurements, the potential energy of the filament eruption is obtained. Then a solution for Equation (4.5) is found and the mechanical energy per unit volume is calculated. In Figure 4.13 the energies E_k, E_p, and E_{mc} of the filament eruption on 2017 April 23 are presented. The plots also compare to the results of the energies derived by considering a constant mass density as given in Jefferies & Orrall (1963) for a typical quiescent prominence ($\rho_m = 1.7 \times 10^{-13}$g cm^{-3}), and used in some previous works.

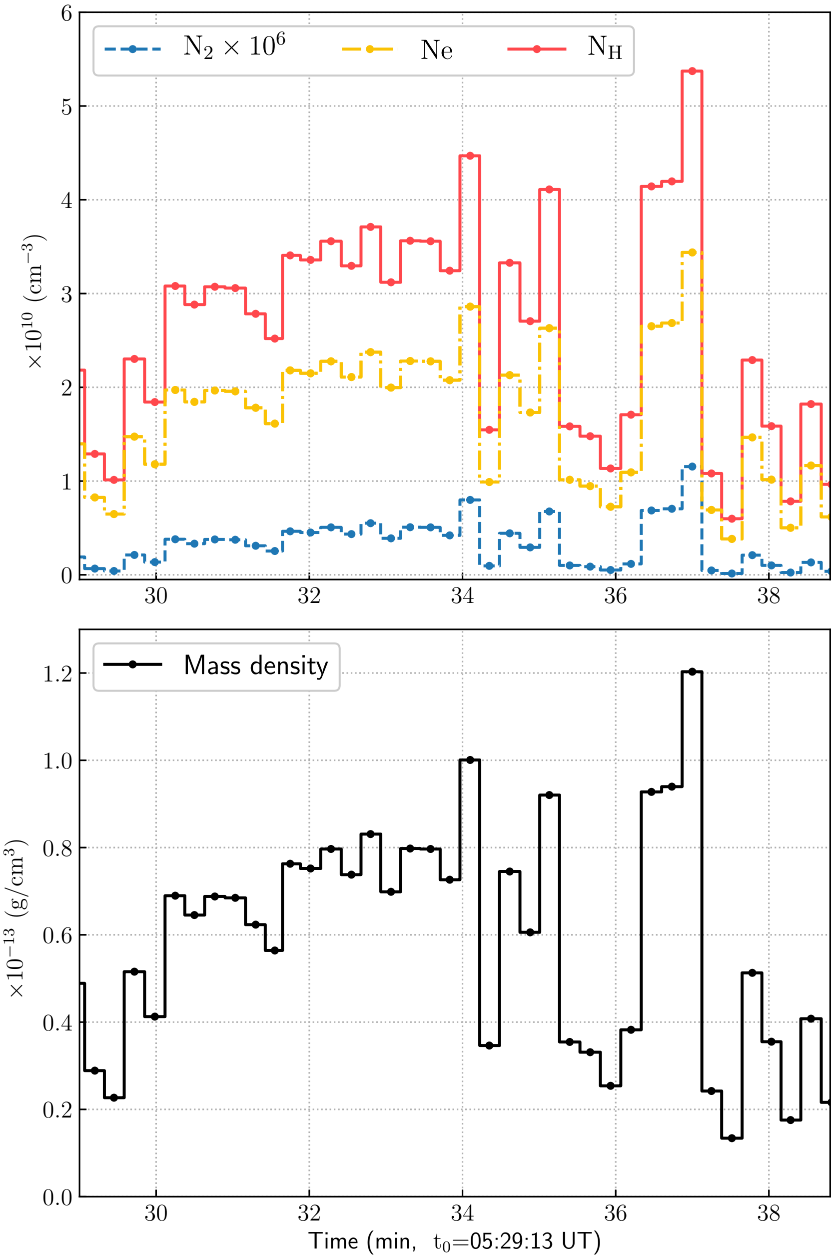

Figure 4.12: Time variation of the densities N_2, Ne, and N_H (upper panel), and the mass density (lower panel) of the filament eruption on 2017 April 23. The derivation of these parameters are based on the "cloud model" results and applying the relations given in Yakovkin & Zeldina (1975) and Tsiropoula & Schmieder (1997) (see the text). The time period spanning from 05:29 to 05:39 UT, covers the fast-rising phase of the eruption.

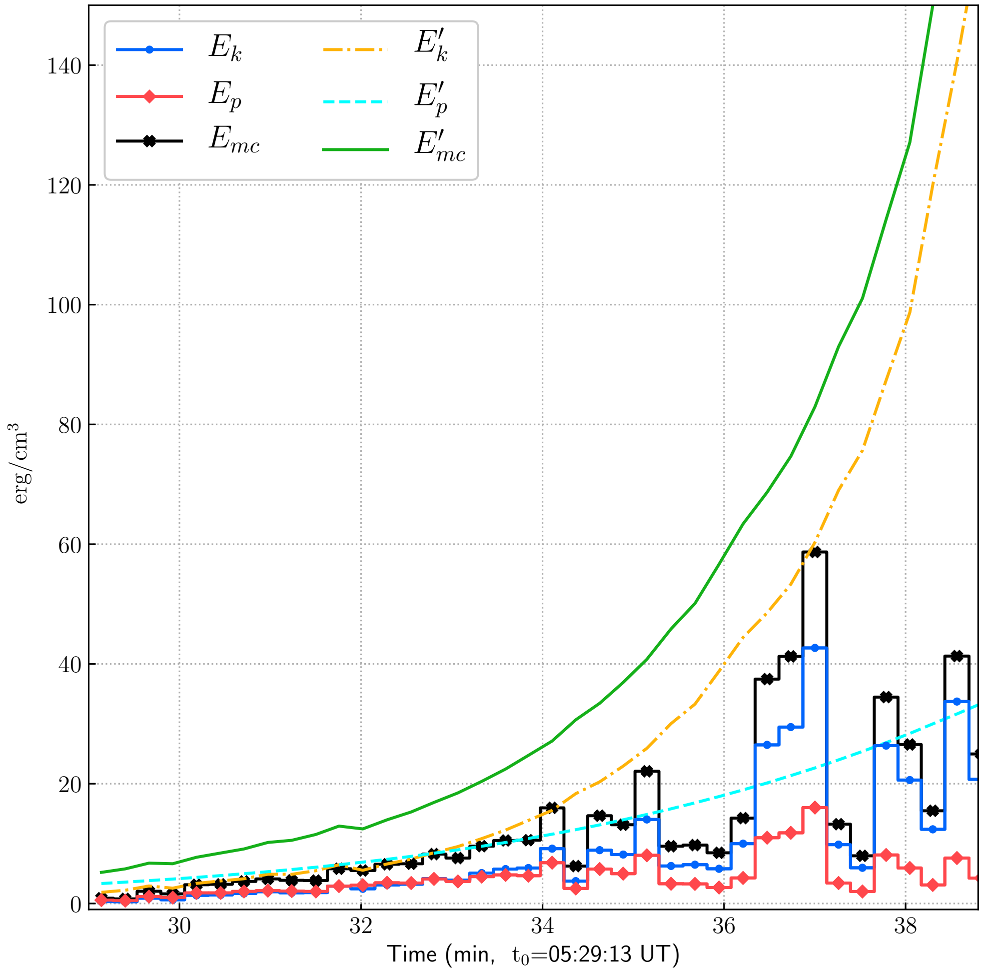

Figure 4.13: Kinetic E_k, potential E_p, and mechanical E_{mc} energies per unit volume of the filament eruption on 2017 April 23. For the calculation we used the mass density presented in Figure 4.12. To compare and see how the energies evolves if ones considers a constant mass density, we also plotted E'_k, E'_p, and E'_{mc} adopting a typical density of an ordinary prominence (1.7×10^{-13}g cm^{-3}).

4.4 Discussion and Conclusions

We studied a fast-filament eruption captured by SMART/SDDI, whose signatures of the erupting material was detected in very far-wing of the Hα line. This observation is an example that filaments can be ejected from the solar surface having line-of-sight velocities higher than 300 km s^{-1}. Despite the weakness of the associated flare (B-class), the eruption generated a fast CME ($\sim$ 955 km s^{-1}).

Inspecting the time-evolution of the height, velocity, and acceleration (Figure 4.6), we found that the filament undergoes the process of the eruption by following three typical stages: (1) pre-eruption, in which the filament shows a slow ascending motion and starts to expand gradually, this occurs between 05:10 to 05:30 UT; (2) main or acceleration, at this point the system becomes very dynamic exhibiting an exponential-like rise, taking place from 05:30 to 05:40 UT; and (3) subsequent propagation. The first stage mentioned above, can be interpreted as a natural consequence of the filament expansion because of the decrease of the pressure with height and possibly due to the rearrangement of the overlying field lines. As for the second stage, it is more likely that some instability (e.g., torus) entered in action (cf. Kliem & Torok, 2006; Kusano, et al., 2012), although it can be also discussed in relation to the loss-of-equilibrium, since as demonstrated by Démoulin & Aulanier (2010) the instability and the loss-of-equilibrium can be interpreted as two different views of the same physical process (see also Shibata & Magara, 2011).

The maximum velocity and acceleration attained by the eruption as derived from Hα and 304 Å observations is about 700 km s^{-1} and 2.5 km s^{-2}, respectively. These values are relatively higher than the average of previous statistical works (e.g., Vršnak, 2001; McCauley et al., 2015). In the velocity profiles it is noted a delay of 304 Å with respect to that of Hα, particularly at the time when the eruption reaches the maximum height; this aspect is significantly reflected in the acceleration profile. An interesting aspect of this particular event is that once the eruption disappears in Hα, there occurs a drastic deceleration which is observed at 304 Å. In this respect, one can speculate that under some circumstance the driving force responsible for the eruption simply ceased to exist. When the filament entered into the eruptive state, it also experienced a helical motion (see Figures 4.5, 4.7). This suggest that the internal structures of the filament might have accumulated high magnetic helicity before the onset of the eruption. Signatures of the untwisting motion can be also observed in the legs of the erupting structure.

The line-of-sight velocity maps obtained with the "cloud model" show a complex evolution of the overall erupting filament (Figure 4.8). The initial phase of the eruption is accompanied by the increase of the line-of-sight velocity at the summit of the loop-like structure formed during the rising phase. It can be also seen that as the time goes on, there is a manifestation of red and blue patterns in the loop legs located north- and southward, respectively. This clearly indicates that an expansion of the loop-like structure is ongoing, but the loop legs remain rooted to the solar surface. Once the disruption occurs at about 05:38 UT, higher Doppler velocity is observed especially in the lateral part of the disrupted structure. Then the material is ejected into the interplanetary space with a line-of-sight velocity nearly to 300 km s^{-1}, and a great portion of the ejecta is directed towards the Earth. It is not common to find in the literature reports on filament eruptions possessing higher velocity component along the line-of-sight. Our finding could be the first of this kind, in which the whole process and evolution of the eruption was captured. In the following there will be more reports similar to our observations thanks to the SDDI capability.

On the other hand, different from the previous works in which constant mass density were considered, here we attempted to estimate the time-variation of the density during the eruption by taking the calculated optical depth and the Doppler width, and applying the relations originally given for small-scale and quasi-static features. It should be mentioned however, that for large velocity gradient of moving clouds such as presented in this work, the DBE could have strong influences. In consequence, our obtained results may involve considerable errors from a quantitative point of view, although we believe that our results represent a proxy of the real situation.

The combination of the derived velocities in the plane-of-sky, line-of-sight, and the mass density of the filament eruption permitted us to calculate the time evolution of kinetic, potential, and the mechanic energies of the filament eruption. As presented in Figure 4.13 the results have a strong dependence on the time variation of the mass density. Our results show that more kinetic energy is supplied during the fast-rising phase of the filament, consequently more mechanical energy per unit volume. For comparison we also included in the plot the mechanical energy estimated with a constant mass density (1.7×10^{-13}g cm^{-3}), such as used in previous works. We found that there is a large difference between the mechanical energy derived with a constant mass density and that calculated with our estimated mass density. Therefore, this tells us about on the importance in deriving the time-variation of the mass density of an erupting filament. This also means in order to constrain the results, it is necessary to accurately measure the velocity field of fast moving clouds. For example, Morimoto et al. (2010) found a positive correlation between the mechanical and thermal energies. The authors interpreted their results as the stored magnetic energy is carried by the Poynting flux to be converted into thermal energy via magnetic reconnection, they also discussed on the importance of the Lorentz force in accelerating the filament. Indeed, the correlation found by Morimoto et al. (2010) can be further verified conducting a statistical study. Now this is possible because of the good enough quality of the Hα data, and also the unprecedented AIA observations which can be used for the temperature diagnostics of erupting filaments by applying the differential emission measure technique.

References

Beckers, J. M., 1964, PhD Thesis, Univ. Utrecht

Démoulin, P., & Aulanier, G. 2010, ApJ, 718, 1388

Filippov, B.P., & Den, O. G. 2001, J. Geophys. Res., Vol. 106, 25, 177

Hanaoka, Y., Shinkawa, T. 1999, ApJ, 510, 466

Heinzel, P., Rompolt, B. 1987, SoPh, 110, 171

Howard, R.A., Moses, J.D., Vourlidas, A., et al. 2008, SSRv, 136, 67

Ichimoto, K., Ishii, T.T., Otsuji K., Kimura, G., et al. 2017, SoPh, 292, 63

Ishii, T., Kawate, T., Nakatani, Y., Morita, S., Ichimoto, K., Masuda, S. 2013, PASJ, 65, 39

Jefferies, J.T., & Orrall,F.Q. 1963, ApJ, 137, 1232

Kaiser, M.L., Kucera, T.A., Davila, J.M., et. al. 2008, SSRv, 136, 5

Kliem, B., & Torok, T. 2006, Phys. Rev. Lett., 96, 255002

Kuhn, J.R., Lin, H., & Loranz, D. 1991, PASP, 103, 1097

Kusano, K., Bamba, Y., Yamamoto, T. T., et al. 2012, ApJ, 760, 31

Lemen, J. R., Title, A., Akin, D. J., et al. 2012, SoPh, 275, 17

McCauley, P. I., Su, Y. N., Schanche, N., et al. 2015, SoPh, 290, 1703

Morimoto, T., Kurokawa, H., Shibata, K., Ishii, T.T. 2010, PASJ, 62, 939

Nagata, S.-i., Morita, S., Ichimoto, K., Nishida, K., Nakatani, Y., et al. 2014, PASJ, 66, 45

Pesnell, W. D., Thompson, B. J., Chamberlin, P. C. 2012, SoPh, 275, 3

Shibata, K., Magara, T. 2011, Living Rev. of Solar Phys., 8, 6

Tsiropoula, G., Schmieder, B. 1997, A&A, 324, 1183

Tsiropoula, G. 2000, A&A, 357, 735

Tziotziou, K., 2007, in ASP, Conf. Ser. 368, The Physics of Chromospheric Plasmas, ed. P. Heinzel, I. Dorotovic, & J. Rutten, 217

UeNo, S., Nagata, S.-i., Kitai, R., Kurokawa, H., & Ichimoto, K. 2004, proc. SPIE, 5492, 958

Vršnak, B. 2001, J. Geophys. Res., Vol. 106, 25, 249

Yakovkin, N.A., Zeldina, M. Yu. 1975, SoPh, 45, 319

Chapter 5

Concluding Remarks

5.1 Brief Overview of Results

In this thesis observational results of solar eruptive events, including two filament eruptions (Chapters 2, 4) and a Moreton wave (Chapter 3) have been presented. The investigation also included the analysis of the associated phenomena of the events mentioned above, such as coronal waves and filaments activation/oscillation due to the interaction with the wave fronts. One of the main objectives of this thesis was to advance into our understanding of chromospheric phenomena by using Hα observations as a primary data source. The Hα chromospheric line has long been used not only for observations of eruptive events but also for quiet chromospheric fine structures, and nowadays still remains as a powerful tool for solar plasma diagnostics.

To summarize the results of Chapter 2, it was introduced a modified method of the "cloud model" for deriving the three-dimensional velocity field of the filament eruption captured by the FMT. Unlike the original method developed by Morimoto & Kurokawa (2003) in which the Doppler width was considered as a fixed parameter, in our method the Doppler width is treated as a free parameter. In this way, the derivation of the physical parameters of the analyzed filament was improved moderately. It should be mentioned that the limitation on deriving the line-of-sight velocity of the filament more accurately is because the FMT is restricted to perform observations only in three positions of the Hα spectral profile, that is, Hα center and ± 0.8 Å. Nevertheless, the FMT data was suitable for detecting the main component of the filament eruption along the line-of-sight, whose velocity was about 30 km s^{-1}. The event presented in Chapter 2 was also captured in the EUV-band by the SDO/AIA and STEREO_A/EUVI instruments. Particularly, the side-view of the eruption by STEREO_A was taken into account, which in combination with the FMT data the inclination of the filament eruption could be estimated. The results show that the filament was ejected nearly horizontally to the solar surface, meaning that the filament might have been responsible for the propagation direction of the associated coronal wave. However, for further conclusions, it would be necessary to conduct a statistical investigation on the inclination of filament eruptions and the tendency for triggering coronal waves.

In Chapter 3 we studied the dynamic and the Doppler characteristics of a Moreton wave and its relation with a coronal wave. As discussed extensively in Chapter 3, the appearance of a Moreton wave, manifested as a chromospheric disturbance, is attributed to the plasma compression because of the globally propagating shock and large-scale disturbances in the corona. Therefore, in-depth understanding on the occurrence of the Moreton wave and the response of the chromospheric plasma requires a direct examination of the interaction corona-chromosphere. The observations in the wing of the Hα line (± 0.8 Å) performed by the FMT, permitted us to investigate in detail the response of the plasma in the chromosphere to global-scale wave propagation in the corona. For example, different from previous works in which the propagation speed of the Moreton wave is often discussed, the results presented in Chapter 3 not only include the propagation speed but also more importantly the velocity amplitude of the Moreton wave, that is, the velocity of the chromospheric plasma traveling downward at front of the Moreton wave. The importance in deriving the downward/upward motion of the plasma in the chromosphere associated with the passage of the Moreton wave, is because, this can be regarded as a direct signature of the shock strength in the corona. Indeed, the result obtained from our Hα observations was used to infer the velocity amplitude of the incident wave from the corona to the chromosphere by applying the MHD linear theory. This estimation led us to suggest that a wave traveling at the base of the corona downward with a velocity $\gtrsim 10$ km s^{-1}, could be able to produce a noticeable disturbance in the chromosphere seen as a Moreton wave. Moreover, the calculated velocity amplitude of the Moreton wave in conjunction with the weak-shock approximation were used to quantify the strength of the incident shock in the corona by deriving the Mach number. Perhaps our work is the first one that focused seriously on the Doppler characteristics of the Moreton wave, and also in the estimation of the velocity amplitude of the disturbance in the chromosphere and the Mach number of the incident shock. On the other hand, the multi-temperature coverage of AIA along with the XRT observations allowed us to characterize the local plasma responses to the coronal wave passage. Applying the differential emission measure diagnostic, the compression ratio distribution was calculated, which led to the determination of the Alfvén and fast-mode Mach numbers of the coronal wave. Based on the compression ratio distribution, it was found that the coronal wave propagates in a complex manner along the different trajectories, meaning that the field strength and the density in the corona are distributed non-uniformly. Consequently, in certain sectors high compression ratio values were obtained, favoring to strong compression in the chromosphere. In fact, we found that large velocity amplitude of the disturbance in the chromosphere are closely connected to high values of the compression ratio.

A fast-filament eruption recorded in the Hα line by SMART/SDDI was analyzed in Chapter 4. Thanks to the SDDI capability it was possible to carry out imaging and spectral investigations of the event. The analysis focused on: (1) the acceleration of the fastest or leading edge of the eruption, (2) the evolution of the overall erupting structure along the line-of-sight, and (3) the mechanical energy of the filament during its fast-rising stage. The acceleration was calculated in the plane-of-sky, which exhibited a exponential-line growth. As for the line-of-sight velocity, on the other hand, it was calculated by using the "cloud model". It is well known that the reliability of the physical information obtained from the "cloud model" depends on the number of wavelengths along the spectral profile, that is, filtergrams obtained at multiple wavelengths around the Hα line are more suitable than two or a few wavelengths that have been used in the majority of previous and similar works. Therefore, our derivation of the line-of-sight velocity of the filament eruption can be considered as the more reliable. Moreover, because there is no limitation in the wavelength range at which the SDDI observes, fastest components of the filament eruption traveling along the line-of-sight were detected. Regarding the mechanical energy of the filament eruption, as it was shown in Equation (4.5) the mass density of the filament is an important parameter. In this works, based on the "cloud model" results and applying some relations, the mass density of the filament was estimated and used to calculate the mechanical energy. Here it is important to mention that possibly our estimates of the mass density involves a substantial uncertainty, because as it was mentioned in Chapter 4 the effect of the Doppler brightening was not taken into account. As claimed by some authors, there is no doubt that the Doppler brightening effect has a strong influence in the intensity variation of high speed eruptions, especially of those observed in the far-wing of the Hα line. In a future work, the Doppler brightening effect will be considered in our analysis, and the role of it will be discussed in more detail.

5.2 Future Directions

The results presented in this thesis will be useful to constrain the understanding about solar eruptions and the related phenomena. It could be also of great importance for space weather, a topic that in the recent years has received a special attention.

In the context of large-scale disturbances in the solar atmosphere, particularly of those occurring in the chromosphere, in this work we attempted to elucidate quantitatively how the chromospheric plasma reacts to the global propagating disturbance in the corona. In a future work it would be interesting to confront our results of the velocity amplitude of the disturbance in the chromosphere with numerical simulations. Furthermore, when spectroscopy observations of coronal wave fronts are available, it will be important to compare the indirect measures of the coronal wave we obtained from Hα data, e.g., the velocity of the incident wave in the corona traveling behind the shock wave, and the Mach number of the incident shock. On the other hand, it is also required to constrain our comprehension on the response of the local plasma to the coronal wave passage, for example, the variation of the density, temperature, and especially the plasma flows. Nowadays it is possible thanks to the multi-temperature AIA data, as in the work we did the differential emission measure diagnostics could be useful for this.

In relation to space weather, the derived three-dimensional velocity field of the filament eruptions could be very useful for investigating the initial stage of the CME formation and its geo-effectiveness. Since the geo-effectiveness of a CME depends primarily on the velocity and the magnetic orientation of it when impact at the Earth's magnetosphere, an accurate estimation of the three-dimensional velocity of the eruption could be very effective for the diagnostic of the initial phase of the CME, which in turn could be practical for predicting the CMEs. Statistical works relating the velocity field of filament eruptions to the CMEs speed and/or geo-effectiveness will be bring more clues about the Earth affecting CMEs. It is important to mention that the velocity of filament and prominence eruptions are being better monitored thanks to the SDDI capability, now we are able to measure the line-of-sight component of the eruptions with high accuracy.

Appendices

Appendix A

Mach Number in Terms of the Moreton Wave Velocity Amplitude

In this Section we present the derivation of Equation (3.5) introduced in Chapter 3. Here we discuss the 1D Riemann problem in the hydrodynamical regime (Landau & Lifshitz, 1987) based on the weak-shock approximation. The three-dimensionality and the magnetohydrodynamic effects are not considered. Figure A.1 shows an illustration of shock interaction before and after the collision with the contact discontinuity (transition region). In the scheme the solid thick line represent the variation of the pressure p along the x-axis. Before the collision, the initial pressure distribution in the chromosphere and corona are in equilibrium ($p_0 = p_{ch} = p_{co}$, $v_{ch} = v_{co} = 0$) and is separated by the contact discontinuity. In our analysis the coronal shock (incident shock) propagates from right to left, where its downstream region is characterized by enhanced pressure $p'_{co} = p_{co,perturbed}$ and velocity $v'_{co} = v_{co,perturbed}$. Note that in the following we take the direction from the chromosphere to corona as positive direction, and thus, $v'_{co} = v_{co,perturbed} < 0$. After the collision of the incident shock with the contact discontinuity, the pressure and the velocity distribution can be divided into three regions: $p = p_0$, $v = 0$ in the leftmost region; $p = p'_{co}$, $v = v'_{co}$ in the rightmost; and an intermediate region characterized with $p_\star$ and v_t (lower panel in Figure A.1).

The Rankine-Hugoniot relations tells us about the jump conditions at the incident i, transmitted t, and reflected r shocks, in which the Mach number of each shock can be expressed respectively as

$$M_i^2 = 1 + \frac{\gamma+1}{2\gamma}\left(\frac{p'_{co}}{p_0} - 1\right), \quad M_t^2 = 1 + \frac{\gamma+1}{2\gamma}\left(\frac{p_\star}{p_0} - 1\right), \quad M_r^2 = 1 + \frac{\gamma+1}{2\gamma}\left(\frac{p_\star}{p'_{c0}} - 1\right) \tag{A.1}$$

$$0 - v'_{co} = \frac{2c_{co}}{\gamma+1}\frac{M_i^2-1}{M_i}, \quad 0 - v_t = \frac{2c_{ch}}{\gamma+1}\frac{M_t^2-1}{M_t}, \quad (-v'_{co}) - (-v_t) = \frac{2c'_{co}}{\gamma+1}\frac{M_r^2-1}{M_r} \tag{A.2}$$

where $c_{co} = \sqrt{\gamma p_0/\rho_{co,unperturbed}}$, $c_{ch} = \sqrt{\gamma p_0/\rho_{ch,unperturbed}}$, $c'_{co} = \sqrt{\gamma p'_0/\rho_{co,perturbed}}$; therefore,

$$-v'_{co} = \frac{2c_{co}}{\gamma+1}\frac{M_i^2-1}{M_i} = \frac{2c'_{co}}{\gamma+1}\frac{\frac{\gamma+1}{2\gamma}\left(\frac{p_\star}{p'_{co}}-1\right)}{\sqrt{1+\frac{\gamma+1}{2\gamma}\left(\frac{p_\star}{p'_{co}}-1\right)}} + \frac{2c_{ch}}{\gamma+1}\frac{\frac{\gamma+1}{2\gamma}\left(\frac{p_\star}{p_{co}}-1\right)}{\sqrt{1+\frac{\gamma+1}{2\gamma}\left(\frac{p_\star}{p_{co}}-1\right)}}. \tag{A.3}$$

Because p'_{co} can be described with p_0 for a given M_i in Equation (A.1), the second equality of Equation (A.3) determines the dependence of $p_\star$ on p_0 and M_i, and thus, M_t and v_t can be also determined as a function of p_0 and M_i by Equation (A.2). Particularly, for a weak shock $M_i^2 - 1 \ll 1$ ($\Leftrightarrow \delta := p'_{co}/p_0 - 1 \ll 1$), $\delta_\star := p_\star/p_0 - 1 \ll 1$, then we have

$$M_i^2 - 1 \approx \frac{\gamma+1}{2\gamma}\delta, \quad \frac{\frac{p_\star}{p'_{co}}-1}{\sqrt{1+\frac{\gamma+1}{2\gamma}\left(\frac{p_\star}{p'_{co}}-1\right)}} \approx \delta_\star - \delta, \quad \frac{\frac{p_\star}{p_0}-1}{\sqrt{1+\frac{\gamma+1}{2\gamma}\left(\frac{p_\star}{p_0}-1\right)}} \approx \delta_\star. \tag{A.4}$$

The previous statements lead us to express Equation (A.3) as

$$\frac{c_{co}}{\gamma}\delta \approx \frac{c_{co}}{\gamma}(\delta_\star - \delta) + \frac{c_{ch}}{\gamma}\delta_\star, \tag{A.5}$$

which is reduced to

$$\delta_\star = \frac{2}{1 + c_{ch}/c_{co}}\delta. \tag{A.6}$$

Furthermore, we can relate the Mach numbers of incident and transmitted shock as

$$M_t^2 - 1 \approx \frac{2}{1 + c_{ch}/c_{co}}(M_i^2 - 1), \tag{A.7}$$

then from Equations in (A.2) we arrive to an expression that relates v_t to the Mach number of transmitted and incident shocks from the corona

$$v_t \approx -\frac{2c_{ch}}{\gamma+1}(M_t^2-1) \approx -\frac{4c_{ch}}{\gamma+1}(M_i^2-1)\frac{1}{1+c_{ch}/c_{co}}. \tag{A.8}$$

It should be noted again that v_t is the velocity in the intermediate region, which appears after the collision between the shock and the contact discontinuity (Figure A.1). In other words, the contact discontinuity starts to move leftward with the velocity of v_t, also affecting the chromosphere, and could be observed as the Doppler shift of the Hα line.

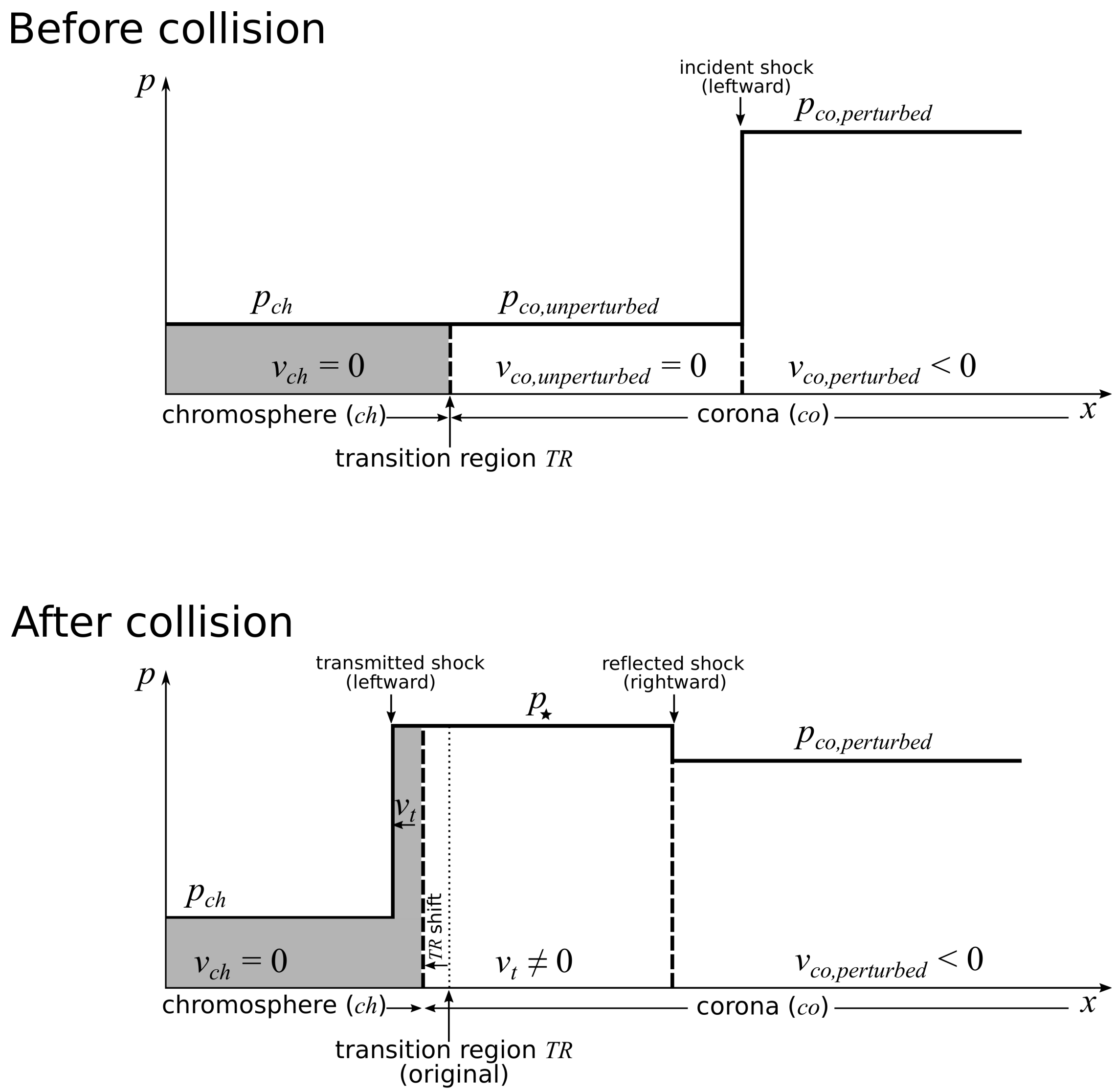

Figure A.1: One-dimensional Riemann problem in a hydrodynamical regime of shock interaction with the corona and chromosphere. In the illustration the transition region represents the contact discontinuity. The thick solid lines show the variation of the pressure distribution p along the x-axis, i.e., the change of the pressure in the corona and chromosphere before and after the collision of the shock with the contact discontinuity.

Appendix B

Alfvén Mach Number from Oblique Shock Jump Relations

Here we show the solution of Equation (3.6) used in Chapter 3 for deriving the Alfvén Mach number of the coronal wave. The following notation describes an oblique shock (Priest, 2000):

$$(v_1^2 - Xv_{A1}^2)^2\{Xc_s^2 + \frac{1}{2}v_1^2\cos^2\theta(X(\gamma-1)-(\gamma+1))\} + \frac{1}{2}v_{A1}^2v_1^2\sin^2\theta X \times\{(\gamma+X(2-\gamma))v_1^2 - Xv_{A1}^2((\gamma+1)-X(\gamma-1))\} = 0. \tag{B.1}$$

Assuming the adiabatic index $\gamma = 5/3$ and expressing the sound speed as $c_s^2 = (\gamma\beta/2)v_A^2$, the first and second part of Equation (B.1) can be written as

$$\frac{1}{3}(v_1^2 - Xv_{A1}^2)^2\left\{\frac{5}{2}X\beta v_{A1}^2 + v_1^2\cos^2\theta(X-4)\right\} + \frac{1}{3}v_{A1}^2v_1^2\sin^2\theta X \times\left\{\frac{v_1^2}{2}(5+X) + v_{A1}^2X(X-4)\right\} = 0, \tag{B.2}$$

and multiplying by $1/v_{A1}^2$ allows to express it in terms of Alfvén Mach number M_{A1}

$$(v_1^2 - Xv_{A1}^2)^2\left\{5\beta X + 2M_{A1}^2\cos^2\theta(X-4)\right\} + v_{A1}^2v_1^2\sin^2\theta X \times\left\{M_{A1}^2(5+X) + 2X(X-4)\right\} = 0. \tag{B.3}$$

Finally, after some algebraic procedures we arrive at the following solution

$$(M_{A1}^2 - X)^2 \left\{ 5\beta X + 2M_{A1}^2 \cos\theta^2 (X-4) \right\} + M_{A1}^2 \sin\theta^2 X$$
$$\times \left\{ M_{A1}^2 (5+X) + 2X(X-4) \right\} = 0, \quad \text{(B.4)}$$

which is Equation (3.7) presented in Section 3.5.3. Vršnak et al. (2002a) also arrived at the same solution. We used Equation (B.4) to calculate the Alfvén Mach number assuming two cases, horizontal ($\theta = 0$) and perpendicular ($\theta = 90$) shock propagation. For the horizontal case Equation (B.4) is reduced to $M_A = \sqrt{X}$, while for the perpendicular situation, it is $M_A = \sqrt{\frac{X(5+X+5\beta)}{2(4-X)}}$.